EFFECTS OF AEROSOLS ON DEEP CONVECTIVE CUMULUS CLOUDS

A Dissertation

by

JIWEN FAN

Submitted to the Office of Graduate Studies of
Texas A&M University
in partial fulfillment of the requirements for the degree of

DOCTOR OF PHILOSOPHY

August 2007

Major Subject: Atmospheric Sciences

EFFECTS OF AEROSOLS ON DEEP CONVECTIVE CUMULUS CLOUDS

A Dissertation

by

JIWEN FAN

Submitted to the Office of Graduate Studies of
Texas A&M University
in partial fulfillment of the requirements for the degree of

DOCTOR OF PHILOSOPHY

Approved by:

Chair of Committee, Renyi Zhang
Committee Members, Don Collins
Robert Duce
Simon North
Wei-Kuo Tao
Head of Department, Richard Orville

August 2007

Major Subject: Atmospheric Sciences

ABSTRACT

Effects of Aerosols on Deep Convective Cumulus Clouds. (August 2007)

Jiwen Fan, B.S., Xiantan Normal University;

M.S., China University of Mining & Technology (Beijing Campus);

M.S., University of Central Florida

Chair of Advisory Committee: Dr. Renyi Zhang

This work investigates the effects of anthropogenic aerosols on deep convective clouds and the associated radiative forcing in the Houston area**.** The Goddard Cumulus Ensemble model (GCE) coupled with a spectral-bin microphysics is employed to investigate the aerosol effects on clouds and precipitation. First, aerosol indirect effects on clouds are separately investigated under different aerosol compositions, concentrations and size distributions. Then, an updated GCE model coupled with the radiative transfer and land surface processes is employed to investigate the aerosol radiative effects on deep convective clouds. The cloud microphysical and macrophysical properties change considerably with the aerosol properties. With varying the aerosol composition from only $(NH_4)_2SO_4$, $(NH_4)_2SO_4$ with soluble organics, to $(NH_4)_2SO_4$ with slightly soluble organics, the number of activated aerosols decreases gradually, leading to a decrease in the cloud droplet number concentration (CDNC) and an increase in the droplet size. Ice processes are more sensitive to the changes of aerosol chemical properties than the warm rain processes. The most noticeable effect of increasing aerosol

number concentrations is an increase of CDNC and cloud water content but a decrease in droplet size. It is indicated that the aerosol indirect effect on deep convection is more pronounced in relatively clean air than in heavily polluted air. The aerosol effects on clouds are strongly dependent on RH: the effect is very significant in humid air.

Aerosol radiative effects (ARE) on clouds are very pronounced for mid-visible single-scattering albedo (SSA) of 0.85. Relative to the case without the ARE, cloud fraction and optical depth decrease by about 18% and 20%, respectively. The daytime-mean direct forcing is about 2.2 W m^{-2} at the TOA and -17.4 W m^{-2} at the surface. The semi-direct forcing is positive, about 10 and 11.2 W m^{-2} at the TOA and surface, respectively. Aerosol direct and semi-direct effects are very sensitive to SSA. The cloud fraction, optical depth, convective strength, and precipitation decrease with the increase of absorption, resulting from a more stable atmosphere due to enhanced surface cooling and atmospheric heating.

DEDICATION

I would like to dedicate this document to my parents, Jielian Xiao and Silai Fan.

ACKNOWLEDGEMENTS

I am deeply grateful to my adivsor, Dr. Renyi Zhang, for his wise guidance, tremendous support and help during my Ph.D. study. He is not only a good mentor advising us in research, but also guiding us to acquire all-round abilities to be successful in our careers. I greatly thank my committee members, Drs. Wei-Kuo Tao, Don Collins, Robert Duce, and Simon North, for their valuable comments and great assistance during this process. Dr. Wei-Kuo Tao was also our collaborator and provided the GCE cloud model. Special appreciation goes to him for his assistance in cloud modeling and during my visit at NASA/Goddard, and also to Dr. Don Collins for his collaboration and help in aerosol observational data. Dr. Larry Carey is greatly appreciated for substituting for Dr. Wei-Kuo Tao at my preliminary exams and for Dr. Robert Duce at my final defense. Dr. Karen Mohr of SUNY, Albany is also greatly acknowledged for collaboration in land surface modeling.

I am thankful to all data providers and helpers during this research: Dr. Che-Jen Lin of Lamar University for providing the gridded emission data; Drs. Matthew Russell and David Allen at University of Texas for providing the TEOM and FRM field measurement data; Dr. Charles Brock of NOAA/Chemical Science Division for providing aerosol aircraft data; Dr. Larry Carey and John Nielsen-Gammon of our department for help with the radar data; Dr. Jerome Fast of PNNL for observed aerosol optical data; Dr. Robert J. Zamora at NOAA for help with the observed surface data; and Drs. Y. Lee and J. Santarpia in Dr. Collins's group for help with the aerosol data.

I want to express my gratitude to my fellow group members for their frequent help and for sharing experiences here. I am also especially thankful to Drs. Xiaowen Li, Stephen E. Lang and Chung-Lin Shie in Dr. Tao's group for help with the cloud simulations.

I would like to thank the department staff, especially Neil Smith, for their work and technical support.

This study was partially supported by NSF (ATM-0424885). I was supported by a NASA Earth System Science (ESS) fellowship.

Finally, I want to thank my family for their love, patience and full support.

TABLE OF CONTENTS

Page

Page

LIST OF TABLES

Page

LIST OF FIGURES

Page

Page

Page

Page

1. INTRODUCTION

1.1 Aerosol Effects on Clouds and Climate

Aerosols in the atmosphere have been of great interest in recent years [*EPA*, 1996; 2000; *Zhang et al.*, 2004]. High aerosol concentrations are associated not only with adverse human health effects, but also contribute to acid precipitation, global and regional climate change and visibility degradation [*EPA*, 1996; 2000; *Zhang et al.*, 2007]. Aerosol-cloud-climate interactions are very complicated and have drawn high attention in the recent years. Aerosols directly or indirectly affect the Earth's energy balance [*Charlson et al.*, 1987; *Houghton et al.*, 2001], as schematically depicted in Figure 1.1. The aerosol direct effect occurs under clear-sky conditions by scattering or absorbing solar radiation. Absorbing aerosol heats and warms the atmosphere locally, modifies the atmospheric lapse rate of temperature and may suppress convection and reduce cloud fraction. This effect has been labeled the semi-direct effect [*Hansen et al.*, 1997; *Johnson et al.*, 2004]. The indirect effect refers to any influence of aerosols on cloud microphysics, cloud duration, precipitation, etc. [*Twomey*, 1977; *Rosenfeld*, 2000]. These include the first indirect effect referred to as the Twomey effect concerning the decrease of cloud droplet size and the increase of cloud reflectance with increasing aerosols in a constant liquid water content [*Twomey*, 1977], and the second indirect effect which proposes that an increase in aerosol will increase cloud liquid water, extend cloud coverage and lifetime, and reduce the precipitation [*Albrecht*, 1989].

This dissertation follows the style of *Journal of Geophysical Research*.

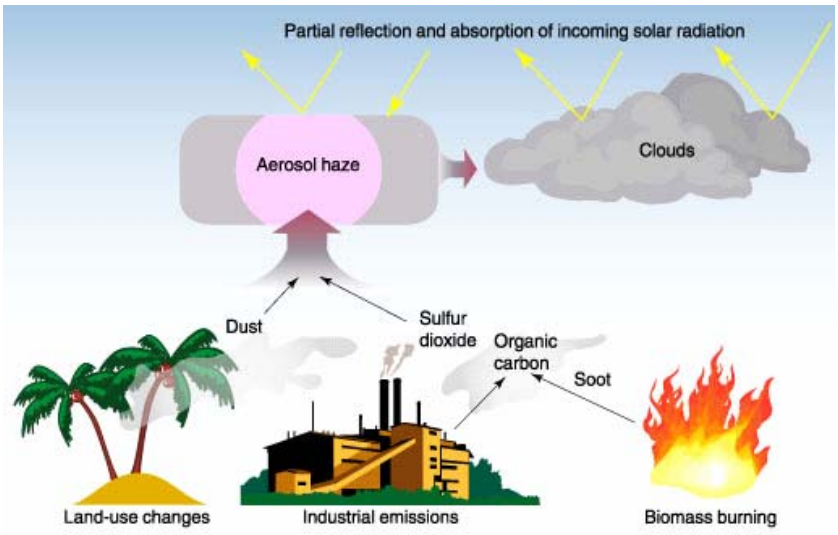

Figure 1.1 Aerosol-cloud-climate interactions [*Chuang*, 2003].

Currently our understanding of aerosol effects on radiative forcing is at a very low level, as indicated in Figure 1.2 by *IPCC* [2001]. The estimation of the direct radiative forcing exerted by aerosols is complex to quantify because anthropogenic particles are generally a complex mixing of different chemical components [*Hegg et al.*, 1997; *Ramanathan et al.*, 2001a]. Each component is characterized by its own microphysical, chemical, and related optical properties, which lead to variable direct radiative forcing. The uncertainty for the aerosol direct climate forcing is about a factor of 2 to 3 [*IPCC*, 2001]. The global mean TOA aerosol direct forcing values range from -0.5 to +0.2 W m^{-2} [*Ramanathan et al.*, 2001b]. The measured TOA direct forcing on the regional scale ranges from -9 to 2 W m^{-2} [*Ramanathan et al.*, 2001b; *Ramachandran*, 2005]. The semi-direct effect introduces the added feedbacks due to the radiative

properties of the aerosol (i.e., absorption) and has been studied in the recent years. *Ackerman et al.* [2000] showed decreases in cloudiness commensurate with the heating rates associated with absorbing aerosol. *Johnson et al.* [2004] and *Feingold et al.* [2005] argued that the vertical location of the absorbing aerosol is important: absorbing aerosol may reduce cloud water and cloud fraction or increase them. On the other hand, the reduction in downwelling solar radiation and associated decrease in surface latent and sensible heat fluxes result in significant reduction in cloud water and cloud fraction [*Feingold et al.*, 2005; *Jiang and Feingold*, 2006]. The semi-direct forcing was estimated to be about 15 W m^{-2} for stratocumulus by *Johnson et al.* [2004] and 7.5 W m^{-2} for trade cumulus by *Ackerman et al.* [2000].

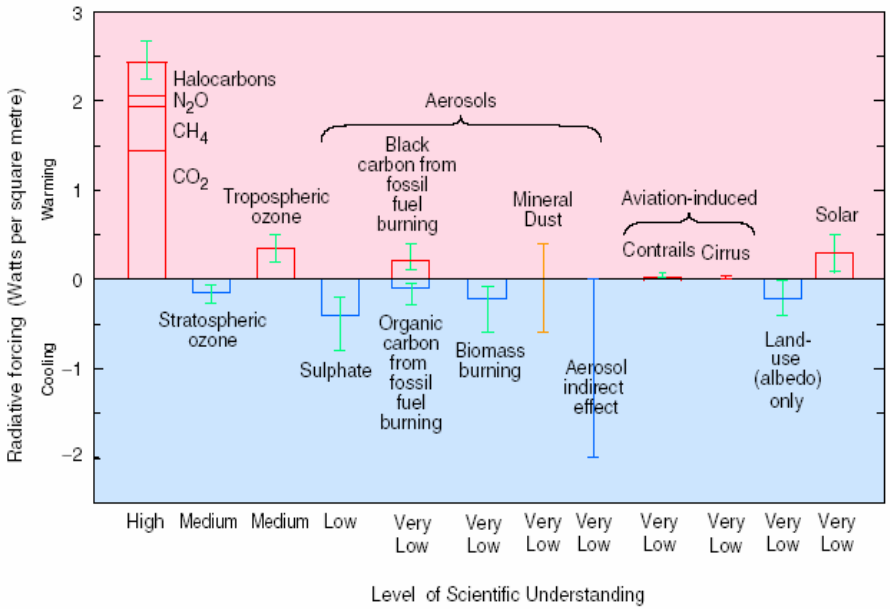

Figure 1.2 The global annual mean radiative forcing (1750-present) [*IPCC*, 2001].

The aerosol indirect effect constitutes the greatest uncertainty in climate forcing

(Figure 1.2) [*IPCC*, 2001]. For example, aerosols in polluted air may influence the cloud processes and precipitation by serving as cloud condensation nuclei (CCN), potentially forming smaller cloud droplets and higher concentrations. *Maritinsson et al.* [1999] reported a significant increase in cloud droplet concentrations (up to 2000 cm^{-3}), together with a substantial reduction in the effective droplet radius in polluted orographic clouds. The aerosol effect on precipitation is also one of the most important issues of anthropogenic climate change [*Hobbs*, 1993]. Several observations demonstrated that smoky tropical clouds have less precipitation [*Rosenfeld,* 1999; *Rosenfeld and Woodley,* 1999]. *Rosenfeld* [2000] reported a decrease in precipitation in urban areas because of suppression of the warm rain processes by anthropogenic aerosols. It is worth noting that the reduction of warm rain production rate in cumulus clouds of smoky air does not mean that the accumulated precipitation will automatically decrease [*Khain et al.*, 2004; *Andreae et al*., 2004]. A decrease in warm rain production may result in an increase in precipitation formed by cloud ice melting [*Khain et al.*, 2004]. Also, reduced cloud droplet sizes may delay the onset of warm precipitation, leading to invigoration and restructuring of clouds. Measurements of heavy smoke forest fires in the Amazon found suppression of low-level rainout and aerosol washout which allows transport of water and smoke to upper levels, causing more intensive thunderstorms and release of more latent heat higher in the atmosphere [*Andreae et al*., 2004]. Recent analyses of satellite measurements of the aerosol optical depth and cloud top pressure also suggest a correlation between the presence of aerosols and the structural properties of clouds, indicating a likely cloud invigoration by pollution [*Koren et al*., 2005]. In addition,

enhanced deep convection and mixed-phase processes associated with urban pollution have been implicated in elevated electrification and lightning activities in thunderstorms [*Orville et al*., 2001], which may also impact the air composition [*Zhang et al*., 2003]. A recent numerical simulation study using a three-dimensional model and a bulk microphysical scheme by *Wang* [2005] suggested that the total amount of precipitation increased with the initial CCN concentration for tropical deep convective clouds.

1.2 Aerosol Properties and Houston Environments

Aerosols properties such as the chemical composition, size distribution, and number concentration are the important factors in determining cloud properties and associated radiative effects. For example, direct radiative forcing is very sensitive to particle size and aerosol types; indirect forcing is affected by aerosol chemical composition and number size distribution. An enhanced aerosol number concentration may result in an enhanced cloud droplet concentration and an increased cloud shortwave albedo. Much of the uncertainty in estimating indirect aerosol radiative forcing is due to the complexity in relating aerosol and cloud droplet number and size distributions. Several studies have been conducted to investigate the influences of aerosol properties on cloud formation and development [*Ekman et al.*, 2004; *Khain et al.* 1999; *Roelofs and Jongen*, 2004; *Zhang et al.*, 2002]. *Ekman et al.* [2004] demonstrated that the size distribution of aerosols was an important factor in determining the aerosol's fate within the convective cloud. *Khain et al.* [1999] concluded that the chemical composition of aerosol particles influenced the concentration of nucleated cloud droplets and changed accumulated rain significantly. Both aerosol size and chemical properties affect the

lifetime of the clouds, as shown in *Roelofs and Jongen* [2004].

Atmospheric aerosol composition includes sulfates, nitrates, ammonium, organic materials, sea salt, water, etc. The fine particles are found predominantly by sulfate, ammonium, organic and elemental carbon [*Seinfeld and Pandis*, 1998]. Typical polluted urban air has total concentrations of over 10^5 cm^{-3}, consisted of primarily sulfate, ammonium, organics and black carbon. Aerosol size distributions in the atmospheric models are generally represented with the sectional and modal approaches. In the modal representation, the particle size distribution is approximated by analytical functions (usually lognormal distributions) that represent the various modes of the particle population. This modal approach has been used in regional and global aerosol models [e.g., *Binkowski and Shankar*, 1995; *EPA*, 1999; *Ghan et al.*, 2001a, 2001b, 2001c]. In the sectional approach, the particle size distribution is approximated by a discrete number of size sections. The traditional sectional approaches used in air quality models conserve particle mass concentration only [e.g., *Lurmann et al.*, 1997; *Meng et al.*, 1998], but both mass and number are conserved in several newer sectional approaches [e.g., *Jacobson*, 1997, *Russell and Seinfeld*, 1998, *Zhang et al.*, 2002].

It is clear that the influence of aerosol on cloud formation is contingent upon the atmospheric environment. The recent analysis of lightning climatology over the southeast United States found enhanced lightning frequency over the Houston Metropolitan area, which was attributed to elevated aerosol concentrations in this region [*Orville et al*., 2001]. Houston, Texas has experienced frequent and severe ozone exceedances over the National Ambient Air Quality Standards (NAAQS) [*Lei et al*.,

2004; *Zhang et al.*, 2004b]. Houston hosts one of the world largest petrochemical complexes and several large fossil-fueled electric power plants. Transportation and industry emit a great quantity of VOCs, NO_x, and SO_2. In particular, the Houston Ship Channel region, east of the city center, represents major emission sources of VOCs from petrochemical plants [*Berkowitz et al*., 2004; *Lei et al.*, 2004; *Zhang et al.*, 2004b], which are believed to the major contributor to ozone and secondary organic aerosol (SOA) formation in this region [*Fan et al*., 2005; *Li et al*., 2005; *Zhang et al*., 2004b]. Observations and model simulations indicate that ammonium sulfate and organics contribute to about 30% of total aerosol mass, respectively [*Russell et al.*, 2004, *Fan et al*., 2005]. The observed BC mass concentrations at LaPorte in Houston were high, up to 2.0 μg m^{-3} [*Fast et al.*, 2006], and the simulated mass mixing ratio of BC to ammonium sulfate was high, up to 1:8 [*Fan et al.*, 2005]. Associated with the Texas 2000 Air Quality Study (TexAQS 2000), there exist several ground-based and aircraft measurements of aerosol number size distributions [*Brock et al.*, 2003, *Fast et al.*, 2006]. High aerosol number concentrations (over 10^5 cm^{-3}) have been identified to exist in this area, associated with transportation and industrial activities [*Brock et al.*, 2003]. Moreover, ample convective clouds are generated due to air convergence over land and also possibly by urban heat island (UHI) effect and sea breeze during the warm season [*Orville et al*., 2001]. It is anticipated that aerosols and clouds may exhibit a stronger correlation and interaction in this region.

In addition, the region also has plentiful of observational data for dynamics, cloud and precipitation by several dense observation networks to validate the model

simulations and verify the aerosol effects on the cumulus clouds. There is a very dense rain gauge network that has been used as the NASA's Tropical Rainfall Measuring Mission (TRMM) validation sites. The Texas Commission on Environmental Quality (TCEQ) operated a surface observational network measuring the temperature, moisture, and wind [*Nielsen-Gammon*, 2002; 2003]. During the Texas Air Quality Study (Tex AQS) 2000, NOAA operated a Weather Surveillance Radar 88 Doppler (WSR-88D) system in the Houston-Galveston region, providing the radar observations. Also, a NOAA remote sensing aircraft Twin Otter provided the measurements of cloud properties such as cloud droplet size distribution and liquid water content during Tex AQS 2006. All of those observational data are very useful for investigating the aerosol effects on cloud properties and precipitation.

Relative humidity is another key factor affecting cloud microphysics and dynamics. In air with different water vapor contents, the effects of aerosols on cloud developments and precipitation likely behave distinctly. *Khain et al.* [2005] performed and analyzed a set of experiments with different RH for continental and maritime conditions. In the 3-D cloud simulations with spectral-bin microphysics by *Lynn et al*. [2005a, b], the importance of the ambient RH on the precipitation was addressed. The humid environment and large surface heating in the Houston area [*Fan et al*., 2007a] likely impact the relationship of the aerosol-cloud interactions.

1.3 Spectral-Bin Cloud Microphysics

Two typical cloud microphysical models are used in the cloud-resolving models (CRM): bulk and spectral-bin microphysics (SBM). Bulk schemes calculate the mixing

ratios of liquid and/or ice and are the most popular and least computationally expensive approaches [e.g., *Kessler*, 1969; *Lin et al.*, 1983]. Recently, two-moment bulk schemes, both mass content and the total number concentration are predicted variables, were also developed and can be used for studying the aerosol – cloud interactions. Spectral-bin microphysical schemes explicitly calculate the number concentrations of hydrometeors during the course of the model integration. The utilization of spectral-bin microphysical cloud models offers a useful method to investigate the aerosol effects on the formation of clouds and precipitation [*Khain et al.*, 2000, 2004]. The SBM models at the early stage only include warm rain microphysics [*Clark*, 1973; *Kogan*, 1991; *Stevens et al*., 1996; *Pinsky and Khain*, 2002]. Some SBM models have been then developed in which only one size distribution function is used to describe cloud ice [e.g., *Hall*, 1980; *Khvorostyanov et al*., 1989; *Ovtchinnikov and Kogan*, 2000]. In this approach, the categories with the smallest masses are interpreted as ice crystals, while larger ice particles are usually considered as graupel. There are only a few models of mixed-phase clouds with a detailed description of cloud ice, in which several size distribution functions for different types of cloud ice are formulated [*Takahashi*, 1976; *Khain et al.*, 1996; 1999; 2000; 2004; *Ovtchinnikov et al.*, 2000; *Reisin et al.*, 1996a; 1996b; *Rasmussen et al.*, 2002; *Yin et al.*, 2000a, b]. These state-of-the-art cloud microphysical models potentionally provide more accurate simulations of precipitation formation and simulations of cloud–aerosol interactions. In the SBM models, the aerosol particles are described by a special size distribution function that changes as a result of advection and activation (droplet nucleation). The values of supersaturation are used to determine the

sizes of aerosol particles (playing the role of CCN) to be activated and the corresponding sizes of newly nucleated cloud droplets. Collisions are calculated by solving stochastic equations for size distribution functions.

The SBM models were successfully used for the investigation of separate microphysical processes [e.g., *Takahashi*, 1976; *Reisin et al.*, 1996b; *Ovtchinnikov and Kogan*, 2000], effects of cloud microphysics on spatial redistribution of precipitation in the coastal zones [e.g., *Khain and Sednev*, 1996], simulation of stratiform clouds and their radiative effects [e.g., *Liu and Kogan*, 1998; *Rasmussen et al.*, 2002], and simulation of cloud seeding [e.g., *Khvorostyanov et al.*, 1989; *Reisin et al.*, 1996c], etc. At the same time, a number of studies in which SBM models are used for the investigation of aerosol effects on mixed-phase clouds and precipitation is quite limited. *Khain et al.* [1999] demonstrated a decrease in the rate of warm rain production in deep cumulus clouds with an increase in the CCN concentration using the SBM Hebrew University Cloud Model (HUCM). A substantial improvement in the understanding of many aspects of microphysics, as well as in the formulation of mathematical microphysical algorithms, has been attained in the last few years. *Khain et al.* [2004a,b; 2005] reported aerosol effects on the microphysical structure of deep growing Texas convective clouds and precipitation [*Rosenfeld and Woodley*, 2000] employing the updated HUCM model. In addition, *Yin et al.* [2000b] studied the role of giant CCN on precipitation from convective clouds.

Note that because of computer limitations most mixed-phase SBM models are two-dimensional. Three-dimensional SBM models are either warm rain microphysical

models or contain only one size distribution of description of wide variability of cloud ice. A novel 3D SBM mesoscale model has been recently developed by the implementation of the updated HUCM microphysics into the fifth-generation Pennsylvania State University– National Center for Atmospheric Research (PSU–NCAR) Mesoscale Model (MM5) dynamical framework [*Lynn et al.*, 2005a, b]. Simulations of a rain event over Florida accompanied by a squall line formation showed that the new model drastically improved the precision in the reproduction of the precipitation rate and amount.

1.4 Objective

Our major objective in this study is to investigate the effects of anthropogenic aerosols on deep convective clouds and the associated radiative forcing in the Houston area. The specific tasks of this study are: (1) to investigate the aerosol characteristics such as aerosol composition and number size distribution by using the EPA's Models-3 Community Multi-scale Air Quality model (CMAQ); (2) To apply the aerosol properties into a cloud-resolving model (CRM) developed at National Aeronautics and Space Administration (NASA)/ Goddard Space Flight Center (GSFC) (called Goddard Cumulus Ensemble model or GCE model, see *Tao et al.*, 2003a), which incorporates a spectral-bin microphysics HUCM, to investigate the aerosol indirect effects on cloud properties and precipitation; (3) to investigate the radiative effects of anthropogenic aerosols containing black carbon (BC) by coupling a land surface model and a radiation scheme into GCE. The aerosol indirect effects on the cloud properties are to be looked into under different aerosol compositions, concentrations and size distributions. An

aerosol radiative module is to be developed and coupled with the radiation scheme to on-line calculate the wavelength-dependent aerosol radiative properties based on aerosol composition, size distribution, mixing state and ambient relative humidity. The significance of the aerosol radiative effects (ARE) will be investigated by comparing with the case without consideration of the ARE. The associated direct, semi-direct and indirect radiative forcing of aerosols for deep convective clouds will be estimated, and the sensitivity of cloud properties and radiative forcing to aerosol single-scattering albedo (SSA) will also be examined.

2. MODEL DESCRIPTION AND MODIFICATION*

Simulations of aerosol characteristics such as composition and number size distribution have been performed by using the EPA's Models-3 Community Multiscale Air Quality model (CMAQ), with the aerosol module AERO3 [*EPA*, 1999]. The cloud simulations for aerosol indirect effects have been conducted by employing a cloud-resolving model (CRM) developed at National Aeronautics and Space Administration (NASA)/ Goddard Space Flight Center (GSFC) (referred as to the Goddard Cumulus Ensemble model or GCE model) [*Tao et al.*, 2003a], which incorporates a spectral-bin microphysics Hebrew University Cloud Model (HUCM) [*Khain et al*., 2004]. The simulations for aerosol radiative effects have been conducted by using the above-mentioned GCE model coupled with an updated Goddard radiation scheme containing a newly-developed aerosol radiative module, and a Goddard surface scheme of a Parameterization for Land-Atmosphere-Cloud Exchange (PLACE) [*Baker et al.*, 2001; *Tao et al.*, 2003a]. The description about these models and accordingly modifications are presented as follows.

---

* Reproduced by permission of American Geophysical Union from:
(1) Fan, J., R. Zhang, G. Li, J. Nielsen-Gammon, and Z. Li, Simulations of fine particulate matter ($PM_{2.5}$) in Houston, Texas, J. Geophys. Res., 110, D16203, doi:10.1029/2005JD005805, 2005.
(2) Fan, J., R. Zhang, D. Collins, and G. Li, Contribution of Secondary Condensable Organics to New Particle Formation: A Case Study in Houston, Texas, Geophys. Res. Lett., 33, L15802, doi:10.1029/2006GL026295, 2006.
(3) Fan, J., R. Zhang, G. Li, W.-K. Tao, and X. Li, Simulations of cumulus clouds using a spectral microphysics cloud-resoving model, J. Geophys. Res., 112, D04201, doi:10.1029/2006JD007688, 2007.
(4) Fan, J., R. Zhang, G. Li, and W.-K. Tao, Effects of aerosols and relative humidity on cumulus clouds, J. Geophys. Res., doi:10.1029/2006JD008136, in press.

2.1 Models-3/CMAQ

2.1.1 Model description

Models-3/CMAQ is a third-generation air quality modeling and assessment tool designed to support air quality modeling applications ranging from regulatory issues to science inquiries on atmospheric science processes [*EPA*, 1999]. The CMAQ aerosol component, or module, designed to simulate the complex processes involving PM, is derived from the Regional Particulate Model (RPM) [*Binkowski and Shankar*, 1995], an extension of the Regional Acid Deposition Model (RADM) [*Chang et al.*, 1991]. The aerosol species considered within the CMAQ aerosol module (AERO3) include sulfate, nitrate, ammonium, water, primary organic aerosol, secondary organic aerosol of both anthropogenic and biogenic origins, elemental carbon, primary material not otherwise specified and wind-blown dust [*Binkowski and Roselle*, 2003]. Two different modes, the Aitken and accumulation modes, each having variable standard deviations, represent PM2.5 particles in the CMAQ aerosol module. Conceptually, the Aitken mode represents fresh particles resulting from nucleation and/or direct emissions. The accumulation mode denotes aged particles. Detailed descriptions of the algorithms of this module have been presented previously [*Binkowski and Roselle*, 2003; *Jiang and Roth,* 2003]. The model performance for visibility and the mass concentrations of speciated aerosols such as organic carbon, sulfate and nitrate has been extensively evaluated against the observations [*Arnold*, 2003; *Eder et al.*, 2000; *Jun and Stein*, 2004; *Mebust et al.*, 2003; *Park et al*., 2005].

The aerosol particle size distribution is modeled using the concepts developed by

Whitby [1978]. That is, $PM_{2.5}$ is treated by two interacting subdistributions or modes. The coarse particles form a third mode. Conceptually within the fine group, the smaller (nuclei or Aitken), i-mode represents fresh particles either from nucleation or from direct emission, while the larger (accumulation), j-mode represents aged particles. Primary emissions may also be distributed between these two modes. The two modes interact with each other through coagulation. The particle production mechanism employed in the CMAQ aerosol module is the classical binary H_2SO_4–H_2O nucleation model parameterized by *Kulmala et al.* [1998] (referred to as the BN Scheme hereinafter). The predicted binary sulfuric acid-water nucleation rates are many orders of magnitude lower than observed in atmospheric nucleation events [*Kulmala et al.*, 1998]. Recent studies on the model performance for the aerosol number concentrations indicate that CMAQ underestimated the aerosol number concentrations of Aitken mode by a factor of 10-100 [*Elleman et al.*, 2004; 2005].

2.1.2 Model modification

Although CMAQ was evaluated to predict reasonably good mass concentrations of aerosols, it underestimated the aerosol number concentrations of Aitken mode by a factor of 10-100 [*Elleman et al.*, 2004; 2005], resultant from the much lower nucleation rates predicted by the binary sulfuric acid-water nucleation theory relative to the observed ones in the atmosphere. Recently, the condensable organic acids, produced from atmospheric oxidation of hydrocarbons, were suggested to play an important role in particle nucleation [*Zhang et al.*, 2004a]. Observation studies also indicated the enhanced production of ultrafine particles in plumes rich in both H_2SO_4 and VOCs

[*Alam et al.*, 2003; *Kulmala et al.*, 2004]. In the Houston area, secondary organic compounds are the most important components of aerosols [*Allen,* 2002; *Russell et al.*, 2004; *Fan et al*., 2005]. In order to represent the reasonable nucleation rates in Houston, a nucleation scheme that accounts for the co-nucleation effects of H_2SO_4 and secondary condensable organics [*Zhang et al*., 2004a] has been incorporated into the CMAQ aerosol module (refereed to as the ON scheme hereinafter). The nucleation rate (J_r) in the ON scheme is assumed to be dependent of the partial pressures of sulfuric acid and secondary condensable organics, with a parameterized equation,

$$J_r = C \cdot P_{H_2SO_4} \cdot (r_{org,a} + r_{org,b}) \qquad (1)$$

where $r_{org,a} = \sum_{i=1}^{8} P_{i.,org}$ and $r_{org,b} = \sum_{i=9}^{10} P_{i.,org}$. $P_{i.,org}$ denotes the concentrations of condensable organic species considered in the CMAQ aerosol module, and *a* and *b* represent the contributions from anthropogenic sources and biogenic sources, respectively. There are totally ten secondary condensable organics, consisting of primarily organic acids produced from oxidation of alkanes, olefins, aromatics, and terpenes. The concentrations of sulfuric acid and secondary condensable organics are predicted by CMAQ, with the typical concentrations of ~10^7 cm^{-3} for sulfuric acid and ~10^{12} – 10^{13} cm^{-3} for secondary condensable organics. *C* is a constant inferred from the above parameterized equation using the typical nucleation rate (~10^6- 10^7 m^{-3} s^{-1}) measured in the urban atmosphere [*Kulmala et al.*, 2004] and the CMAQ predicted concentrations of H_2SO_4 and secondary condensable organics, with a value of 3×10^{-25} m^3 s^{-1}. Considering the large uncertainties in our understanding of atmospheric new

particle formation in experimental, theoretical, and modeling studies, such a parameterization represents a reasonable approach to account for the organic effect in new particle formation.

2.2 GCE Cloud-Resolving Model

2.2.1 Model description

The GCE model employed is two-dimensional and nonhydrostatic. The equations for the velocity components u and w, as well as the mass continuity equation, are reduced to an elliptic equation for the pressure. The thermodynamic equations include the equation for the potential temperature θ and the water vapor–dry air mixing ratio q. The equation system is based on the deep convection approximation [*Ogura and Phillips*, 1962]. A multi-dimensional positive definite advection transport algorithm [*Smolarkiewicz and Grabowski*, 1990] avoids decoupling between mass and number concentration of cloud species. The positive definite advection scheme also produces more light precipitation, which is in better agreement with observations [*Johnson et al.*, 2002]. Subgrid-scale (turbulent) processes in the GCE model are parameterized using a scheme based on *Klemp and Wilhelmson* [1978], and the effects of both dry and moist processes on the generation of subgrid-scale kinetic energy are incorporated [*Soong and Ogura*, 1980]. More details on the descriptions of the microphysical and dynamical processes of the CRM have been discussed by *Tao and Simpson* [1993] and *Tao et al.* [2003a].

The coupled spectral-bin model HUCM is based on solving an equation system for eight number size distributions for water drops, ice crystals (columnar, plate-like and

dendrites), snowflakes, graupel, hail/frozen drops and CCN. Each size distribution is represented by 33 mass doubling bins. Explicit descriptions of nucleation of CCN, ice nucleation, diffusional growth (condensation, evaporation, deposition, and sublimation) of all hydrometeors, freezing of water drops, ice particle melting, collision/coalescence of drop-drop, drop-ice, and ice-ice are represented in this bin scheme. Details of the bin model can be found in *Khain and Sednev* [1996], *Khain et al.* [2000], *Khain et al.* [2004], and *Khain et al.* [2005]. The model microphysics is specifically designed to take into account the effect of atmospheric aerosols on cloud development and precipitation formation, as well as the effects of clouds on aerosol/CCN concentration in the atmosphere.

In the original SBM, the initial aerosol size distribution is calculated by an empirical formula: $N = N_0 S_w^k$ [*Pruppacher and Klett*, 1997], where S_w is the supersaturation with respect to water. At each time step a value of S_w is calculated at all grid points. Using the value of S_w, a critical aerosol/CCN radius is calculated according to the Köhler theory. Aerosols/CCNs with radii exceeding the critical value are activated. The size of fresh nucleated droplets is calculated as follows. In the case where the radii of aerosol/CCN $r_N < 0.03$ μm, the equilibrium assumption for the condensation growth is used to calculate the radius of a nucleated droplet corresponding to r_N (see *Khain et al.* [2000] for more details). In the case of $r_N > 0.03$ μm, the radius of the nucleated water droplet is assumed to be equal to 5 times as much as $5r_N$ [*Kogan*, 1991; *Khain et al.*, 1999, 2004, 2005; *Yin et al.*, 2000a, b]. Since large aerosol/CCN does not reach their

equilibrium size at the cloud base, this approach prevents the formation of unrealistically large droplets and inhibits raindrop formation that is too fast.

2.2.2 Model updates and modification

2.2.2.1 CCN activation

The original CCN activation scheme in the SBM is the simple Köhler theory for single-component aerosols such as ammonum sulfate. In order to represent the CCN activation in reality and investigate the effect of aerosol compositions on clouds, two other activation schemes modified from the Köhler theory have been coupled with the SBM. A modified Köhler theory for multiple components has been applied to calculate CCN activation, assuming all of the components are water soluble [*Shulman et al.*, 1996]. The critical supersaturation (S_{crit}) for each bin is calculated from the modified Köhler theory. The aerosol particles with the critical supersaturation $S_{crit} < S_w$ within the bins are activated. We assume that the aerosol composition consisted of $(NH_4)_2SO_4$ and soluble organics. The effect of surface tension caused by organic compounds is taken into account when calculating CCN activation and the algorithm is taken from *Mircea et al.* [2005]. Another activation scheme is a reformulation of the Köhler theory to include the effect of slightly soluble substances and soluble gases (i.e., HNO_3), which has been coupled to calculate CCN activation for the aerosols with insoluble or slightly soluble substances [*Laaksonen et al.*, 1998]. The growth curve of aerosol particles within each bin is calculated by the reformulation of the Köhler theory and the maximum supersaturation (S_{max}) is defined as the critical supersaturation. The aerosol particles with the critical supersaturation $S_{max} < S_w$ within the bins are activated and transformed into

cloud droplets. The aerosol composition in our test is assumed to be $(NH_4)_2SO_4$ and slightly soluble organics (SSO) with the solubility of 0.001 kg/(kg of water). The slightly soluble organics is the core coated with ammonium sulfate. The above three activation schemes correspond to three aerosol composition cases in cloud simulations and will be discussed later.

2.2.2.2 PLACE surface model and Goddard radiation scheme

In order to investigate the aerosol radiative effects on clouds and the associated radiative forcing, the GCE model has been updated by being incorporated with an improved Goddard radiation scheme and a Goddard surface scheme of a Parameterization for Land-Atmosphere-Cloud Exchange (PLACE) [*Baker et al.*, 2001; *Tao et al.*, 2003a].

The PLACE model is a detailed interactive process model of the heterogeneous land surface (soil and vegetation) and adjacent near-surface atmosphere. PLACE consists of linked process models (e.g., net radiation, evapotranspiration, ground heat storage) and emphasizes the vertical transport of moisture and energy through the 5 layer soil moisture and the 7 layer soil temperature column to the overlying heterogeneous land surface. The additional two soil temperature layers are used to aid in resolving large temperature gradients near the surface. Momentum, sensible, and latent heat fluxes are calculated using similarity relationships [*Zilitinkevich*, 1975; *Businger et al*., 1991]. More details on the description of PLACE can be found in *Wetzel and Boone* [1995]. The atmospheric component of the GCE cloud model provides surface winds, surface air temperature, surface pressure, moisture, shortwave and longwave radiation, and

precipitation to the land surface model (PLACE). The land surface component returns momentum, sensible heat, and latent heat fluxes to the atmosphere. The coupling is two-way interactive. Both 2-D and 3-D GCE coupled with the PLACE model has previously been used to investigate landscape-generated deep convection [*Lynn et al*., 1998; *Baker et al*., 2001] and the sensitivity of convection to land cover in the semi-arid regions of West Africa [*Mohr et al*., 2003; *Alonge et al*., 2007].

The improved Goddard radiation scheme includes shortwave and longwave radiation models [*Tao et al*., 2003a, b]. The shortwave radiation model of *Chou and Suarez* [1999] is used to compute the solar fluxes due to absorption and scattering by clouds, aerosols and gases (including water vapor). Fluxes are integrated virtually over the entire spectrum, from 0.175 to 10 μm. The spectrum is divided into seven bands in the ultraviolet (UV) region (0.175–0.4 μm), one band in the photosynthetically active radiation (PAR) region (0.4–0.7 μm), and three bands in the near infrared region (0.7–10.0 μm). In the UV and PAR region, a single O_3 absorption coefficient and a Rayleigh scattering coefficient are used for each of the eight bands. In the infrared, the k-distribution method is applied to compute the absorption of solar radiation. Reflection and transmission of a cloud and aerosol-laden layer are computed using the δ-Eddington approximation. Fluxes for a composite of layers are then computed using the two-stream adding approximation. The longwave radiation parameterizations developed by *Chou et al*. [1999] and *Kratz et al*. [1998] are implemented into the GCE model. The IR spectrum is divided into nine bands. In addition, a narrow band in the 17 μm region is added to compute flux reduction due to N_2O. As in the solar spectral region, the *k*-

distribution method with temperature and pressure scaling is used to compute the transmission function in the weak absorption bands of water vapor and minor trace gases (N_2O, CH_4, CFC's). A look-up table method is used to compute the transmission function in the strong absorption bands.

2.2.2.3 Aerosol radiative module

The wavelength-dependent aerosol radiative properties such as AOD (τ), SSA (σ), and AF (*g*) are the key factors to determine the aerosol radiative effects on clouds and associated forcing. Instead of using the fixed aerosol radiative properties during the simulations as in some previous studies [e.g., *Johnson et al.*, 2004; *McFarquhar and Wang*, 2006], an aerosol radiative module has been developed and incorporated into the radiation scheme to online calculate the aerosol radiative properties as a function of wavelength (λ) based on the aerosol composition, size distribution, mixing state, and ambient relative humidity. The module includes the methodologies for the external and core-coated internal mixing states. The calculations of aerosol radiative properties for the core-coated internal mixture are presented below.

For the internally mixed aerosol components, the complex refractive index of aerosol particles is calculated based on the volume-weighted average of the individual refractive index [*Hänel*, 1976]. The real and imaginary parts of the complex refractive index, denoted by $\bar{n}(i,\lambda)$ and $\bar{k}(i,\lambda)$, respectively, for aerosols in a size bin (*i*) at a certain wavelength (λ) are determined by:

$$\bar{n}(i,\lambda) = \sum_{l=1}^{m} n(l,i,\lambda) f(l)\,,\ \bar{k}(i,\lambda) = \sum_{l=1}^{m} k(l,i,\lambda) f(l) \qquad (2)$$

where m is the number of aerosol components and $f(l)$ is the volume fraction of the component (l). The Mie theory [*Bohren and Huffman*, 1983] is employed to calculate the extinction efficiency (Q_e), scattering efficiency (Q_s), and asymmetry factor (g) as functions of the size parameter, $x = 2\pi r / \lambda$, where r is the particle's wet radius. The hygroscopic growth of a water-soluble component at a certain ambient humidity is calculated by the relation defined by *Mallet et al*. [2004],

$$r_{g,a(o)} = r_{g,a(b)}(1-h)^e \tag{3}$$

where h is the relative humidity. The coefficient e depends on the considered type of aerosol. It is equal to 0.25 for particulate organic matter [*Chazette and Liousse*, 2001], and 0.285 for ammonium sulfate, nitrate, and sea salt [*Hänel*, 1976]. To avoid repeated Mie calculations, the first step of this methodology is to obtain a look-up table containing aerosol optical properties, i.e., Q_e, σ, and g, over all size ranges covered by 33 bins and a set of refractive indices that represent a range of indices typical of atmospheric aerosols by performing full Mie calculations. In all subsequent calls to this algorithm, the Mie calculations are skipped, and the Q_e, σ, and g for an aerosol particle are obtained by interpolating linearly from the look-up table with the calculated complex refractive index and size parameter.

The aerosol optical depth ($\tau(\lambda, j)$) at a certain λ and atmospheric layer (j) is calculated by integration over the aerosol particles in all of 33 size bins and given by

$$\tau(\lambda, j) = \sum_{i=1}^{33} Q_e(\lambda, r_i)\pi r_i^2 n(r_i, j) dz_j \tag{4}$$

where $n(r_i, j)$ represents the aerosol number concentrations and dz_j is the height of the atmospheric layer. It is noted that r_i is the wet particle radius, corrected with the hygroscopic growth and calculated with eq. (3). Assuming $\tau(\lambda, r_i, j) = Q_e(\lambda, r_i)\pi r_i^2 n(r_i, j)dz_j$, the weighted-mean values of SSA (σ) and AF (g) for the aerosol mixture at a certain wavelength and layer are then calculated by

$$\sigma(\lambda, j) = \sum_{i=1}^{33} \tau(\lambda, r_i, j)\sigma(\lambda, r_i, j) \Big/ \sum_{i=1}^{33} \tau(\lambda, r_i, j) \qquad (5)$$

$$g(\lambda, j) = \sum_{i=1}^{33} \tau(\lambda, r_i, j)\sigma(\lambda, r_i, j)g(\lambda, r_i, j) \Big/ \sum_{i=1}^{33} \tau(\lambda, r_i, j)\sigma(\lambda, r_i, j) \qquad (6)$$

For the externally mixed aerosol components, the aerosol radiative properties τ, σ, and g are calculated for each component first, and the ensemble aerosol radiative properties for the total aerosol population are summed over all of the components [*Wolf*, 2006].

Once the wavelength-dependent aerosol radiative parameters τ, σ, and g are found, they are transferred to the shortwave and longwave radiative transfer models, and then interact with the other components of GCE such as dynamical, microphysical, and surface processes along with the cloud radiative properties.

3. AEROSOL CHARACTERISTICS*

Aerosols act as cloud condensation nuclei (CCN) and their properties such as the chemical composition, size distribution, and number concentration are the important factors in determining cloud properties. Associated with the TexAQS 2000 and the Houston Supersite Project, the aerosol characteristics have been investigated by model simulations from the EPA's Models-3/CMAQ system with aerosol modules [*Fan et al*., 2005; 2006]. The results have been compared with the limited observational data.

3.1 Description of Numerical Experiments

Aerosol mass concentrations and compositions are simulated with the CMAQ Version 4.3 coupled with the aerosol module AERO3 [*EPA*, 2003]. The meteorological fields for chemical transport simulations are generated during TexAQS 2000 by *Nielsen-Gammon* [2003] using MM5 with domain of 600× 540 km^2 and horizontal resolution of 4 km, which incorporate the GOES satellite data. The emission inventory used in this study is from the EPA's National Emission Inventory (NEI99) final version 3. More details about model configuration can be found in *Fan et al*. [2005].

---

* Reproduced by permission of American Geophysical Union from:
(1) Fan, J., R. Zhang, G. Li, J. Nielsen-Gammon, and Z. Li, Simulations of fine particulate matter ($PM_{2.5}$) in Houston, Texas, J. Geophys. Res., 110, D16203, doi:10.1029/2005JD005805, 2005.
(2) Fan, J., R. Zhang, D. Collins, and G. Li, Contribution of Secondary Condensable Organics to New Particle Formation: A Case Study in Houston, Texas, Geophys. Res. Lett., 33, L15802, doi:10.1029/2006GL026295, 2006.

The study domain in Houston covers the latitude from 29.60N to 29.96N and longitude from 95.62W to 95.02W (the inner box in Figure 3.1), since the relatively higher $PM_{2.5}$ mass concentrations above the annual average standard frequently occurred in this area. The hourly $PM_{2.5}$ measurements with Tapered Element Oscillating Microbalance (TEOM) and Federal Reference Method (FRM) during the Houston Supersite Project provide valuable data to evaluate modeling results in southeast Texas [*Allen*, 2002; *Russell et al.*, 2004]. Figure 3.1 shows the locations of the sites for TEOM and FRM measurements within the study domain.

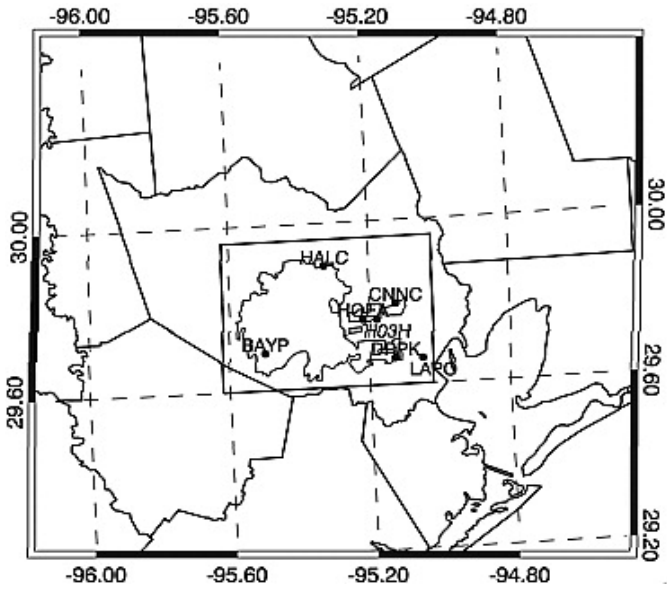

Figure 3.1 The study domain and PM monitoring sites in the Houston area.

Aerosol number concentration and size distribution are simulated with the incorporated organic nucleation scheme (ON) described in Section 2.1.2 that accounts for the enhanced nucleation effect of secondary condensable organics. The results are

compared with those with only the original binary nucleation scheme (BN) and the available observations. Ground-level measurements are only from one site located in Northeast Houston (Aldine, N29.90 and W95.33), made with a differential mobility analyzer (DMA) system [*Gasparini et al.*, 2004]. The aircraft aerosol data are collected using a DMA on board the instrumented Southern Ogallal Aquifer Rainfall (SOAR) Cheyenne II aircraft during a flight on August 23, 2004.

3.2 Aerosol Mass Concentrations and Composition

The diurnal variation of $PM_{2.5}$ mass concentration averaged over the study domain and over eight simulated days is depicted in Figure 3.2. A strong maximum with the highest concentration about 21.0 $\mu g/m^3$ occurs around 8:00 am, and a weaker maximum (13.0 $\mu g/m^3$) takes place around 8:00 pm. The temporal variation of $PM_{2.5}$ at different locations is consistent throughout the region. Averaged over the seven monitoring sites in Houston, the daily $PM_{2.5}$ mass concentrations are about 8.5-13.0 $\mu g/m^3$, in agreement with the TEOM observed values, 8.0-14.0 $\mu g/m^3$. The modeled hourly $PM_{2.5}$ mass concentrations are compared with the available TEOM measurements. Figure 3.3 presents the comparisons of modeled hourly $PM_{2.5}$ mass concentrations averaged over the simulation period against the measurements for the CNNC site. Generally, the model simulations of hourly $PM_{2.5}$ concentrations are reasonable compared with the observations. The model reproduces the diurnal variations, although the predicted peak time is about 1-2 hour later than the observed. The model overpredicts the morning peaks and underestimated the $PM_{2.5}$ concentrations

in the afternoon for all sites. The strong emissions, low calculated PBL heights, and rapid photochemical activity after sunrise, are responsible for the strong morning peak.

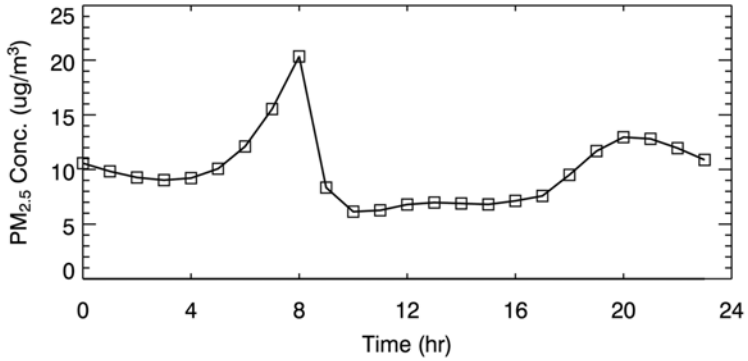

Figure 3.2 Simulated $PM_{2.5}$ mass concentrations averaged over the study domain and the episode.

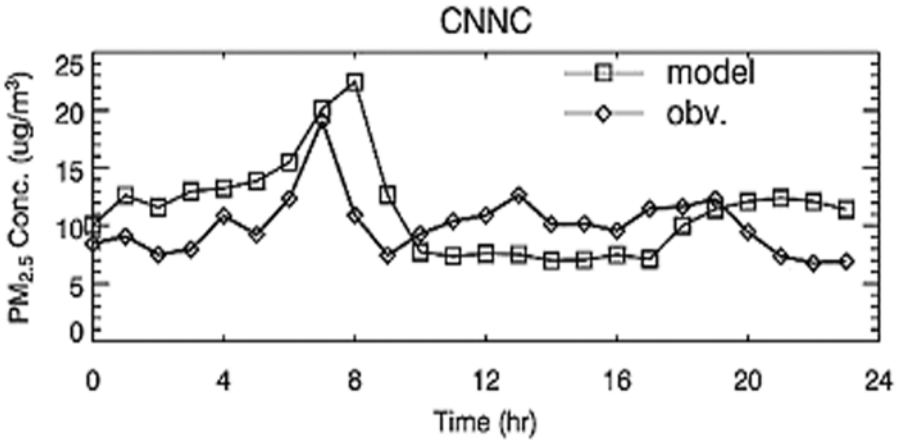

Figure 3.3 Comparisons of the simulated and measured hourly $PM_{2.5}$ mass concentrations for CNNC site.

The averaged $PM_{2.5}$ mass composition is presented in Figure 3.4. Sulfate, organic carbon, elemental carbon and ammonium are the major constituents of $PM_{2.5}$ in the

Houston area. Sulfate consists of about 30% of the total average $PM_{2.5}$ mass. Organic carbon and elemental carbon makes up about 32% of the total $PM_{2.5}$ mass. Ammonium and nitrate account for about 10% and 1% of the total $PM_{2.5}$ mass, respectively.

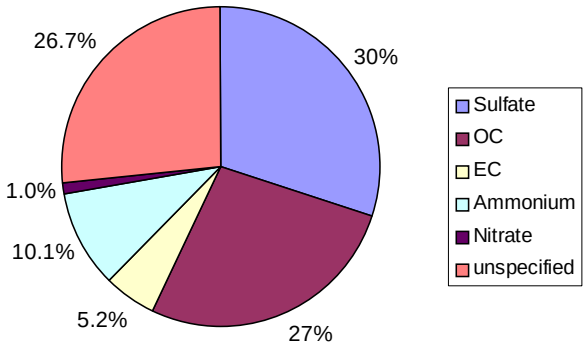

Figure 3.4 Chemical compositions of simulated $PM_{2.5}$ in the Houston area averaged over the study domain and the episode.

The site-by-site comparisons of compositions against FRM measurements are presented in Table 3.1. The simulated mass concentrations of the components are in good agreement with the observations except for nitrate. For organic carbon, sulfate, elemental carbon, and ammonium, the normalized mean biases (NMB) are –17.4%, -20.76%, 9.06%, and 24.20%, respectively. Those values are less than ±25%, indicating good agreement. The NMB value for nitrate is -61.46%, indicating a significant underestimation for nitrate. The uncertainty in aqueous chemistry may be responsible for the underprediction by the model.

The geographical distribution of black carbon (i.e., EC) indicates very spatially inhomogeneity (not shown) and high concentrations, up to 2.0 $\mu g/m^3$, consistent with the

observations [*Fast et al.*, 2006]. The simulated mass mixing ratio of black carbon to ammonium sulfate is up to 1:8.

Table 3.1 Site-by-site comparisons of the major components of $PM_{2.5}$ between modeled and observed values

Sites	OC ($\mu g/m^3$)		Sulfate ($\mu g/m^3$)		Nitrate ($\mu g/m^3$)		EC ($\mu g/m^3$)		Ammonium ($\mu g/m^3$)	
	Obs.	model	Obs.	model	Obs.	model	Obs.	model	Obs.	model
CNNC	3.00	2.20	4.05	5.02	0.22	0.11	0.46	0.45	0.86	1.08
BAYP	2.50	3.03	3.59	1.79	0.34	0.12	0.32	0.62	0.64	0.60
DRPK	2.50	2.02	4.08	2.33	0.36	0.10	0.34	0.39	0.73	0.76
H03H	3.74	3.04	4.95	5.37	0.40	0.14	0.61	0.59	1.04	1.80
LAPO	2.45	1.70	4.33	2.70	0.39	0.09	0.40	0.35	0.80	0.98
HALC	3.88	3.00	4.10	2.68	0.30	0.19	0.58	0.56	0.75	0.96
mean	3.01	2.50	4.18	3.32	0.34	0.13	0.45	0.49	0.80	1.03
Mean Bias	-0.51		-0.87		-0.21		0.04		0.23	
NMB (%)	-17.40		-20.76		-61.46		9.06		24.20	

3.3 Aerosol Number Concentrations and Size Distribution

Figure 3.5 shows a comparison of the predicted number size distributions from the two schemes with ground-level aerosol measurements at the Aldine Site, which are averaged over the daytimes (from 8 am to 6 pm) during the 8-day episode. The aerosol number size distributions averaged over the entire Houston area and over the daytimes during the episode from the two schemes are similar to those shown in Figure 3.5. There exists a significant difference in the number concentrations for particles smaller than 50 nm between the two schemes. The ON scheme predicts over one order of magnitude

higher number concentrations than the BN for the nucleation mode particles (< 11 nm). Clearly, the BN scheme fails to simulate the measured high number concentrations of ultrafine particles, while the ON scheme yields concentrations in good agreement with the measured values.

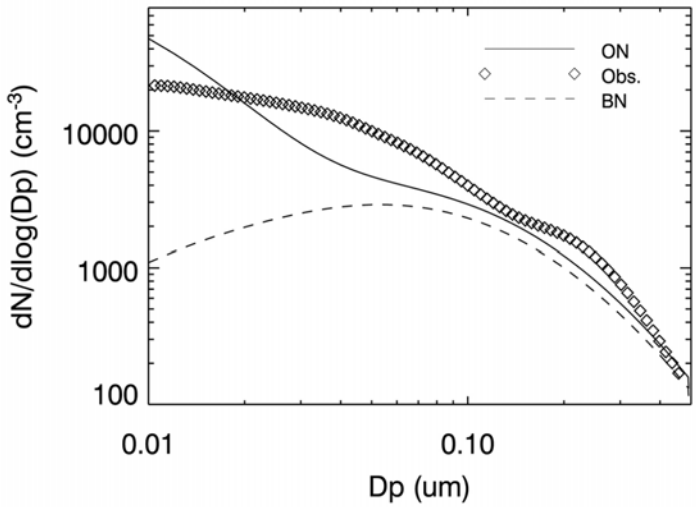

Figure 3.5 Comparison of aerosol simulations with the ground-level measurements at the Aldine site.

The diurnal variations of measured and simulated number size distributions averaged over the eight simulation days also reveal that the ON scheme reasonably reproduced the ultrafine particle concentration especially in the afternoon and the BN scheme fails to predict the new particle formation. Please refer to *Fan et al.* [2006] for figures and more details.

The diurnal variations of predicted and observed total number concentrations at the Aldine site averaged over the episode are shown in Figure 3.6. The particle number

concentrations predicted by the ON scheme are in good agreement with the measurements during the daytime, which are over 10^4 cm^{-3}, while the BN scheme considerably underestimates the particle number concentrations during the daytime, especially in the afternoon, by a factor of about 10. The high aerosol concentrations of over 10^5 cm^{-3} occur frequently. The results imply that co-nucleation between sulfuric acid and condensable organics likely accounts for the observed new particle formation event during the afternoon hours because of high concentrations of sulfuric acid and condensable organics resulting from photochemical oxidation of volatile organic compounds. The nighttime particle concentration may be controlled by a different nucleation mechanism [*Laaksonen et al.*, 2005]. The ON scheme can not account for the nighttime particle concentrations.

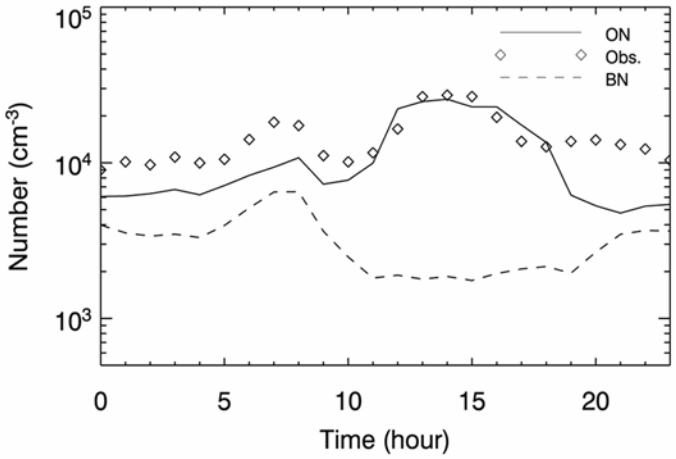

Figure 3.6 Comparison of diurnal variations of total number concentrations averaged over the episode.

Comparison of the number size distributions predicted by the two schemes with the aircraft measurements is presented in Figure 3.7. The aircraft data are averaged over a flight path to the north of Houston (from N30.135, W95.760 to N30.14, W 95.05) at the altitudes of 630 – 650 m. The predictions by the ON scheme agree reasonably well with the aircraft measurements, but the number concentrations of ultrafine particles predicted by the BN scheme are substantially smaller than those measured.

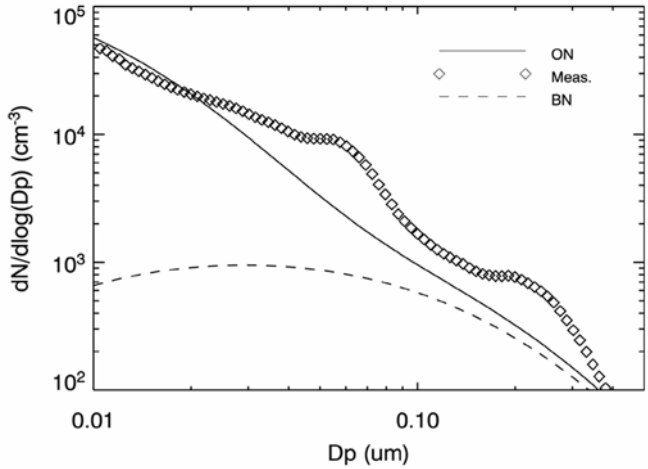

Figure 3.7 Comparison of number size distribution (dN/dlog(D_p)) averaged over a selected flight path.

The increases in mass concentrations of sulfate and organic carbon from the binary scheme BN to organic scheme ON are very small (generally less than 5%), since the number concentrations are only significantly enhanced for the particles with the diameter of less than 0.1 μm, which contribute to mass negligibly.

3.4 Summary

The major components of the fine particulate matter in the area are sulfate, organic carbon, elemental carbon and ammonium with the predicted mass contents of

about 30%, 27%, 5%, and 10% of total $PM_{2.5}$ mass, respectively. The black carbon mass concentrations are high, up to 2.0 μg m^{-3} and spatially inhomogeneous. The predicted daily $PM_{2.5}$ mass concentrations are about 8.5-13.0 μg/m^3, comparable to the measured values, 8.0-14.0 μg/m^3. The diurnal patterns of $PM_{2.5}$ mass concentrations are consistent nearly throughout the region, with a strong morning peak and a weaker peak in the late afternoon to the early evening. A parameterized organic nucleation scheme accounting for the co-nucleation effect of sulfuric acid and secondary condensable organics predicts number concentrations of ultrafine particles in agreement with the measurements and reasonably reproduces the measured diurnal variation. The results support that secondary condensable organics are important in new particle formation when sulfate and organics are abundant. The average total aerosol number concentrations during the daytime are over 10^4 cm^{-3}, with the high values of over 10^5 cm^{-3} frequently.

4. AEROSOL INDIRECT EFFECTS ON DEEP CONVECTIVE CLOUDS*

Aerosol indirect effects on cumulus cloud formation and development in the Houston area have been investigated separately without consideration of aerosol radiative effects [*Fan et al.*, 2007a, b]. The obtained aerosol characteristics in this region have been incorporated into the GCE cloud model. A convective cloud event occurring on August 24, 2000 in Houston, Texas has been simulated and the model results have been compared with available radar and rain gauge measurements. First, the effects of aerosol chemical properties such as composition and solubility on the convective clouds have been investigated. Then, the responses of clouds and precipitation to different aerosol types and concentrations have been studied. Finally, we have looked into the aerosol indirect effects on the cumulus clouds under different relative humidity (RH).

4.1 Simulations of a Convective Cloud Event and Effects of Aerosol Chemical Compositions

4.1.1 Design of numerical experiments

The initial aerosol size distributions used in the cloud simulations are from the modeled results of EPA Models-3/CMAQ (Figure 4.1a) [*Fan et al.*, 2005; 2006]. The modeled size distributions are compared with measured data shown in Figure 4.1a. Data

---

* Reproduced by permission of American Geophysical Union from:
(1) Fan, J., R. Zhang, G. Li, W.-K. Tao, and X. Li, Simulations of cumulus clouds using a spectral microphysics cloud-resoving model, J. Geophys. Res., 112, D04201, doi:10.1029/2006JD007688, 2007.
(2) Fan, J., R. Zhang, G. Li, and W.-K. Tao, Effects of aerosols and relative humidity on cumulus clouds, J. Geophys. Res., doi:10.1029/2006JD008136, in press.

collected aboard the Electra aircraft from a five-channel condensation particle counter (CPC), a laser optical particle counter (OPC), and a white-light OPC were combined to determine dry particle size distributions from 0.004 to 8 μm diameter with 1-s time resolution [*Brock et al.*, 2003]. Figure 4.1a indicates that the modeled aerosol size distributions agree well with the observations. An exponential decrease has been widely used for the height dependence of the aerosol concentration in model simulations [e.g., *Khain et al.*, 1999, *Khain et al.*, 2000]. Figure 4.1b presents the exponential decrease of aerosol concentrations with height used as the initial condition at $t = 0$, when there was no convection and no clouds (the fitted line): $N_0 = N_0(z=0)\exp((z-z_0)/\Delta z)$, where z_0 = 2.0 km and Δz =1.2 km, which are obtained from the CMAQ simulation. When convection develops, convective motions determine the spatial distribution of aerosols.

Three numerical experiments, in which different aerosol chemical compositions are assumed and different CCN activation scheme is employed, are conducted to evaluate the effect of aerosol chemical properties on cumulus development. As described in Section 2.2.2, the aerosol composition in the first case consists of only $(NH_4)_2SO_4$ and therefore the simple Köhler theory is employed to calculate CCN activation (referred to as "NS"). In the second test, the aerosol composition is assumed to consist of $(NH_4)_2SO_4$ and soluble organics (NSOR). The corresponding activation scheme is the modified Köhler theory for multiple components. In the third case, the aerosol composition is assumed to be $(NH_4)_2SO_4$ and slightly soluble organics (SSO) with the solubility of 0.001 kg/(kg of water) (NSORs). Therefore, the CCN activation is calculated using a reformulation of the Köhler theory to include the effect of slightly soluble organics and

soluble gases (i.e., HNO_3). In the simulations, the mass mixing ratio between the two components within each bin is about 1:1 estimated from the CMAQ simulations [*Fan et al.*, 2005]. The HNO_3 concentrations are also from the model simulations by CMAQ [*Fan et al.*, 2005; 2006].

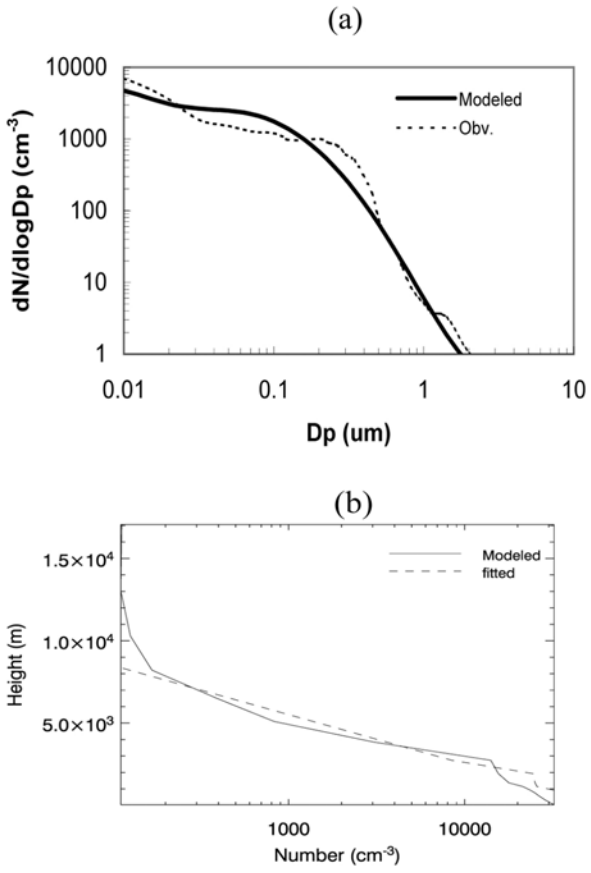

Figure 4.1 (a) Aerosol size distribution, and (b) vertical aerosol profile.

The CCN activation spectra for the three cases are shown in Figure 4.2. For a given S_w larger than 0.05%, the NS scheme yields the most activated aerosol particles and the NSORs yields the least. The differences in the cumulative activated aerosol

particles between NS and NSOR schemes are less significant, partially because of the effect of reduced surface tension of organics in NSOR. NSORs predicts a little more activated aerosols at a very low supersaturation, i.e., less than 0.05%, because the solubility effect is negligible at such low supersaturation and the effect of soluble gas (HNO_3) causes the decrease of the critical radius for CCN activation. Generally, the supersaturation in the simulated cloud case was larger than 0.05%. Since the observations and model simulations indicate that ammonium sulfate and organics are the major components of aerosol in Houston [*Fan et al.*, 2005], soot, dust, and sea salt aerosols are not considered in this study.

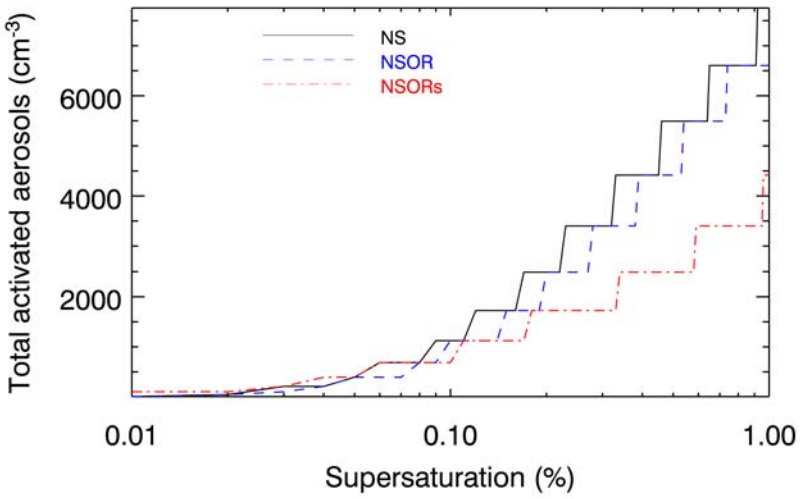

Figure 4.2 CCN activation spectra of NS, NSOR, and NSORs.

The 2-D GCE model was used. The computational domain comprised 1024 × 33 grid points with a horizontal resolution of 500 m. There were 33 stretched vertical levels with a resolution of 250 m at the lowest level and 1260 m at the top. Open boundary

conditions were used at the lateral boundaries. Vertical velocities were assumed to be zero at the upper and lower boundaries

A deep convective event with precipitation occurring on August 24, 2000 in Houston, Texas is simulated. The corresponding sounding data in Houston at the site with the longitude of -95.54 and latitude of 29.95 are shown in Figure 4.3, as used in the simulations. The vertical temperature and dew point profiles reveal instability in the atmosphere, with a convective available potential energy (CAPE) of 960 J kg^{-1} integrated from the surface. The surface temperature is about 31°C and the surface relative humidity is about 60%. The cloud base and freezing level are about 1.8 km and 4.7 km, respectively, on the basis of the sounding. The total integration time in the simulations is 180 minutes with a 6 s time step.

In all simulations the development of the cumulus clouds is triggered by a warm bubble within a 20-km-wide region, with the initial vertical atmospheric profiles depicted in Figure 4.3. The maximum heating temperature is 5°C at the height of 3 km. Such heating results in a relatively strong updraft and formation of the convective clouds.

4.1.2 Results

The results of cloud properties from three numerical simulations with different aerosol chemical compositions are compared with observations from WSR-88D radar and rain gauge data in Houston (Table 4.1). NSORs predict a shorter cell lifetime, a smaller cell core size and a lower maximum accumulated rain than those predicted from NS and NSOR. The values of the cell life and cell core size predicted by NSORs are 140 min and 14 km, respectively, in good agreement with the observational data of 120 min

and 12 km. The maximum accumulated precipitation in NSORs is 23.3 mm, also in agreement with observed value of 21.1 mm. The corresponding values of the cell size, cell lifetime and precipitation in NS and NSOR are noticeably higher than the observations. It is evident that NSORs, in which aerosols have the compositions of $(NH_4)_2SO_4$ and slightly soluble organics (SSO) and the activation is calculated with the reformulation of Köhler theory to include the effect of slightly soluble organics and soluble HNO_3, produces a better simulation when compared to the observed convective cloud.

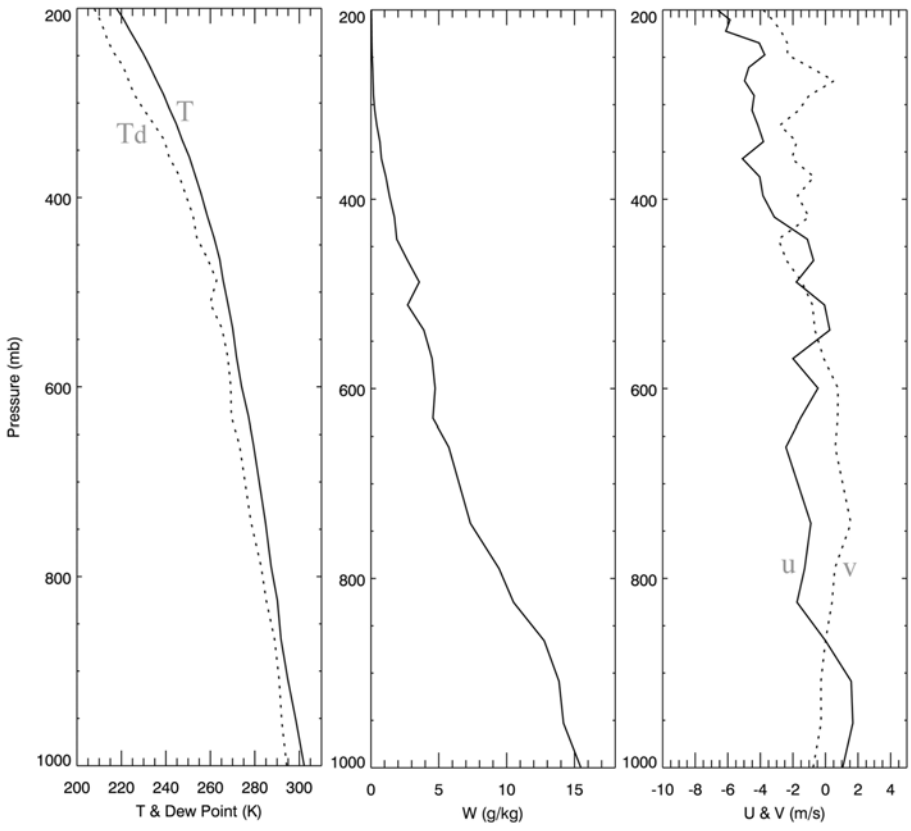

Figure 4.3 Initial profiles of temperature (*T*), dew point (*Td*), water vapor mixing ratio (*w*), and horizontal winds *u* and *v* from a sounding in Houston at 11:58 am local time.

Table 4.1 Results from NS, NSOR and NSORs and comparison with observations

	NS	NSOR	NSORs	Observation
Cell lifetime (min)	160	150	140	120
Cell core size (>30 dBz) (km)	17.0	17.0	14.0	12.0
Accumulated rain (mm)	26.8	25.2	23.3	21.1
Average updraft velocity (m/s)	7.44	7.35	7.21	
Maximum RWC at 155 min (g/m^3)	3.11	2.77	1.65	

Figure 4.4 shows a comparison of radar reflectivity profiles from NSORs at 120 min and 135 min with those from the corresponding observational radar data. The radar reflectivity for a specific hydrometeor is calculated to be proportion to the square of mass concentrations and inverse proportion to number concentrations. The major convective cell is well captured by NSORs. The simulated radar reflectivity generally agrees with the observations, especially for the radar reflectivity of more than 30 dBz. However, the peak radar reflectivity (i.e., the prominent band) at the freezing level in the simulated cloud is likely caused by unrealistic melting processes in the model code. The comparison of the radar reflectivity pattern at the different times (120 and 135 min) indicates that modeled cloud evolution matched the observations. The predicted cloud top is somewhat higher than the observations, probably due to the strong convection caused by the initialization of the warm bubble and coarse resolution used.

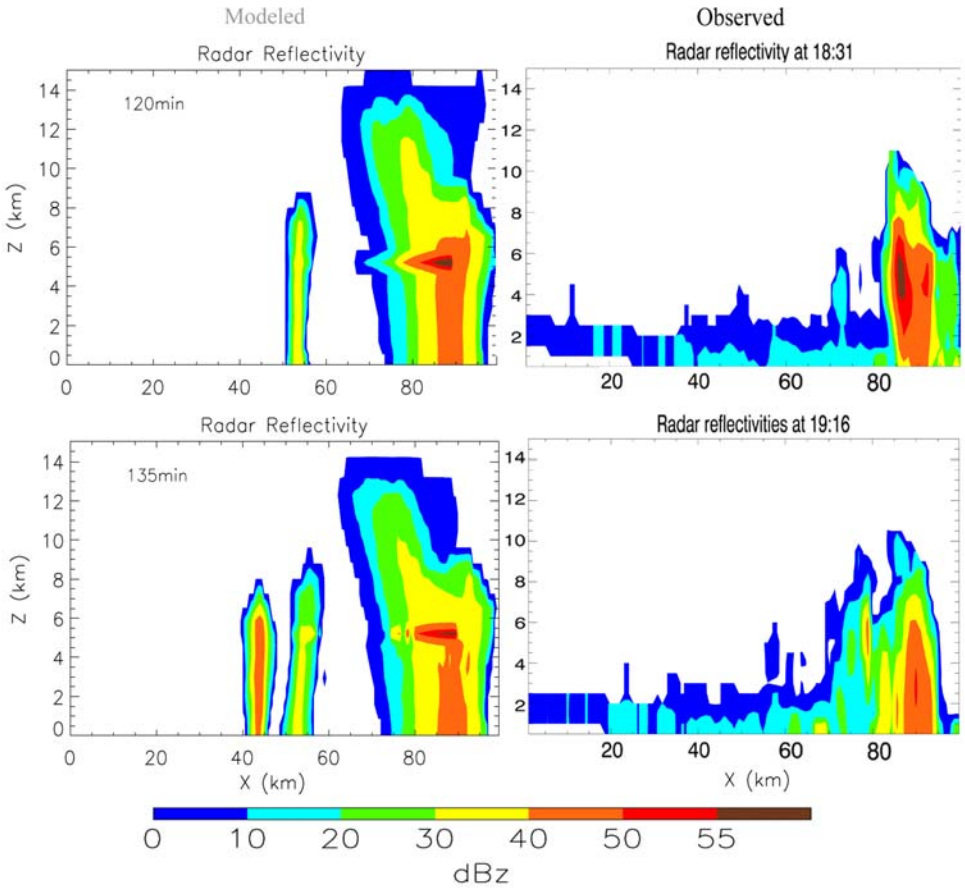

Figure 4.4 Comparison of the radar reflectivity profiles from NSORs with the observations. The left plots correspond to the modeled values, and the right plots correspond to observations.

The cloud microphysical properties and dynamics from three simulations are examined to evaluate the effect of the aerosol chemical properties. Figure 4.5 presents the 2-D profiles of number concentrations of hydrometeors. The cloud droplet number concentrations are considerably different among the three cases. NS predicts more than 1000 cm^{-3} within the cloud core and NSORs predicts only about 600-800 cm^{-3} at 20 min. On the basis of the CCN activation spectra shown in Figure 4.2, NSORs predicts the lowest cloud droplet number concentration and NS predicts the highest one, with a

difference of up to 40%. The predication made by NSOR is between the values of NS and NSORs. The droplet concentrations decrease more rapidly with height in NSORs, indicating more efficient droplet collisions and raindrop formation (coalescence). Most of the ice crystals in the three cases are distributed above the 10-km level, indicating that they are mainly formed by homogeneous freezing. The ice crystal number concentrations at the developing stage (50 min) in NS and NSOR are about 20% higher than those in NSORs within the core, because more droplets are transported into the homogeneous freezing level due to higher cloud droplet concentrations in the former two cases. The higher droplet concentrations also cause more extensive riming, causing higher snow and graupel number concentrations in NS and NSOR. The profiles of cloud water content (CWC) and rainwater content (RWC) at the developing stages are shown in Figure 4.6. The higher values of CWC in NS and NSOR are explained by more condensation, and the higher value of RWC in NSORs than the other two cases is due to more efficient coalescence. Although the differences in CWC and RWC are small among the three cases, the ice processes as shown in Figures 4.5 and 4.7 are more significant. More droplets transported into the freezing level and more extensive riming resultant from the higher droplet number concentrations in NS and NSOR cause the noticeably higher mass concentrations of ice crystal and snow than those in NSORs. Although the graupel number concentration in NSORs is obviously lower than those in NS and NSOR, the graupel mass concentration in NSORs is comparable to the other two, indicating more efficient growth by collisions because of larger droplet size (to be shown later). The differences in the number and mass concentrations of hydrometeors between

NS and NSOR are less evident because the differences in the number of activated aerosols between them are not very significant, due to the effect of surface tension of organics in NSOR. The organization of modeled clouds among the three sensitivity tests is not impacted because the same vertical shear of horizontal wind is applied.

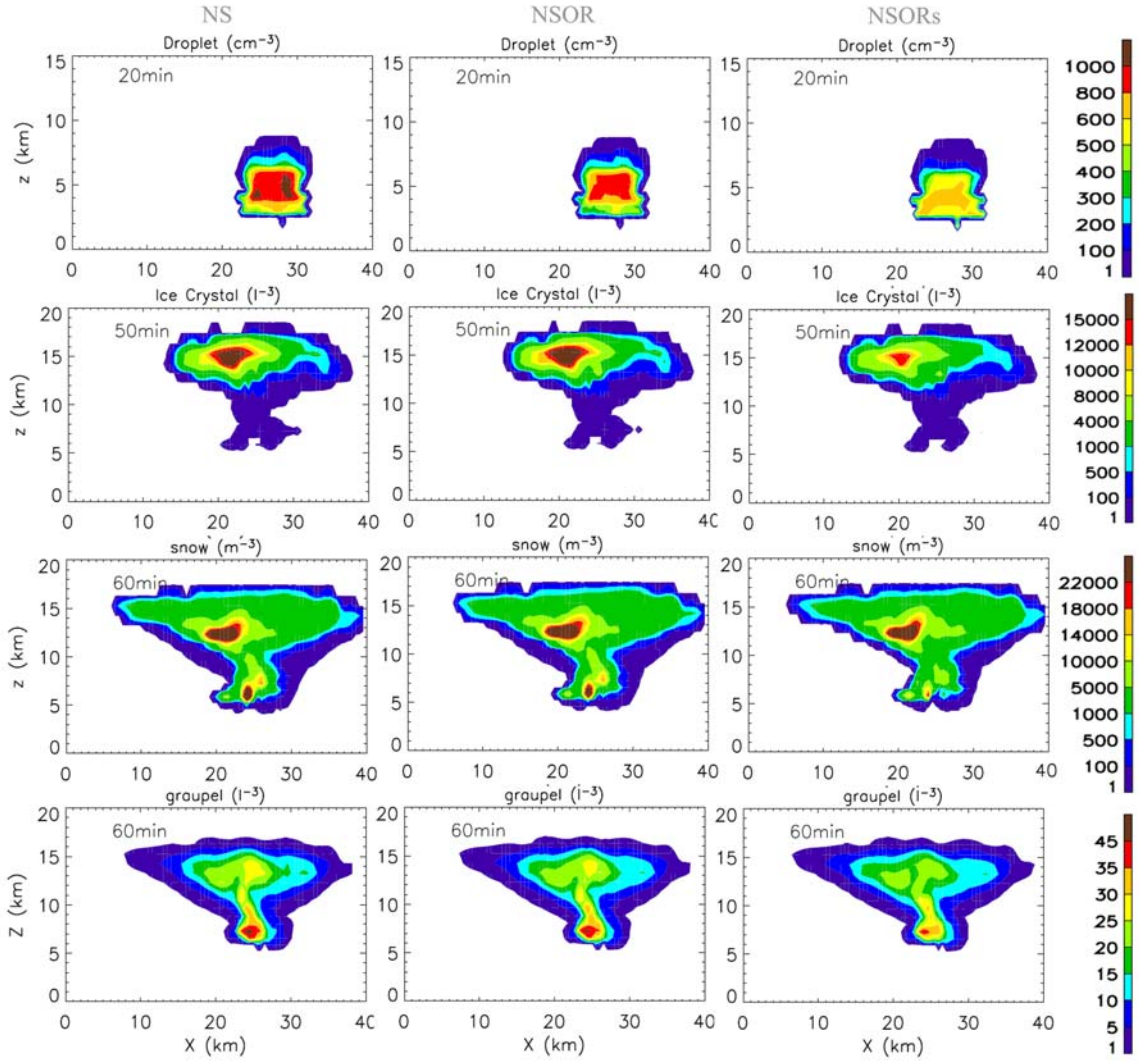

Figure 4.5 2-D profiles of number concentrations of cloud droplet, ice crystal, snow, and graupel for NS (left), NSOR (middle) and NSORs (right) at the developing stages.

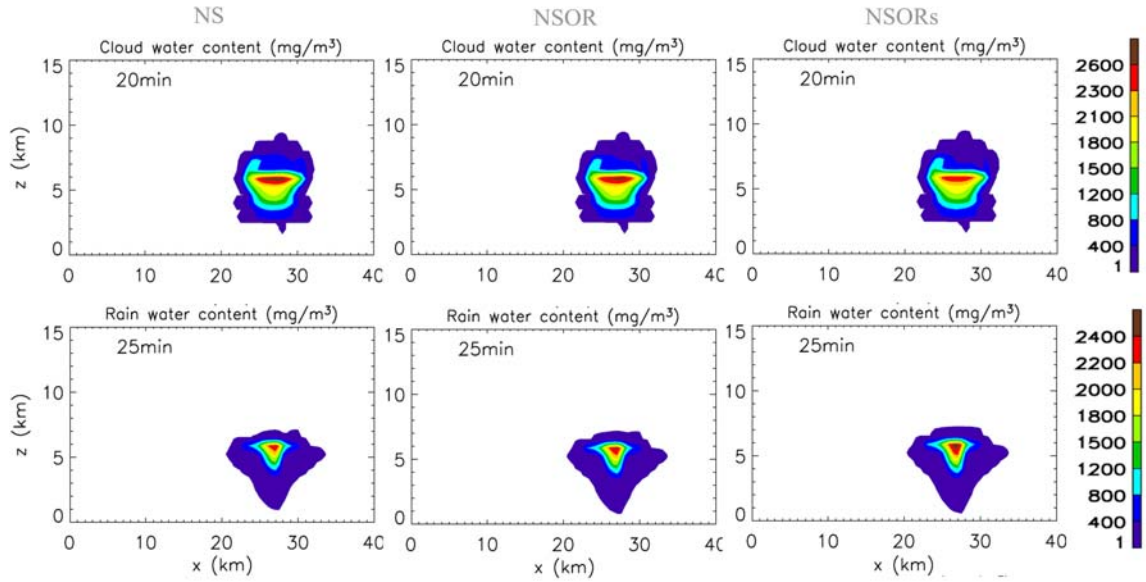

Figure 4.6 As in Figure 4.5, except for CWC and RWC.

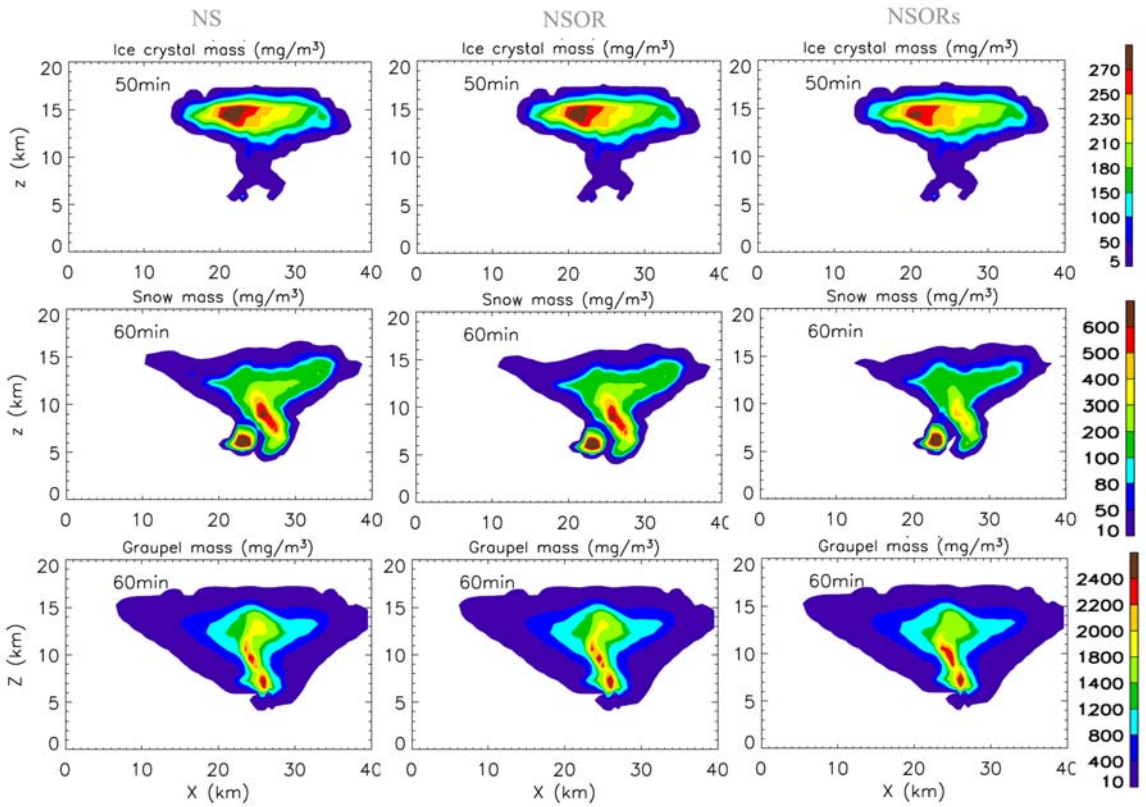

Figure 4.7 As in Figure 4.6, except for ice crystal, snow and graupel.

The 2-D profiles of the mass concentrations of hydrometeors at the mature stage (110 min) are illustrated in Figure 4.8. Cloud water is omitted in the figure because it is negligible at the mature stage. From the ground up to about 2 km, the rainwater content in NS is higher than those in the other two cases, indicating more precipitation from the melting processes. For the ice crystal mass concentration, the domain size with values of more than 120 mg/m^3 in NS and NSOR is larger than that in NSORs, while the difference is smaller than that at the developing stage. The snow mass concentrations decrease noticeably in the order from NS, NSOR, to NSORs, which results from the decrease of ice-ice collisions caused by the decrease of droplet number concentrations. The more efficient growth by drop-ice collisions due to larger droplet size (to be shown later) and by deposition due to higher S_{ice} contributes to the higher graupel mass concentrations in NSORs at the mature stage than those in the other two cases. The lower graupel mass concentration in NSOR than in NS is primarily caused by less riming due to lower droplet concentrations.

A comparison of the cloud droplet effective radius predicted by the three cases is presented in Figure 4.9. Figure 4.9a shows the vertical distributions of the droplet effective radii from NS, NSOR and NSORs at 20 min. At the cloud core and top, NSORs predicts significantly larger droplet effective radii than NS and NSOR. The cloud droplet size increases in the order from NS, NSOR to NSORs. The mean droplet effective radii at different time steps from the three cases are shown in Figure 4.9b. NSORs predicts up to 15-20% larger droplet sizes than NS, and NS predicts the smallest droplet size, consistent with Figure 4.9a. The larger cloud droplet size in NSORs causes more

efficient coalescence and more efficient growth of graupel by collisions, which explain the higher RWC and higher graupel mass concentration stated above, respectively.

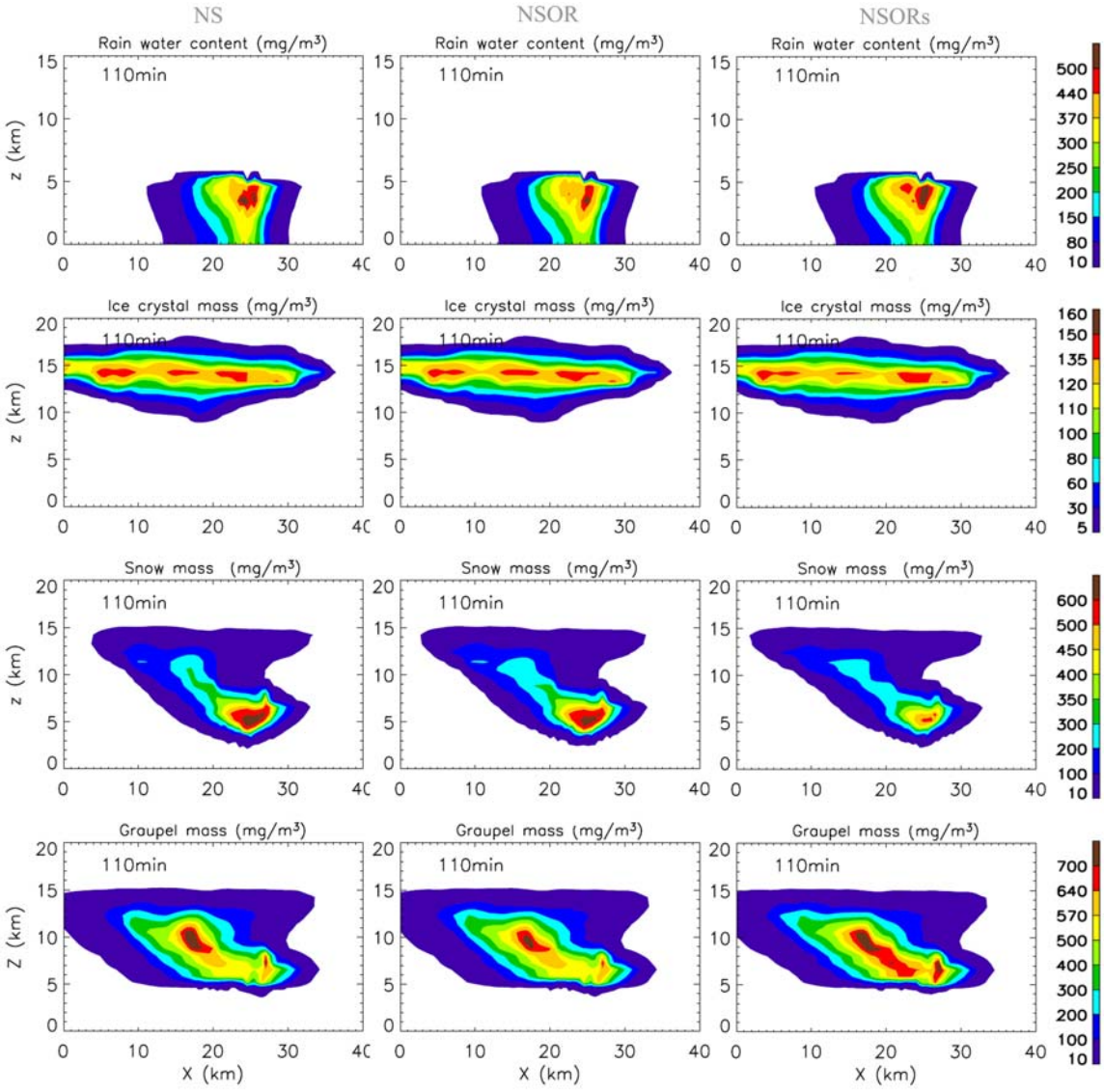

Figure 4.8 As in Figure 4.7, except for rain water, ice crystal, snow and graupel at the mature stages.

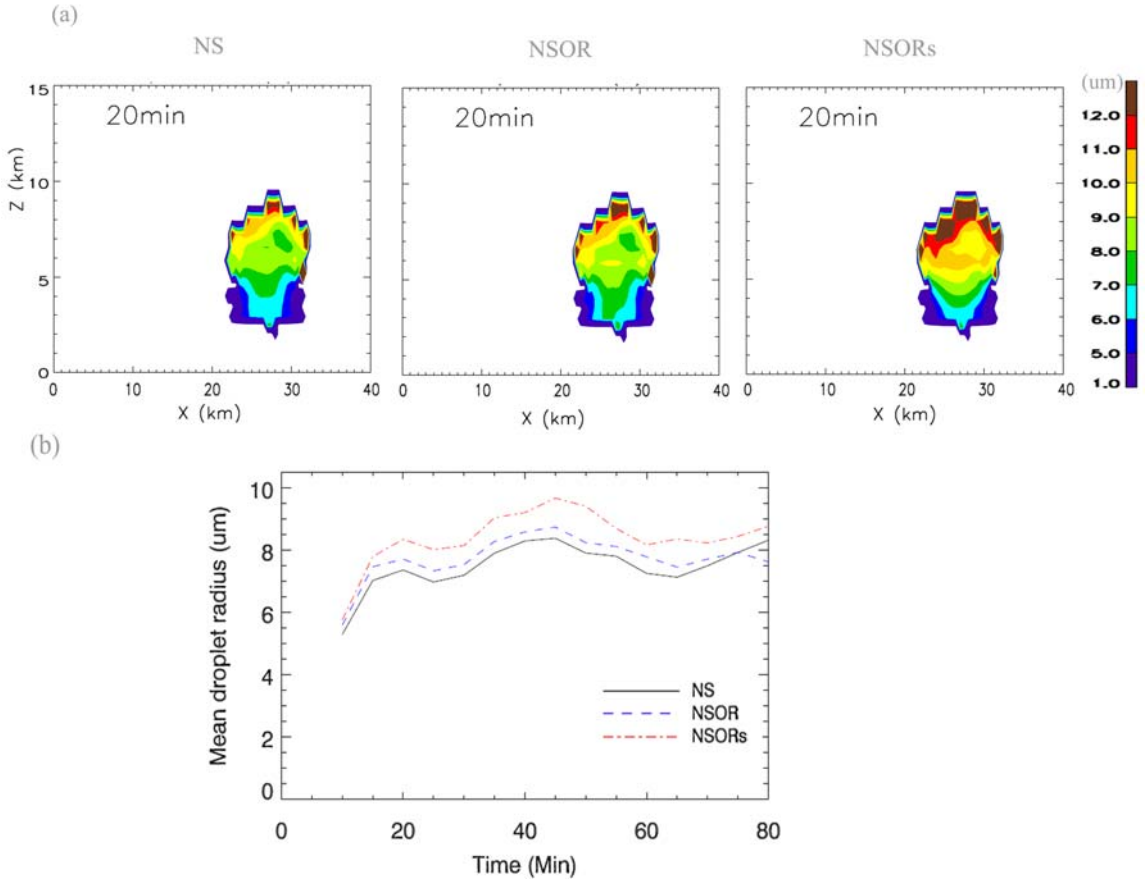

Figure 4.9 (a) 2-D profiles of the cloud droplet effective radius for NS (left), NSOR (middle) and NSORs (right) at 20 min on the same domain as in Figure 4.5, (b) Temporal evolution of the domain-mean of the cloud droplet effective radius in NS (black), NSOR (blue) and NSORs (red).

The simulated temporal evolution of the radar reflectivity is presented in Figure 4.10. At 60 min, the radar reflectivity predicted by NS and NSOR is higher than that by NSORs in the cloud center from about 5 to 10 km, due to higher mass concentrations of ice crystal and snow, as indicated in Figure 4.7. At the mature stage (120 min), the stronger radar reflectivity (over 45 dBz) from the ground to 5 km in NS and NSOR than that in NSORs is explained by more melting precipitation. The stronger ice processes

also explains the larger cell core sizes (17 km) in the former two cases than that in NSORs (14 km), as shown in Table 4.1. At the later stage (175 min) of the cloud, the cloud dissipates more slowly in NS than that in NSOR and the cloud dissipates fastest in NSORs (compared to the radar reflectivity over 30 dBz). As shown in Table 4.1, NS corresponds to the longest cell lifetime (160 min) and NSORs corresponds to the shortest cell lifetime (140 min). Moreover, NS predicts a deeper and stronger secondary convective cell than NSORs. The profiles of the vertical velocity at 155 min presented in Figure 4.11 also illustrates that the updraft velocities for the secondary convective cell in NS are about two times higher than those in NSORs and the prediction by NSOR is between the values predicted by NS and NSORs. There are no significant changes in the vertical velocity at 40 min among the three cases because the strong trigger in dynamics dominates over the effect of microphysical processes caused by activated aerosols. The wavy pattern in the vertical velocity at t = 40 min likely results from two aspects: (a) gravity waves at the early stage as the simulation is spinning up, (b) a strong triggered convection from the warm bubble, and (c) induced by deep convection. The downward motion just below the intense updraft is primarily due to the precipitation-induced downdraft (falling of large particles). The intense updraft causes strong ice processes. Similar phenomena were reported in simulations by *Tao et al.* [2003b].

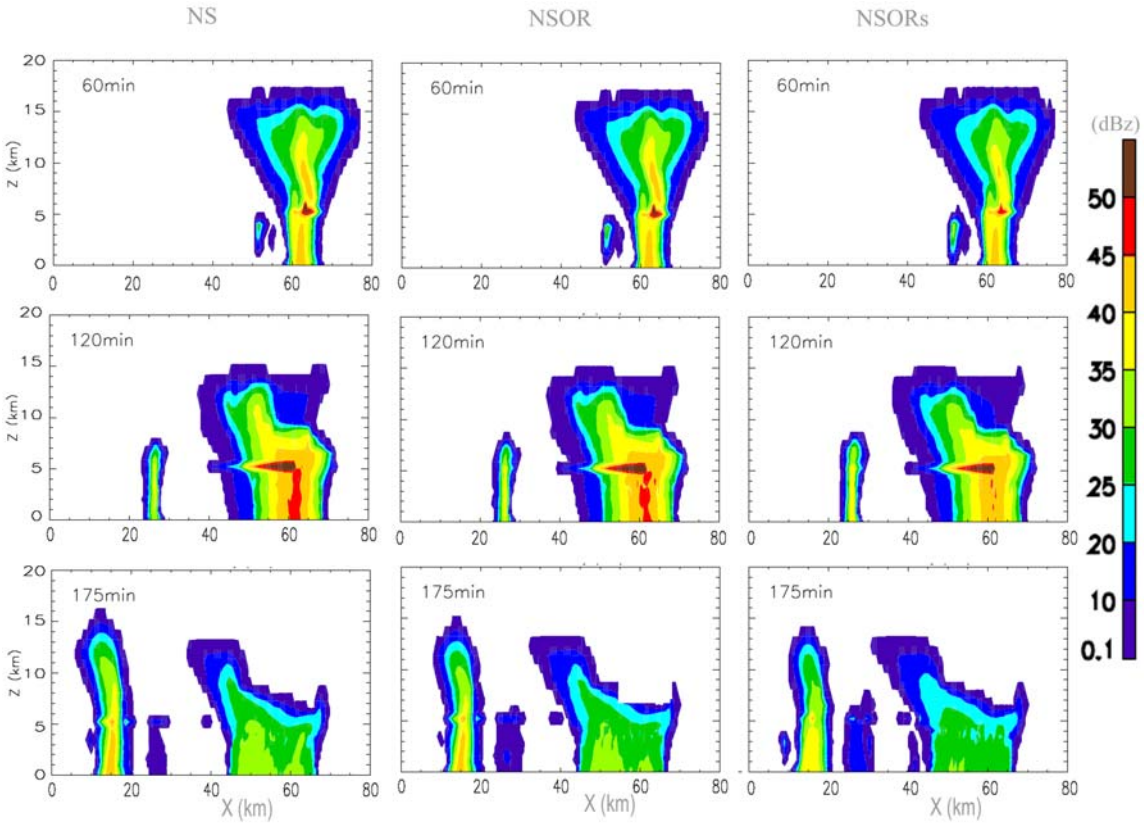

Figure 4.10 2-D profiles of the radar reflectivity for NS (left), NSOR (middle) and NSORs (right) at the developing, mature, and dissipating stages.

The responses of precipitation to the changes of aerosol chemical properties are shown in Figure 4.12. Figure 4.12a presents the time-dependent rain rate averaged over the horizontal domain in Figure 4.11. There exist several noticeable rain rate maximums during the simulations. Peaks 1 and 2 correspond to the maximum warm rain rate and the melting precipitation rate for the major (initial) convective cell, respectively. Peaks 3 and 4 represent the maximum warm rain rate and melting precipitation rate for the secondary convective cell, respectively. The precipitation rates in NS and NSOR are significantly higher (by up to 20%) than those in NSORs at the times of 95-110 min

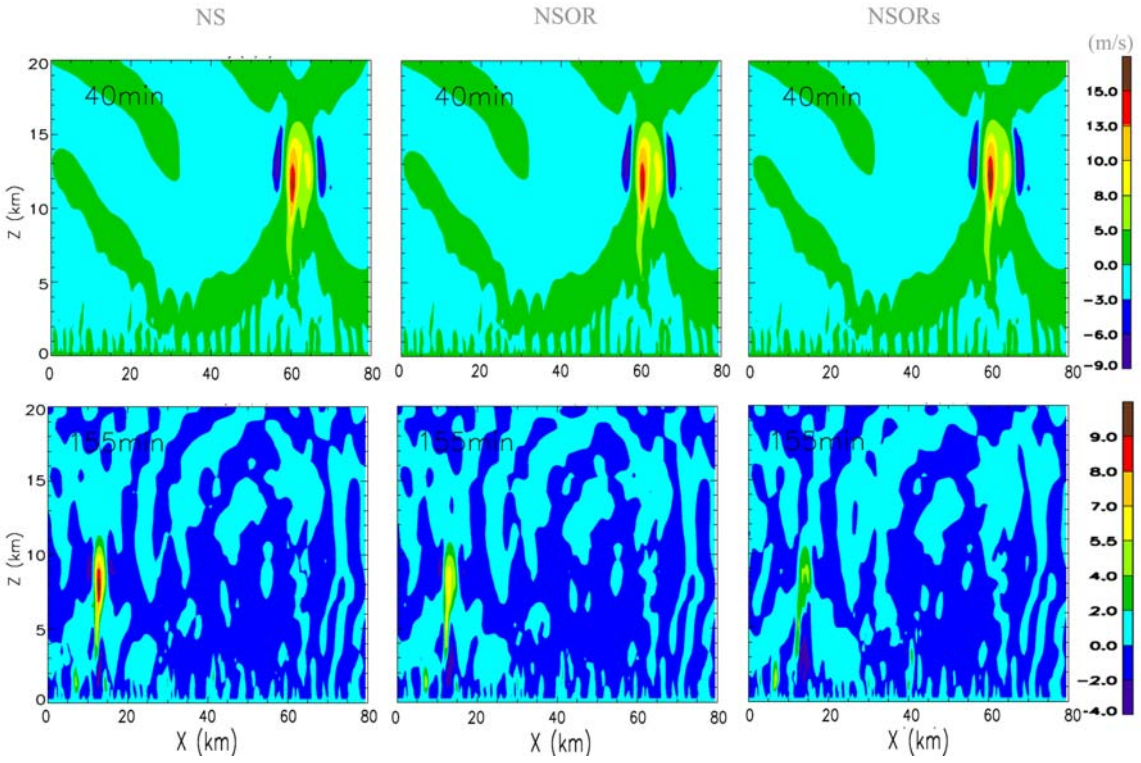

Figure 4.11 2-D profiles of the vertical velocity for NS (left), NSOR (middle) and NSORs (right) at 40 min and 155 min.

(Peak 2) and 145-165 min (Peak 4), but there is little difference among the three cases for peaks 1 and 3, implying that the ice microphysical processes are more sensitive to the changes of aerosol chemical properties than warm rain processes. This is also reflected by the mass concentrations shown in Figures 4.6 and 4.7. More activated aerosols cause stronger ice processes, resulting in more melting precipitation. The maximum rain water content at 155 min for the three cases shown in Table 4.1 also indicates that NS and NSOR predict more melting precipitation than NSORs, with the values of 3.11, 2.77 and 1.65 g/m^3, respectively. Figure 4.12b shows the time dependence of rain accumulation averaged over the domain similar to in Figure 4.12a for the three cases. At the time after

70 min, the accumulated rain in NS is higher than that in NSOR and NSOR predicts a higher accumulated rain than NSORs, especially for the time after 100 min, which is attributed to the melting precipitation. The precipitation is less sensitive to aerosol composition than the cloud microphysical properties.

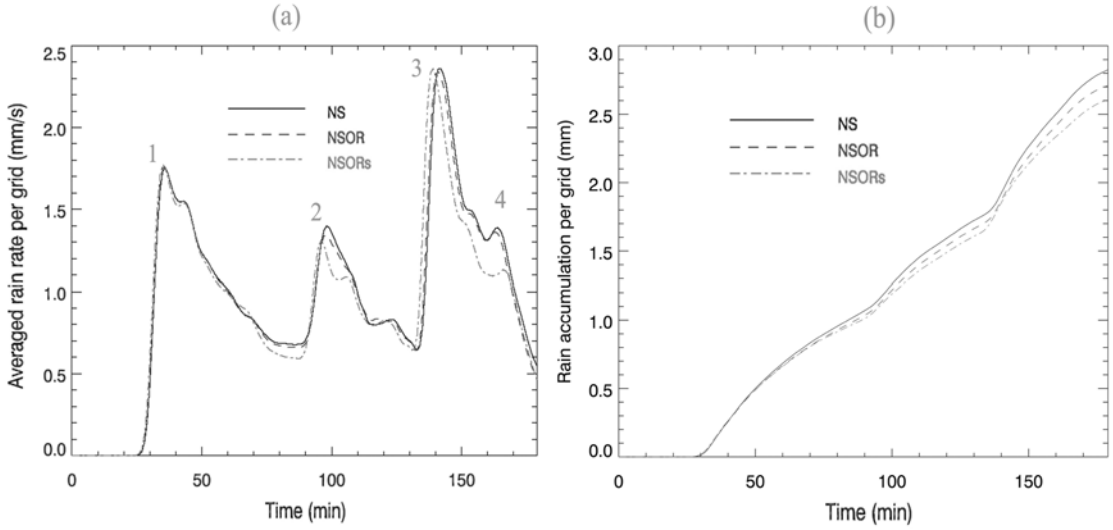

Figure 4.12 Temporal evolution of (a) the rainrate per grid averaged over the domain in Figure 4.11, and (b) the accumulated rain averaged over the same domain as (a).

4.2 Effects of Different Aerosol Types and Initial Concentrations

4.2.1 Description of numerical experiments

In the above study (Section 4.1), it is found that the chemical compositions of $(NH_4)_2SO_4$ and slightly soluble organics and an activation scheme of a reformulation of Köhler theory to include the effect of slightly soluble organics and soluble gas of HNO_3 produce simulations better in agreement with the observations [*Fan et al*., 2007a]. In this section, additional sensitivity studies are conducted to investigate the effects of different

aerosol types and initial concentrations on cumulus clouds, with the above-mentioned aerosol composition and activation scheme as the base run for comparison [*Fan et al*., 2007b].

We consider three cases to represent possible aerosol scenarios in the coastal city of Houston, Texas, dependent on the wind speed and directions [*Fan et al*., 2005; *Li et al*., 2005; *Fan et al*., 2006]. The regional scale environment in this region includes frequent incursions of marine and continental air masses that receive emissions from woodlands and a major urban area containing large power plants and the largest concentrations of petrochemical refining activities in the world [*Lei et al*., 2004; *Zhang et al*., 2004b]. For example, a strong sea breeze in this region brings in large amounts of marine aerosols from the Gulf of Mexico. In contrast, a strong northwest wind brings relatively clean continental air masses. We conduct three simulations to represent polluted continental (P-case), clean continental (C-case), and marine (M-case) aerosol types, on the basis of aerosol measurements and simulations in the Houston area [*Fan et al.*, 2005; *Fan et al.*, 2006]. The initial dynamic and thermodynamic conditions remain invariant for all three simulations in order to isolate the aerosol effects from the other factors. The P-case corresponds to the base run mentioned above, while the C-case has the same configuration as the P-case, except that the aerosol concentration is 10% of the P-case. The M-case has the marine aerosol composition of NaCl and the size distribution is taken from *Khain et al.* [2005]; the total aerosol concentration is about 400 cm^{-3}, less than that in the C-case, which is about 3000 cm^{-3}. Figure 4.13 presents the initial aerosol size distributions for the three aerosol cases. The M-case has large aerosol particles, but

lacks small particles. The number concentrations of activated aerosols at 1% supersaturation for the P-, C-, and M-cases are 4415, 552, and 228 cm^{-3}, respectively. Additional simulations relevant to the continental conditions are also conducted by varying the aerosol concentration from 550 to 2×10^5 cm^{-3} with 15 different initial values, to explore the responses of convective clouds to changes in aerosol number concentrations. Measurements reveal a large variation in the aerosol concentration over the Houston area, with the highest concentration approaching 10^5 cm^{-3} [*Fan et al.*, 2006]. The model configurations similar to the P-case (base run) are employed for all 15 simulations and the aerosol sizes do not change with the total aerosol concentration.

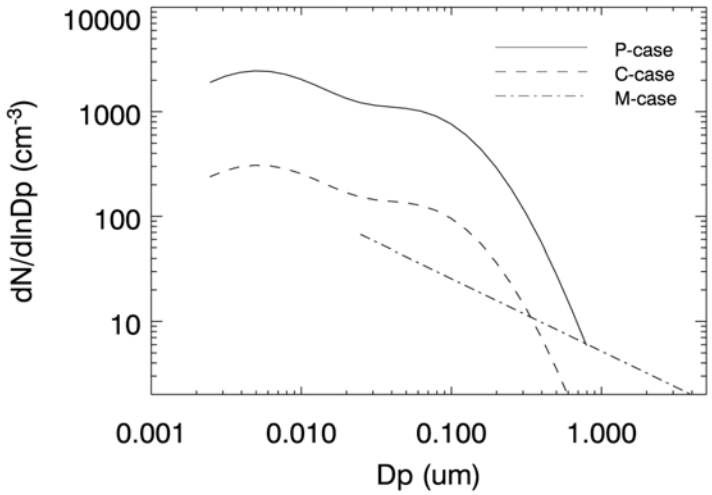

Figure 4.13 Initial size distributions for polluted, clean continental, and marine aerosol cases.

To survey the responses of modeled deep convective clouds to the changes in aerosol and RH conditions, we perform statistical analyses of the mean model variables.

The cloud area mean (area-mean) and the population mean (p-mean) of a variable are calculated similarly to *Wang* [2005]. The area-mean corresponds to the averaged value over a specific region at an output time step, while the p-mean represents the averaged value over all qualified grids and during the entire simulation period.

4.2.2 Results

4.2.2.1 Polluted continental, clean continental, and marine aerosol cases

The 2-D fields of the number concentrations of hydrometeors are presented in Figure 4.14. Figures 4.15 and 4.16 illustrate the mass concentrations of hydrometeors for the P-, C-, and M-cases at the developing stages. The most noticeable difference in Figure 4.15 is that the P-case predicts significantly higher number concentrations of cloud droplets, ice crystals and snow than the C- and M-cases. Also, the cloud anvil (the coverage of ice phase) at 50 min is the largest for the P-case, likely because of more droplet condensation at a higher droplet number concentration and hence a stronger convection [*Khain et al*., 2005]. The maximum updraft velocity during the developing stage is 16.4 m/s in the P-case, and only 10.4 in the C- case and 8.0 m/s in M- cases. Alternatively, the large anvil can also be explained by the smaller cloud droplets in the P-case that ascend to the higher levels, in contrast to larger raindrops formed in the C- and M- cases that settle down. The p-mean of droplet effective radius in the P-case is 8.3 μm, much smaller than those in the C- and M- cases (13.6 and 14.5 μm, respectively). The more droplet condensation is responsible for the higher cloud water content (CWC) in the P-case (Figure 4.15). The higher droplet concentrations in the P-case extends up to the 7-km level, indicating a less efficient coalescence compared with the C- and M-cases,

in which the droplet concentrations decreases more rapidly with height because of more efficient droplet collisions and raindrop formation (Figure 4.14). The higher rainwater content (RWC) for the C- and M-cases in Figure 4.15 reflects more efficient raindrop formation; for both cases, the supersaturation is higher, leading to faster condensation growth and more efficient coalescence of cloud droplets. The cloud droplet concentration, CWC, and cloud coverage shown in those cases are consistent with previous observations [*Rosenfeld and Woodley*, 2001; *Kaufman and Koren*, 2006] and model simulations [*Khain and Pokrovsky*, 2004]. Ice crystals in the P- and C-cases are primarily distributed above the 10-km level, indicating that they are mainly formed by homogeneous freezing. However, in the M-case much less droplets reach the freezing level because of a much weaker convective strength, lack of small aerosol particles, and efficient growth into raindrops. The much higher supersaturation with respect to ice (S_{ice}) in the M-case causes more efficient ice growth by deposition, contributing to the higher mass concentrations of snow (Figure 4.16). The P-case predicts higher graupel number and mass concentrations than the M-case (Figures 4.14 and 4.16), because of more extensive riming at higher droplet number concentrations. The graupel concentrations in the C-case are comparable to that in the P-case, attributable to more efficient drop-ice collision in the C-case.

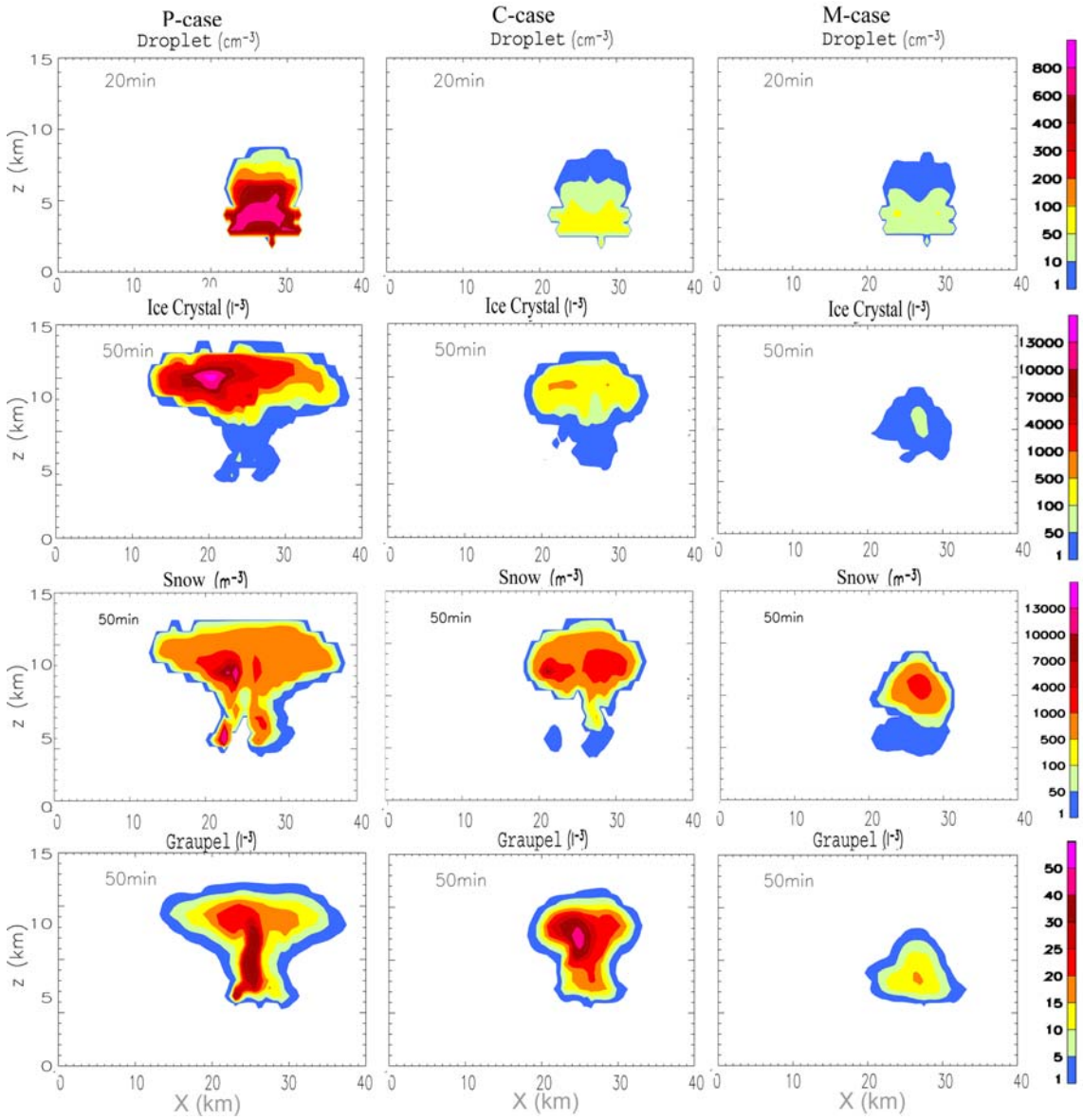

Figure 4.14 2-D fields of number concentrations of cloud droplet, ice crystal, snow, and graupel for the P- (left), C- (middle) and M-cases (right) at the developing stages.

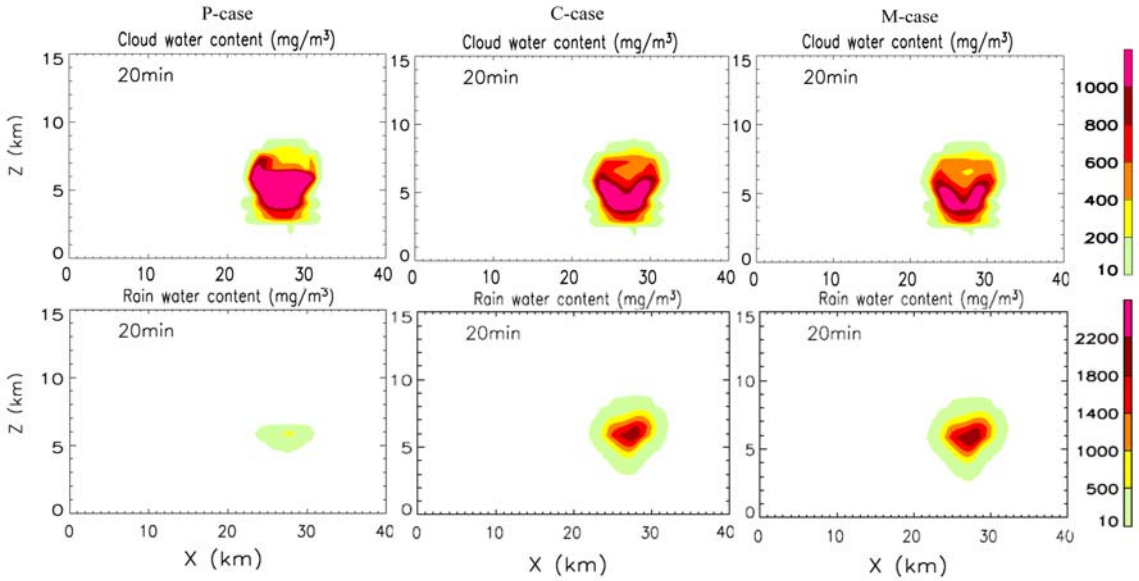

Figure 4.15 As in Figure 4.14, except for CWC and RWC at 20 min.

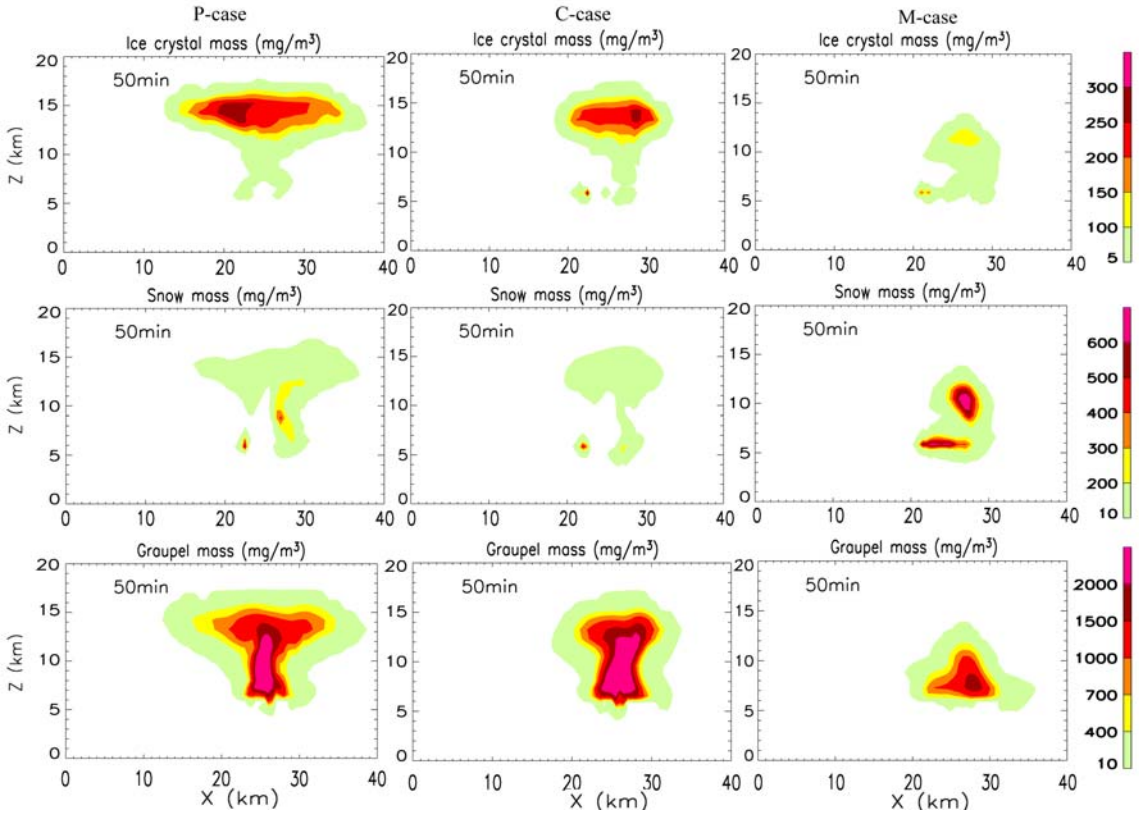

Figure 4.16 As in Figure 4.15, except for ice crystal, snow and graupel at 50 min.

The radar reflectivity at the developing (~50 min) and mature (~120 min) stages is depicted in Figure 4.17 for the three cases. The more efficient production of rain water, snow and graupel at 50 min is responsible for the more intensive radar reflectivity in the C and M-cases. At the mature stage, M-case predicts stronger radar reflectivity than the P- and C- cases.

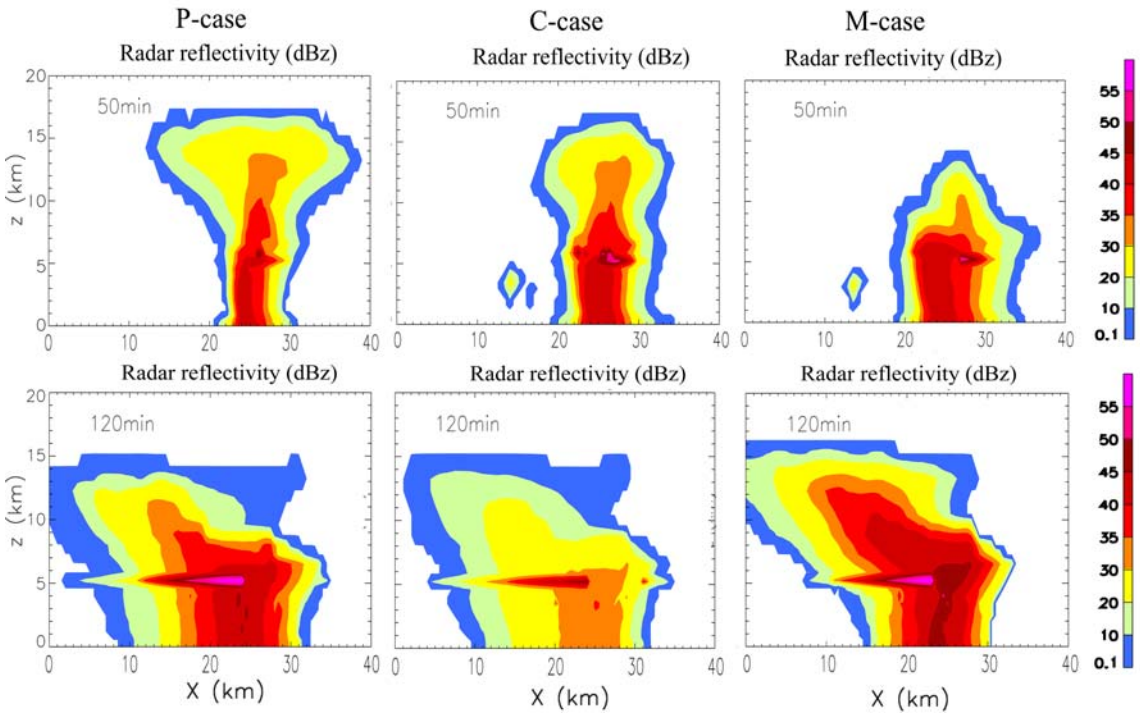

Figure 4.17 The total radar reflectivity of P- (left), C- (middle) and M-cases (right) in the developing stage at 50 min and mature stage at 120 min.

Figure 4.18a shows the temporal evolution of the maximum updraft velocity for the three cases. In the developing stage from 15 min to about 50 min, the P-case predicts up to 45% higher maximum updraft velocity than the C-case, while the C-case predicts

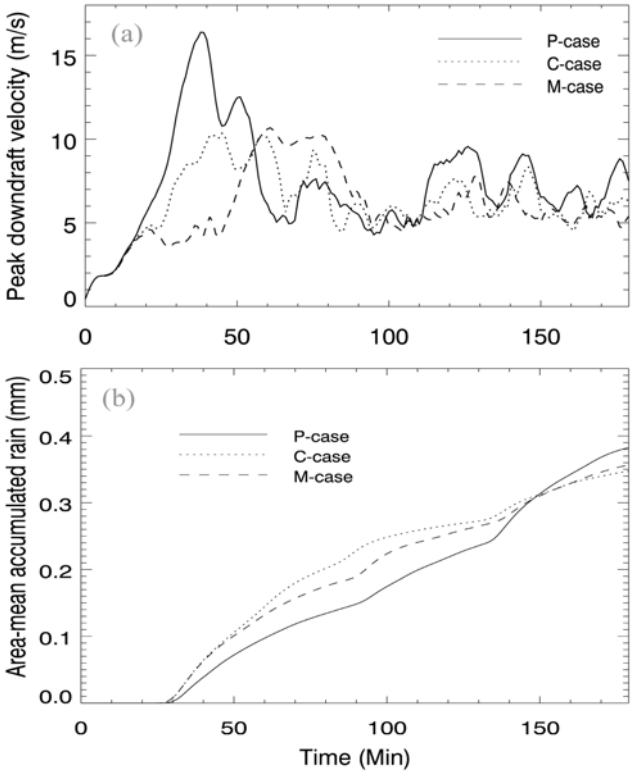

Figure 4.18 (a) Time dependence of the maximum updraft velocity and (b) the area-mean accumulated rain for the P-, C- and M-cases.

up to 60% higher than the M-case. The largest updraft velocity for the P-case is attributed to the highest droplet condensation due to the highest droplet number concentration. During the intermediate stage from about 50 min to 90 min, the maximum updraft velocity is the highest in the M-case, with the maximum difference of over 40%. The maximum convective strength occurs at about 40, 45 and 60 min in the P-, C-, M-cases, respectively. The convection develops faster in the P-case due to much more latent heat release from droplet condensation. The cloud in the M-case develops slower and the updraft velocity reaches its maximum about 20 min later relative to the P-case (Figure 4.18a). The downdraft resulted from the fallout of warm rain at the early stage in

the M-case can work as an increase in the buoyancy at the later stage, possibly contributes to the strong convection during 60-90 min.

In Figure 4.17, the M-case predicts the most intensive radar reflectivity among the three cases at 120 min because of the strongest convection from 60 to 90 min (Figure 4.18a). The calculated radar reflectivity for a specific hydrometeor increases with the mass concentration and decreases with the number concentration. Figure 4.19 illustrates the mass concentrations of hydrometeors at 120 min. The mass concentrations of ice crystal and snow in the M-case are higher due to higher S_{ice}. The formation of ice crystals at the levels over 15 km in the P- and C- cases is primarily through homogeneous freezing. In the P-case, more droplets are transported to these levels with stronger convection and higher droplet number concentrations, leading to higher ice crystal concentrations than those in the C-case (Figures 4.14 and 4.16). For the low concentration of supercooled droplet (M-case), the ice crystal formation is determined from the parameterization formula by Meyers et al. [1992], where the ice nuclei concentration is proportional to S_{ice}. The high S_{ice} in the M-case leads to high ice crystal formation according to the parameterization and also efficient diffusion growth of ice crystals, yielding the high mass concentrations of ice crystals (Figure 4.19). The p-mean S_{ice} from 90-120 min is 0.047, 0.062, and 0.101% for the P-, C-, and M-cases, respectively. The production mechanisms of snow and graupel correspond to ice-ice and drop-ice collisions, respectively. Efficient ice-ice collisions in the M-case due to larger sizes of ice particles resultant from the higher supersaturation lead to the much higher snow concentration. The much lower graupel mass concentration in the M-case than the

other two cases at 120 min (Figure 4.19) is mainly because of the less graupel production at a much lower supercooled droplet concentration.

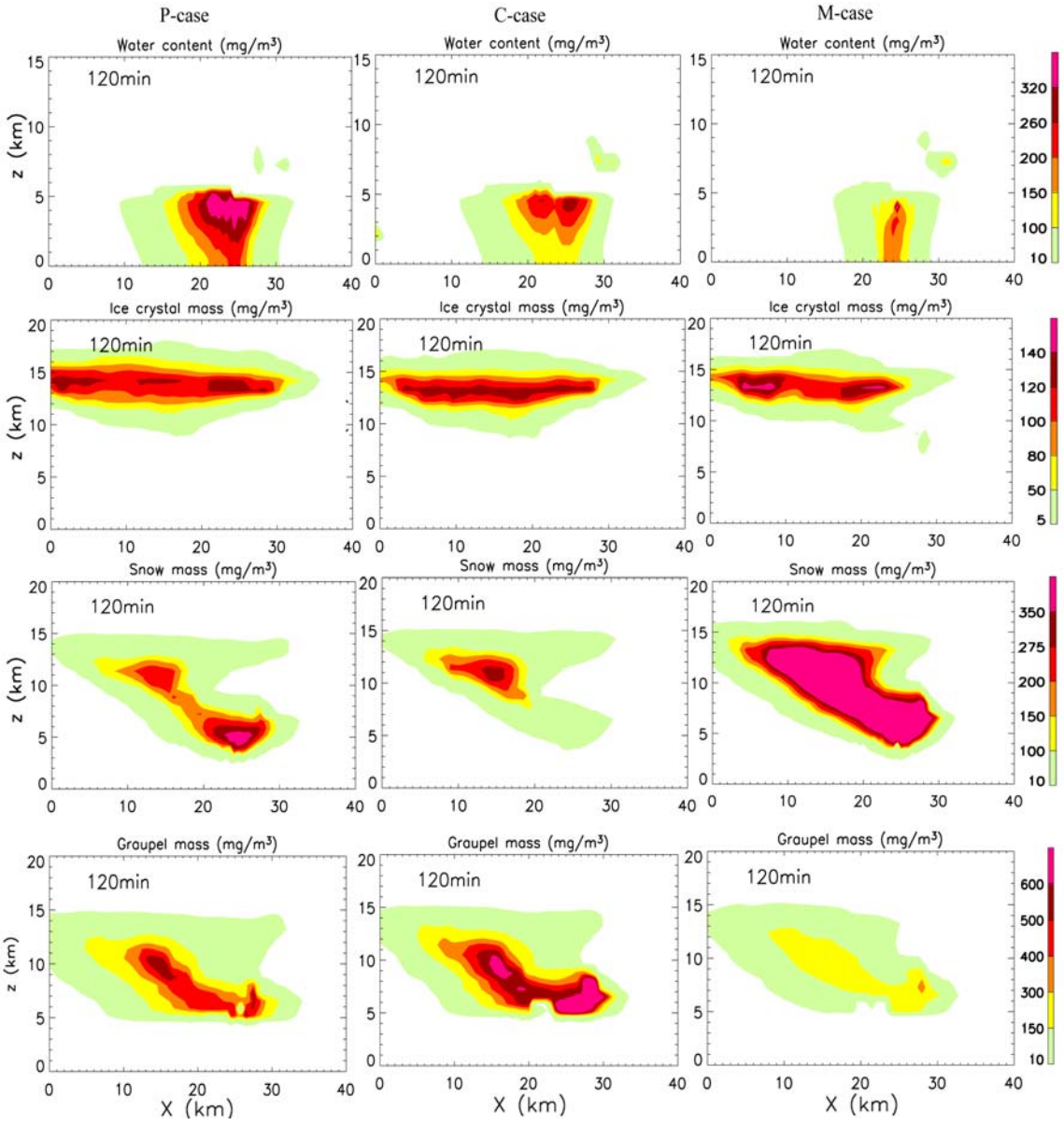

Figure 4.19 As in Figure 4.16, except for liquid water, ice crystal and snow in the mature stage at 120 min.

A comparison of cloud macro-physical properties is shown in Table 4.2. The P-case predicts almost two times larger cell size and about 60 min longer cell lifetime than the C-case. The cell lifetime and size are defined from the radar reflectivity that is greater than 30 dBz. Also, the accumulated rain over the entire domain is higher in the P-case than that in the C-case. As shown in Figure 4.18b, the time-dependence of the area-mean accumulated rain reveals that the secondary clouds contribute to the precipitation significantly in the P-case, but not in the C- and M-cases. The enhanced melting precipitation rate and the stronger secondary convection caused by the higher aerosol concentrations primarily contribute to the increased precipitation in the P-case, although the increase is not very significant. The stronger updraft in the P-case enhances the upward transport of liquid drops and retards sedimentation of ice particles. The former effect is responsible for rapid formation of ice particles and the latter decreases the number of ice particles settling down to the warm region. Moreover, the stronger updraft elevates the glaciation level where large ice particles are formed from higher collision efficiencies for aggregation. Also, more extensive riming of ice particles in the P-case is due to the much higher supercooled droplet number concentration. All those result in more melting precipitation, longer cell lifetime, larger cell size, and stronger secondary clouds in the P-case than in the C-case. The total domain precipitation for the P-case is higher than that for the C-case, suggesting an enhanced precipitation with increasing aerosols. This is in contrast to several previous field and modeling studies showing suppressed precipitation with increasing aerosols in the shallow cumulus clouds [e.g., *Rosenfeld*, 2000; *Feingold et al.*, 2005]. The humid environment and large surface

heating in the Houston region [*Fan et al*., 2007a] likely create favorable thermodynamic and dynamic conditions for a positive aerosol-precipitation relation. Our modeled precipitation enhancement is in agreement with field measurements around heavily polluted coastal urban areas in this region [*Shepherd and Burian*, 2003].

Table 4.2 Comparisons of the results from P-, C- and M-cases.

	P-case	C-case	M-case
Max. radar reflectivity (dBz)	61.1	58.4	62.7
Cell lifetime (min)	140	80	150
Cell size (>30 dBz) (km)	14	7.5	12
Total domain rain (mm)	366.8	356.3	364.1

4.2.2.2 Effects of initial aerosol concentration

The responses of the p-mean number and mass concentrations of hydrometeors to the increase of the initial aerosol concentration in the continental aerosol environment are presented in Figures 4.20 and 4.21, respectively. It is evident from 4.20a that the number concentration of cloud droplet increases with increasing aerosol concentrations. The p-mean number concentration of ice crystal also increases with aerosol (Figure 4.20b), but the change of graupel number concentration is not monotonic (Figure 4.20c). The p-mean CWC and graupel mass concentration increase with the aerosol concentration of less than about 1.5×10^4 cm^{-3} (referred to as 'low-aerosol cases'), as shown in Figure 4.21a and 4.21d, respectively. The mass concentrations of all hydrometeors become much less sensitive to the aerosol concentration above 1.5×10^4

cm^{-3} (referred to as 'high-aerosol cases'). The lower RWC and graupel mass concentrations (Figures 4.21b and 4.21d) in the high-aerosol cases than those in the low-aerosol cases are primarily due to the less efficient collisions of drop-drop and drop-ice (graupel). The p-mean RWC is not very sensitive to aerosol probably because the increase of the melting precipitation compensates with the decrease of warm rain processes with increasing aerosols.

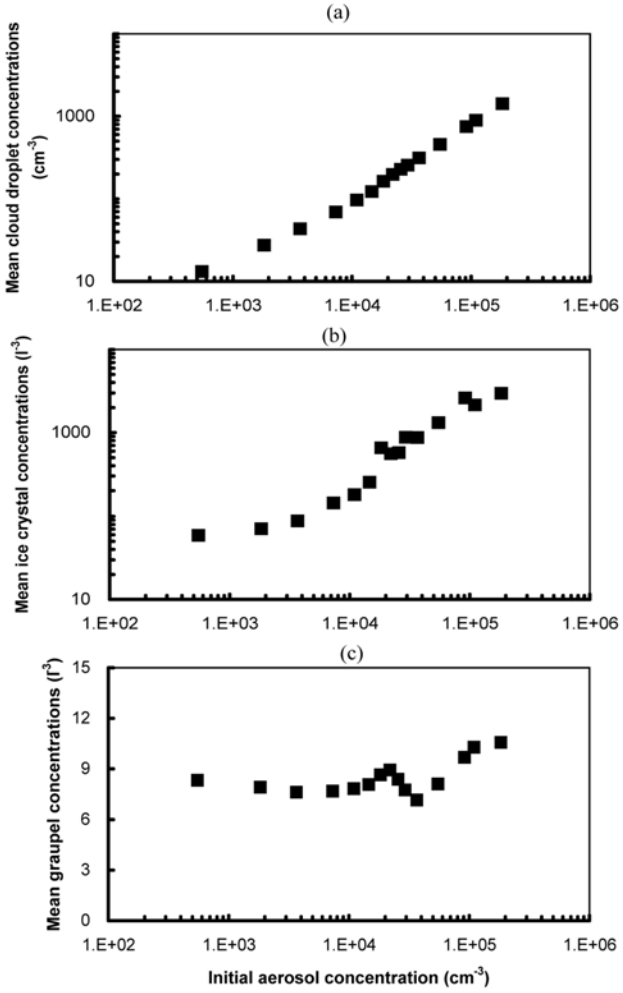

Figure 4.20 P-mean number concentrations of (a) cloud droplet, (b) ice crystal, and (c) graupel with increasing aerosols.

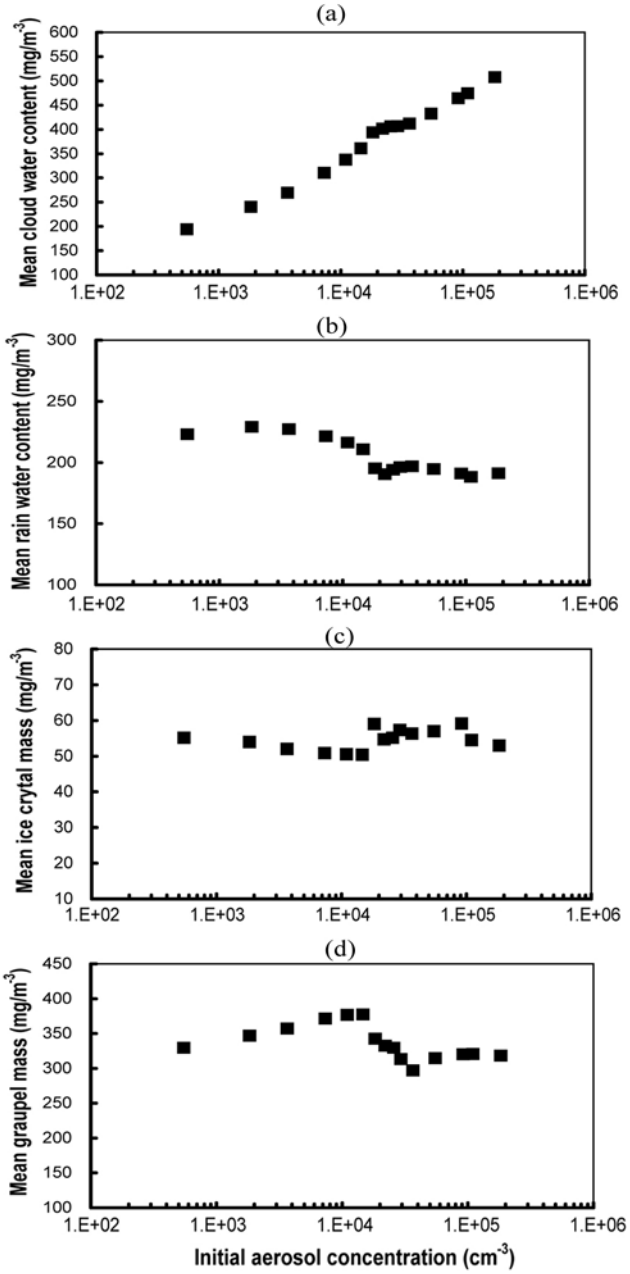

Figure 4.21 P-mean mass concentrations of (a) cloud droplet, (b) rain drop, (c) ice crystal, and (d) graupel with increasing aerosols.

In contrast to the cloud water content and droplet number concentration, the p-mean cloud droplet size decreases with increasing aerosols (4.22a). From the aerosols of

550 to 2×10^5 cm^{-3}, the p-mean effective radius of cloud droplets is reduced by 70%. In the high-aerosol cases, the reduction in the droplet effective radius with increasing aerosol becomes less significant. The latent heat release associated with the condensation of cloud droplets enhances the updraft velocities in the cloud (Figure 4.22b), although the convection is less sensitive to aerosols in the high-aerosol cases. As shown in Figure 4.22c, the secondary clouds are stronger with increasing aerosols except for the extremely high aerosol cases (over about 5×10^4 cm^{-3}), in which the convection is suppressed because of the very low supersaturation resulting from droplet condensation.

The response of precipitation to increasing aerosols is not monotonic (Figure 4.23a). The total precipitation in the entire domain increases with aerosols except for the extremely high aerosol cases. The enhanced total precipitation with increasing aerosols is primarily due to enhanced melting rain rates and stronger secondary clouds. The total precipitation significantly decreases with increasing aerosols in the extremely high aerosol cases, likely because of suppressed convection from depletion of water vapor and inefficient coalescence for small droplet sizes. There is a slight rain delay with increasing aerosol (Figure 4.23b). In our simulations with increasing aerosols, the aerosol sizes remain invariant, and hence the sizes of activated aerosols are invariant. A strong warm bubble initialization for all the cases probably reduces the delay of initial rain.

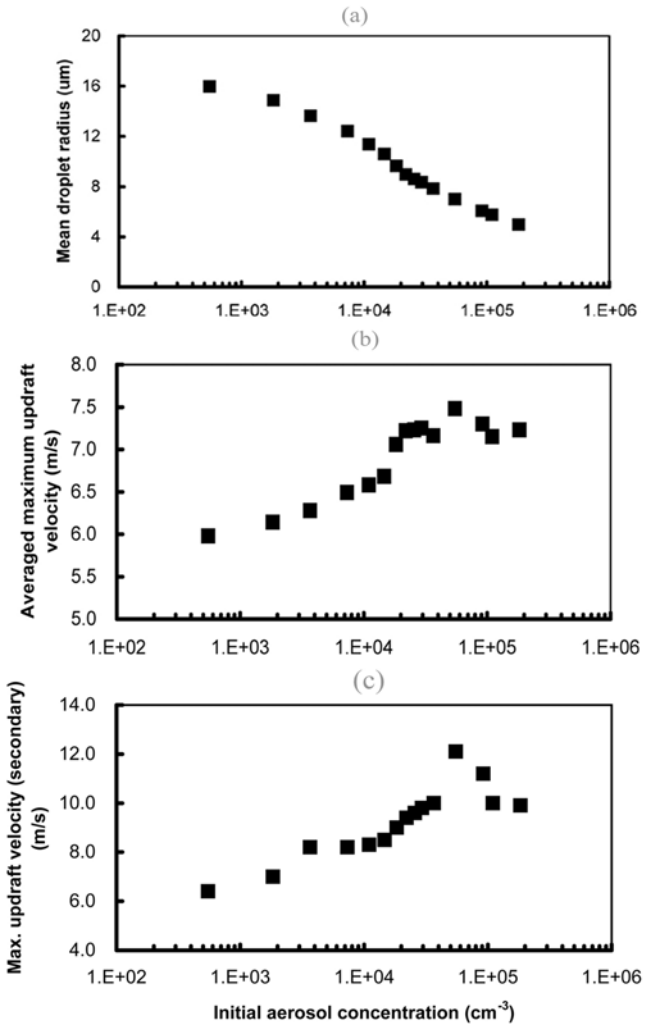

Figure 4.22 As in Figure 4.21, except for (a) P-mean effective droplet radius, (b) averaged maximum updraft velocity over the simulation time, and (c) the maximum updraft velocity of the secondary clouds.

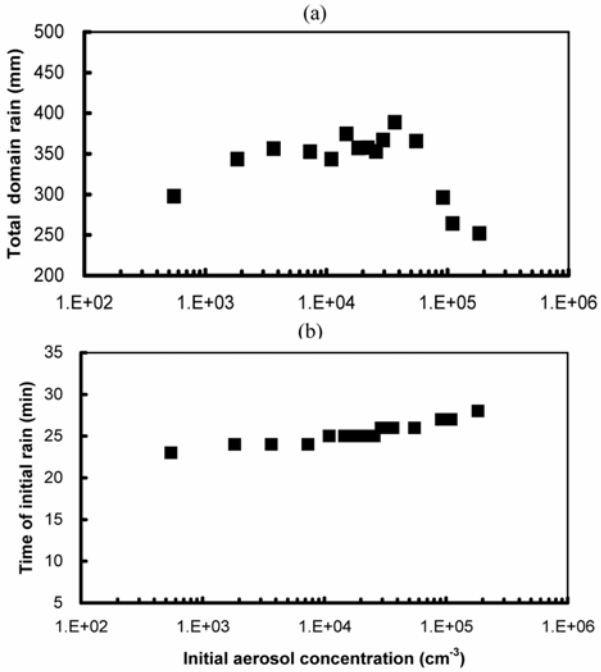

Figure 4.23 (a) Total domain precipitation, and (b) time of initial rain formation with increasing aerosols. The total domain precipitation is the sum of accumulated rain of every grid.

The present results that cloud number concentrations, cloud water, cloud coverage, and precipitation increase while the cloud droplet size decreases with aerosol concentration, are consistent with the study of deep convection conducted by *Wang* [2005]. However, in our study the increases in cloud properties are found to reach a maximum value at a certain aerosol concentration. The cloud properties then become insensitive or decrease with further increasing aerosol concentrations. The range of the aerosol concentration employed in *Wang* [2005] corresponds to the concentration at the low-aerosol cases used in our study. In addition, the increase in ice crystal number concentration is much more sensitive to aerosol concentration in this study than that in *Wang* [2005], likely caused by the different ice microphysics employed.

4.3 Effects of Relative Humidity (RH)

The impact of relative humidity (RH) on cumulus cloud development is evaluated for the three aerosol cases, i.e., P-, C-, and M-cases [*Fan et al.*, 2007b]. In each case, four RH conditions of 40, 50, 60 and 70% at the surface are considered, with 40 and 70% RH representing dry and humid conditions, respectively. This RH range is representative of the surface moist conditions in the Houston region during the early afternoon hours. The RH in the vertical levels varies with the surface RH accordingly (with a same factor). For example, the RH is about 99% at 1.5 km for the 70% surface RH condition.

The cloud development is dramatically affected by RH, because of a significant change in the CAPE. The CAPE increases dramatically with increasing RH, with the values of 0.0, 19.0, 960.0 and 2840.0 J kg^{-1} at the 40, 50, 60 and 70% surface RH conditions, respectively. The fields of mass concentrations of hydrometeors for the P-case at 50, 60 and 70% RH are shown in Figure 4.24. At 40% RH only limited shallow warm cumulus develops. The mass concentrations of hydrometeors dramatically increase with increasing RH, as is the case for the number concentrations of hydrometeors (not shown). The cloud base height decreases significantly with increasing RH, as reflected from the profile of cloud water content. Ice phase processes are limited at lower RH (40 and 50% surface RH), but are greatly enhanced at higher RH (60 and 70% surface RH). At 70% RH, the maximum updraft is 42.5 m/s, corresponding to extremely strong convection because of very large CAPE. The clouds at 70% RH appears to be too strong, likely attributable to the coarse vertical resolution of the model

upper layers. In addition, cloud development is about 15 min earlier at 70% RH than that at 50% RH. The level of the ice phase is significantly elevated and the cloud anvil is greatly expanded when RH increases from 50 to 70% RH as shown in Figure 4.24, due to the significant increase of CAPE.

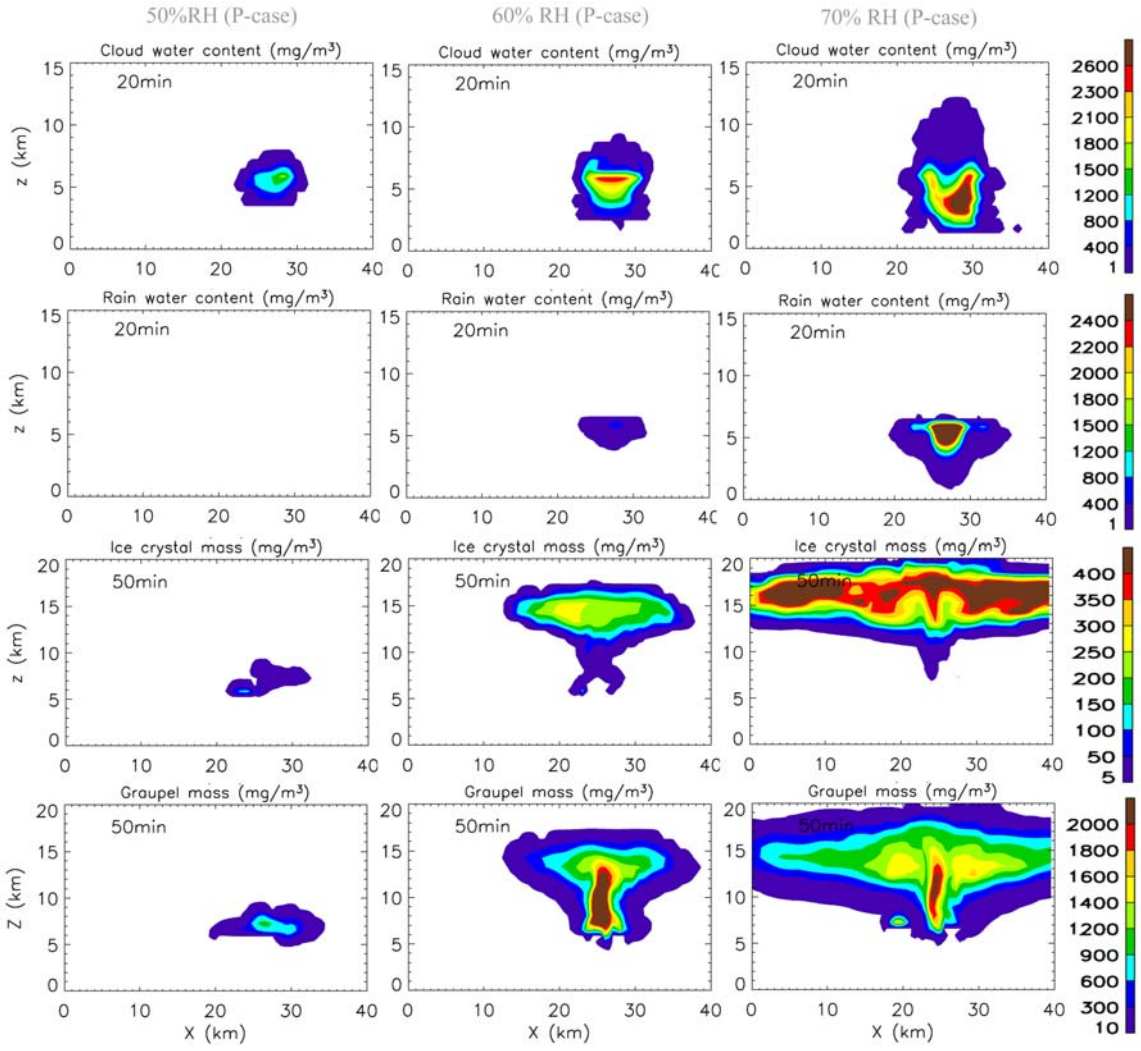

Figure 4.24 2-D fields of CWC, RWC and mass concentrations of ice crystal and graupel for the P-case at 50 (left), 60 (middle) and 70% (right) RH.

The aerosol effect on the cloud microphysical properties is strongly dependent on RH: the effect is negligible in relatively dry air and becomes much pronounced in humid air. The p-mean mass concentrations of hydrometeors for the P-, C- and M-cases at different RH conditions are depicted in Figure 4.25. Generally, the hydrometeor mass concentrations increase with RH and the aerosol effect on CWC is evident (Figure 4.25a). The p-mean RWC increases with RH as shown in Figure 4.25b, but it is higher in the C-case than that in the P-case, primarily because of the more efficient coalescence relating to larger droplet sizes. As shown in Figure 4.25c, for all three aerosol cases, the ice crystal mass concentration increases dramatically when RH increases from 50 to 70%, but there is little difference between 40 and 50% RH. The aerosol effect on ice crystal mass is significant only in humid air. The p-mean graupel mass increases with RH and the aerosol effect on graupel is more evident at the higher RH (Figure 4.25d). The much lower mean graupel mass in the M-case is caused by the much lower droplet number concentration due to the very low aerosol particles. The small differences in cloud properties between 40 and 50% RH are explained by little difference in CAPE.

As shown in Figure 4.26a, when RH increases from 40 to 60% the p-mean effective droplet radius is not sensitive to RH, but very sensitive to aerosol. However, the droplet size is significantly larger at 70% RH than that at 60% RH. The P-case consistently predicts much smaller droplet size than C- and M-cases at all RH conditions. The droplet size is determined jointly by the number of nucleated droplets and supersaturation, which have opposite effects on the effective radius. The cloud dynamics changes most noticeably with RH and also with aerosols to a lesser extent. The

maximum updraft velocity increases with RH due to increasing CAPE (Figure 4.26b). The aerosol effect on the convective strength is only significant in relatively humid air, i.e., at 60 and 70% surface RH.

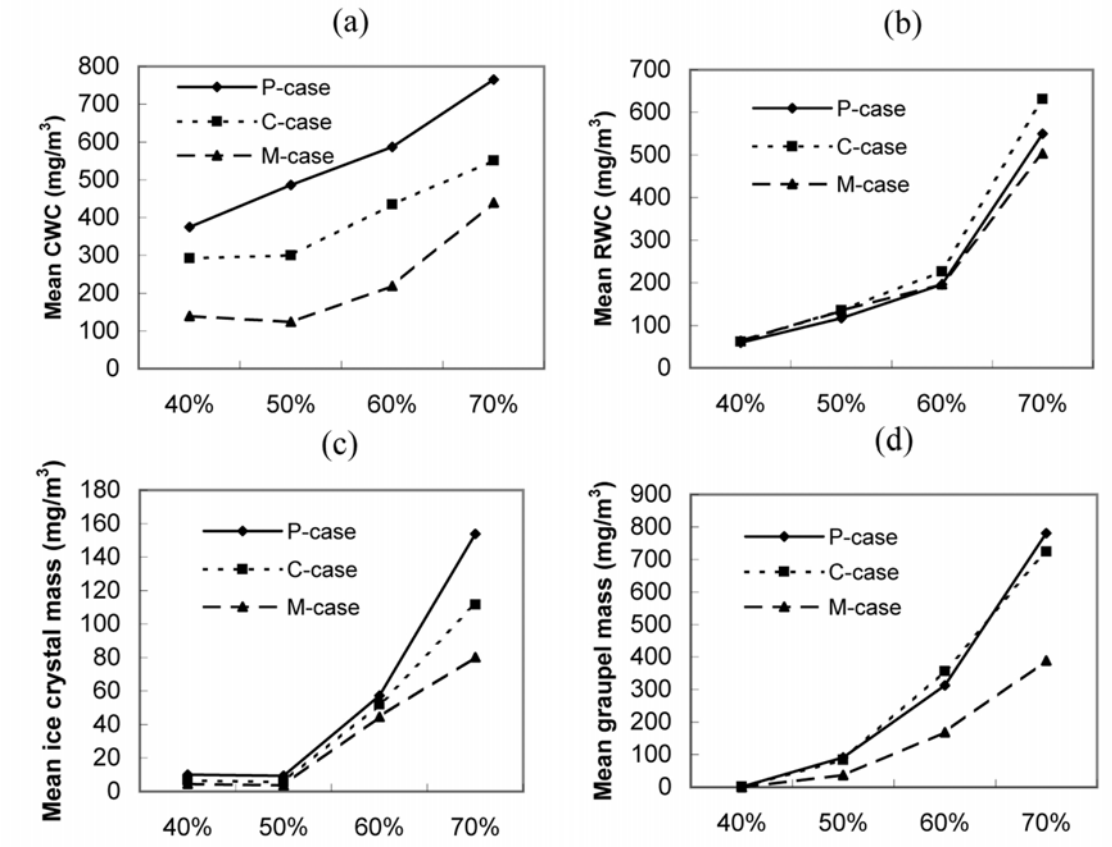

Figure 4.25 P-mean mass concentrations of (a) cloud droplet, (b) rain drop, (c) ice crystal, and (d) graupel for the P-, C- and M-cases at the different RH conditions.

The response of precipitation to RH for the three aerosol cases is shown in Figure 4.27. The aerosol effect on the maximum rain rate is most significant under the moist conditions, and the M-case predicts significantly lower maximum rain rate in the humid

air (70% RH) (Figure 4.27a). The larger maximum rain rate in the P-case relative to the M-case is consistent with the results reported by *Lynn et al*. [2005b]. The rain delay for a certain aerosol case is very sensitive to RH, but at a certain RH it is not very sensitive to aerosols under the same initial thermodynamic conditions (Figure 4.27b). *Khain et al.* [2005] found a significant delay in the onset of precipitation in the continental cloud compared with the maritime cloud. In our simulations the same sounding and warm bubble initialization determine an initial strong convective development and hence a less delay in precipitation.

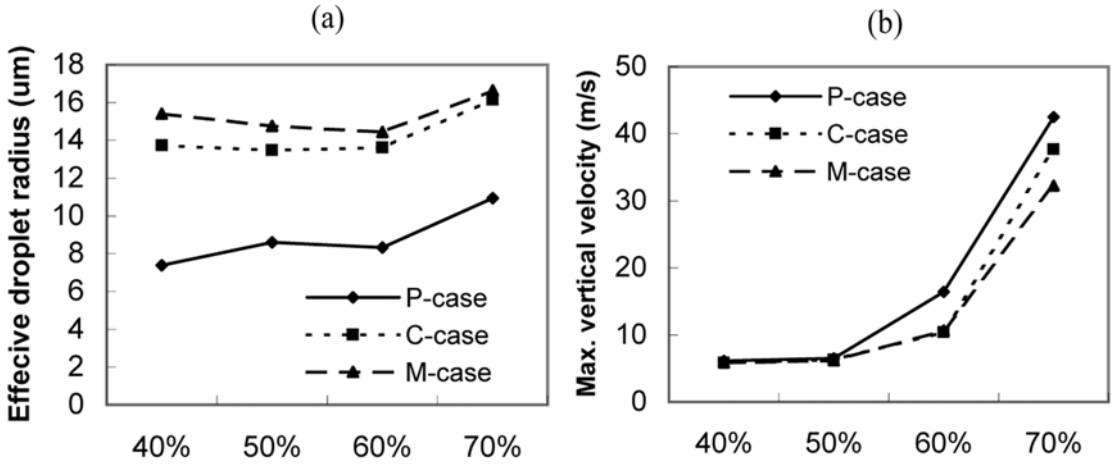

Figure 4.26 As in Figure 4.25, except for (a) P-mean effective droplet radii, and (b) Maximum updraft velocity.

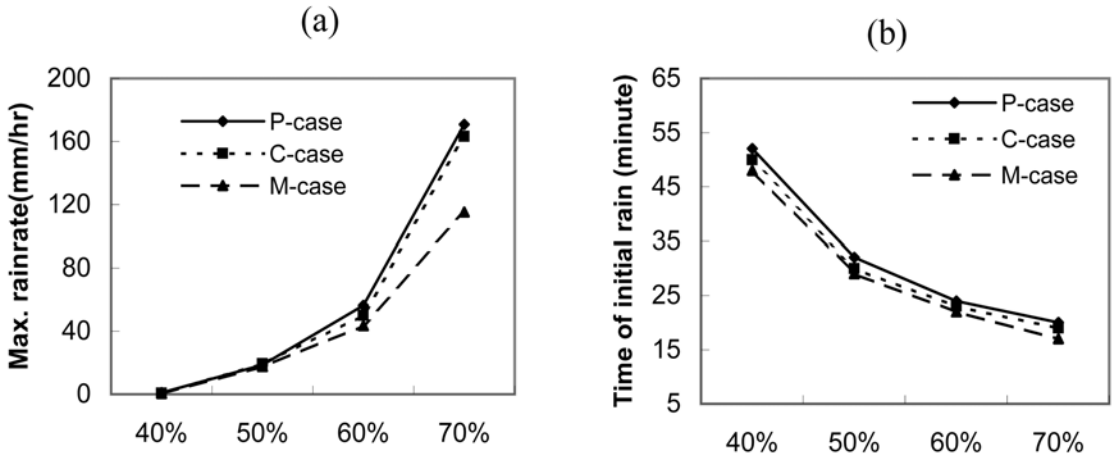

Figure 4.27 As in Figure 4.25, except for (a) Maximum rain rate, and (b) time of initial rain formation.

4.4 Summary

The aerosol indirect effects on the cumulus clouds have been investigated. The cloud microphysical and macrophysical properties change considerably with the aerosol chemical properties. With varying the aerosol composition from only $(NH_4)_2SO_4$, $(NH_4)_2SO_4$ with soluble organics, to $(NH_4)_2SO_4$ with slightly soluble organics, the number of activated aerosols in cloud decreases gradually, leading to a decrease in the cloud droplet number concentration and an increase in the droplet size. Increasing activated aerosols results in the increase of ice crystal formation by homogeneous freezing, more extensive riming, lower supersatuation (S_w and S_{ice}), less efficient growth of graupel, and more melting precipitation. Ice microphysical processes are more sensitive to the changes of aerosol chemical properties than the warm cloud processes. The changes in macrophysical properties are more evident: the increase of activated aerosols resulted in longer cell lifetime, larger cell size, stronger secondary convective

cell and more accumulated precipitation.

The cloud properties are considerably influenced by the aerosol type and concentration. The maritime aerosol results in more intensive radar reflectivity in both developing and mature stages than the continental aerosol in polluted air. For the continental case, the increase of initial aerosol concentration generally leads to a stronger convection. The most noticeable effect of increasing aerosol is the increases of the cloud droplet number concentration and cloud water content, but a decrease in the effective radius of cloud droplets. These changes lead to more extensive collection of small droplets by large drops and ice riming of supercooled droplets. The increase of the convection promotes the upward transport of the liquid drops, which leads to a faster formation of ice particles and retards ice particle sedimentation. We show that the total amount of precipitation and rain rate increase with aerosols over this region, confirming measurements of precipitation enhancement reported previously [*Shepherd and Burian*, 2003]. More melting precipitation and stronger secondary clouds contribute to the enhanced precipitation with increasing aerosols. Previous measurements and simulations have suggested suppressed precipitation associated with increasing anthropogenic aerosols in shallow cumulus clouds [e.g., *Rosenfeld*, 2000; *Feingold et al*., 2005]. Our simulations suggest that the aerosol effects on clouds and precipitation are dependent on cloud-embedded thermodynamic and dynamic conditions. The weak wind shear, the humid environment and large surface heating in the Houston region [*Fan et al.*, 2007a] likely impact the aerosol-precipitation relation.

The cloud development is dramatically affected by relative humidity. As RH increases from 40 to 70% at the surface, the cloud changes from shallow warm to deep convective types due to the significant increase of CAPE. The aerosol effects on the cloud microphysical properties and precipitation are found to be strongly dependent on RH: the effects are negligible in dry air (40% RH) but significant in humid air (60-70% RH). The aerosol effects on the convective strength and the rain rate are significant in the humid air. The rain delay is found to be sensitive to RH, but not very sensitive to aerosol under the same initial thermodynamic conditions.

Our results reveal that in continental aerosol environments, the impact of aerosols on deep convective clouds is consistent with the Twomey effect, but the effect is non-linear. The aerosol indirect effect on deep convection is more pronounced in relatively clean air than in heavily polluted air, implying that aerosols may play a more important role in moist and clean marine environments [*Zhang et al*., 2007].

5. AEROSOL RADIATIVE EFFECTS ON DEEP CONVECTIVE CLOUDS*

The climate effects of anthropogenic aerosols have been of extensive attention and large uncertainties [*IPCC*, 2001]. The addition of anthropogenic aerosols containing absorbing components to the atmosphere may significantly change the radiative fluxes at the top-of-atmosphere (TOA), at the surface, and within the atmospheric column. Recent reports summarize that on a global average the sum of direct and indirect forcing by anthropogenic aerosols (ACF) at the TOA is likely to be negative and may be comparable in magnitude to the positive forcing of about 2.4 W m^{-2} by anthropogenic greenhouse gases [*IPCC*, 2001]. Large uncertainties exist in current estimates of aerosol forcing because of incomplete knowledge concerning the distribution and the physical and chemical properties of aerosols as well as aerosol-cloud interactions.

It has been demonstrated that the climate effects of aerosols are more significant on the regional scale than on the global scale [*Wang*, 2004]. The effect of anthropogenic aerosols on direct radiative forcing is significant in the vicinity and downwind of the urban area of Houston. The observed aerosol radiation forcing during the afternoon periods was between -30 and -80 W m^{-2} [*Fast et al.*, 2006]. *Fast et al.* [2006] also indicated that the predicted surface shortwave radiation was 30 to 40 W m^{-2} closer to the observations in the vicinity of Houston when the aerosol radiative properties were incorporated into the shortwave radiation scheme.

---

* Submitted for publication in *Journal of Geophysical Research*.

In the previous section, we have investigated the aerosol indirect effect on the cumulus clouds in the Houston area using the GCE model without consideration of radiation and land surface processes [*Fan et al*., 2007a, b]. A more comprehensive investigation of aerosol effects on the deep convective clouds with the focus on radiative effects of anthropogenic aerosol containing black carbon (BC) is performed here by incorporating a improved Goddard radiation scheme and an explicit land surface model (PLACE) into the GCE model [*Wetzel and Boone*, 1995; *Tao et al.*, 2003a]. The descriptions of these models are given in Section 2. An aerosol radiative module is developed as described in Section 2 and coupled with the radiation scheme to on-line calculate the aerosol radiative properties as a function of wavelength based on aerosol composition, size distribution, mixing state and ambient relative humidity. The significance of the aerosol radiative effects (ARE) is investigated by comparing with the case excluding the ARE. The associated aerosol direct, semi-direct and indirect radiative forcing values for deep convective clouds are estimated, and the sensitivity of cloud properties and radiative forcing to aerosol single-scattering albedo (SSA) are examined. Although the effects of aerosols including absorbing components on clouds and radiative forcing have been investigated by model simulations in previous studies [*Johnson et al.*, 2004; *Feingold et al.* 2005; *Jiang and Feingold*, 2006; *McFarquhar and Wang*, 2006], few studies have simultaneously examined the aerosol direct, semi-direct, and indirect effects on clouds using a spectral-bin CRM coupled with a state-of-the-art land surface model and an aerosol radiative module to online calculate the aerosol radiative properties.

5.1 Model Configuration and Validation

5.1.1 Initial conditions and design of numerical experiments

The initial sounding used in the simulations is from Lake Charles (93.21W, 30.11N) near the Houston area, and is at 7:00 am (local time) on August 24, 2000 (Figure 5.1). The vertical temperature and dew point profiles reveal an unstable atmosphere with convective available potential energy (CAPE) of 1800 J kg^{-1}, integrated from the level of 500 m. For an early morning sounding, the surface temperature is low (23.2°C) and the surface relative humidity is high (87%) (Figures 5.1a and 5.1b). The sounding also reveals relatively weak wind shear (Figure 5.1c). The computational domain is comprised of 1024 × 33 grid points with a horizontal resolution of 500 m. There are 33 stretched vertical levels with a resolution of 280 m at the lowest level and 1260 m at the top. Open boundary conditions are used at the lateral boundaries. The time step is 6 s. The radiation and land surface processes are calculated every 3 min.

The initial surface conditions for PLACE are broadly representative of land cover in the Houston area as shown in Table 5.1. In this heavily urbanized region is a mixture of impervious cover, lawns, and deciduous broadleaf trees and bushes. The soils are typical of coastal plains, sandy and silty clays and clay loams. The low percentage of vegetation cover reflects the sprawling urban infrastructure of buildings and transportation networks. Initial soil moisture and soil temperature values are based on examination of the NCEP/NCAR daily reanalysis of soil moisture, soil temperature, and precipitation for the week preceding 24 August. The reanalysis of volumetric soil moisture in the layers 0–10 cm and 10–200 cm for the Houston area has a range of

0.20–0.28 cm^3 cm^{-3}. The initial soil moisture values in Table 5.1 assume additional drying in the layers above 10 cm after rainfall on 22 August. Both soil temperature and soil moisture are randomly varied within the ranges in Table 5.1 across the model domain to account for the variability of the urban landscape.

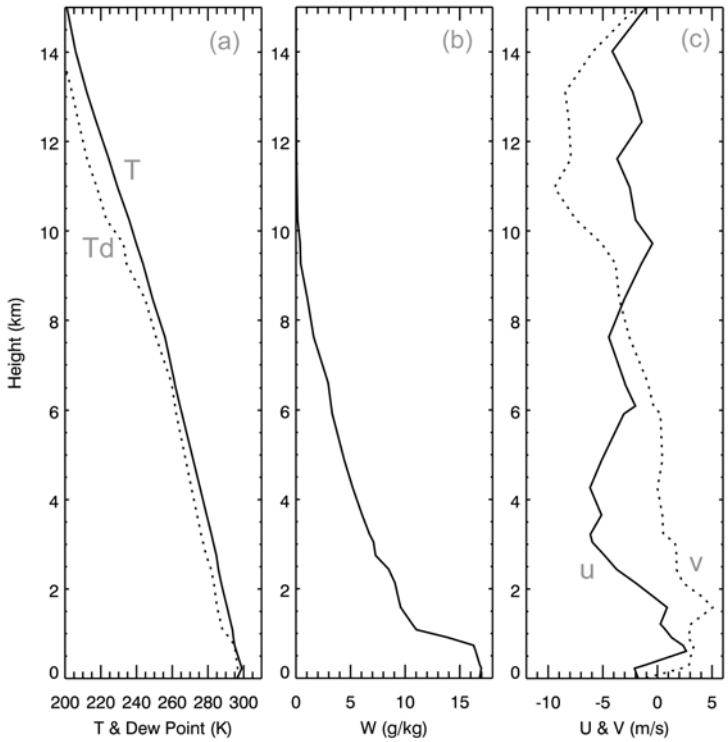

Figure 5.1 Initial profiles of temperature (*T*), dew point (*Td*), water vapor mixing ratio (*w*), and horizontal winds *u* and *v* from a sounding near Houston at 7:00 am on August 24, 2000.

A series of simulations have been performed. We first perform the control run (AR_85) considering aerosol radiative effects. The initial aerosol size distribution in AR_85 is from the modeled results and has been compared with the observations [*Fan et al*., 2006, 2007a, b]. Aerosols are represented by internal BC-cores surrounded by

ammonium sulfate. The preliminary analysis of the recent in-situ measurements of the mixing states of BC during TexAQS 2006 shows about 70% internally mixed BC in the Houston area [*J. P. Schwarz at NOAA*, personal communication]. The mass mixing ratios are assumed to be about 0.1 for BC and 0.9 for ammonium sulfate (Table 5.2). The activation scheme accounting for the effect of the insoluble core is employed to calculate CCN activation [*Fan et al*., 2007a]. As shown in Table 5.2, the mid-visible (at 0.55 μm) AOD, SSA and AF calculated from the aerosol radiative module at the initial time of the

Table 5.1 Selected vegetation and soil characteristics used in PLACE

Vegetation: Broadleaf bushes/trees with groundcover		Soil: sandy clay loam	
Albedo	0.14	Albedo	0.15
% Veg. cover	30%	Porosity	0.42
Leaf area index	4.0	Saturated hydraulic conductivity	6.1×10^{-4}
Root profile layers 1–5	0.00 0.25 0.50 0.20 0.05	Initial soil moisture layers 1–5	0.18–0.21 0.20–0.22 0.23–0.26 0.25–0.28 0.25–0.28
Surface roughness	1.0	% Silt	20%
Minimum stomatal resistance	110.0	% Sand	55%
Biomass heat capacity	5.0	% Clay	25%

Legend: % veg. cover is the percentage of area covered by transpiring vegetation; root profile is the cumulative frequency distribution of roots in the 5 soil moisture reservoirs; surface roughness in m; minimum stomatal resistance is in s m^{-1}; surface biomass (water-equivalent) heat capacity in J K^{-1} m^{-2}. For soil, saturated hydraulic conductivity in m s^{-1}. Initial soil moisture is expressed as volumetric (cm^3 cm^{-3}) soil moisture, the ratio of the volume of soil water to total soil volume.

simulation are 0.27, 0.85, and 0.76, respectively, consistent with the observations in Houston. Generally, the observed mid-visible AOD is between 0.25 and 0.4, and the SSA falls in the range of 0.85-0.95.

Table 5.2 Aerosol properties in numerical simulations

Cases	Composition [a]	Conc. (cm^{-3}) [b]	AOD [c]	SSA [c]	AF [c]
NAR_00	0.9 Ammo. Sulf. 0.1 BC	4.2×10^4	0.0	0.0	0.0
AR_85	0.9 Ammo. Sulf. 0.1 BC	4.2×10^4	0.27	0.85	0.76
SA_100	1.0 Ammo. Sulf.	4.2×10^4	0.25	1.00	0.76
SAC_100	1.0 Ammo. Sulf.	3×10^3	0.009	1.00	0.72

[a] Based on mass mixing ratios.
[b] The concentration is the sum over the aerosol size distribution $dN/d\ln(D_p)$
[c] Values shown here are at the wavelength of 0.55 μm.

In order to isolate the aerosol radiative effects, an additional run NAR_00 is set to be similar with AR_85 except that the aerosol radiative properties, i.e., AOD, SSA, and AF, are set to zeroes (without calling the aerosol radiative module) (Table 5.2). To estimate the aerosol radiative forcing, two other simulations are run for background aerosols (ammonium sulfate only) considering the aerosol radiative effects: one is for the polluted case (SA_100) and the other is for the clean case (SAC_100). SA_100 has the same initial aerosol size distribution as AR_85, but the simple Köhler theory is employed for the activation of ammonium sulfate. SAC_100 has the similar configuration with SA_100, except that the aerosol concentration is only about 7% of

SA_100, which is about 3000 cm^{-3} (sum over the size distribution $dN/d\ln(D_p)$). As show in Table 5.2, the AOD at 0.55 nm is 0.25 for SA_100 and only 0.009 for SAC_100. The values of SSA are 1.0 for both cases because ammonium sulfate only has a scattering effect. An exponential decrease of aerosol concentrations with height is used as the initial condition for all of the simulations, the same as our previous studies [*Fan et al.*, 2007a, b].

Further tests are performed for the sensitivity of aerosol radiative effects to SSA. The mass ratio of BC to ammonium sulfate is varied to give aerosol mixtures with a range of mid-visible SSA: 0.85, 0.9, 0.95, and 1.0 for pure ammonium sulfate. These reflect the typical range of mid-visible SSA values observed in the atmosphere. The tests with the SSA of 0.85 and 1.0 correspond to the simulations AR_85 and SA_100, respectively. The other two tests with SSA = 0.90 and 0.95 have the same configurations as AR_85, with the exception of different mixing ratio of BC to ammonium sulfate. The initial mid-visible AOD decreases gradually from 0.27 to 0.25 as SSA increases from 0.85 to 1.0.

All simulations have been run for 10-hr daytime, from 7:00 -17:00. The analyses are performed for the middle 6 hrs by excluding the model spin-up time, except for the forcing estimates, which are calculated based on the whole daytime simulations.

5.1.2 Validation of the coupled GCE model

Although the surface model PLACE and the Goddard radiation scheme have been validated separately in previously studies [*Lynn et al.*, 1998; *Baker et al.*, 2001; *Mohr et al*., 2003; *Alonge et al*., 2007; Tao et al., 2003b], the fully coupled model

system is validated here by comparing with the observations and other modeling results. Figure 5.2 shows the comparisons of the surface temperature and the downwelling surface infrared fluxes between the modeled values from AR_85 and the observed values from the site of La Porte in Houston [*Zamora et al.*, 2003; 2005]. The modeled surface temperature and the downwelling surface infrared fluxes are in generally agreement with the observations, although the model tends to slightly overestimate the surface temperature and underestimate the downwelling surface infrared fluxes. The sharp decrease in observed temperature at 480 min is attributed to a storm occurring at that site. The maximum difference in the downwelling surface infrared fluxes between the modeled and observed values is only about 10 W m^{-2}. Because of the poor data quality of the sensible and latent heat fluxes in observations, comparisons of those parameters with the values from the MM5 simulations in the study of surface heat fluxes [*Zamora et al.*, 2003] are provided. The modeled maximum sensible and latent heat fluxes from AR_85 are about 314 and 318 W m^{-2}, occurring at 330 and 250 min, respectively. They are consistent with the values of 310 and 300 W m^{-2} at 360 and 300 min, respectively, from MM5 simulations. Also, the modeled maximum surface solar flux is 945 W m^{-2}, consistent with the observed value of 960 W m^{-2}. The good agreement of these parameters with the observations and simulations indicates that the surface model responds correctly to the changes in net radiation and the coupled system is able to provide robust simulations. The overestimation of surface temperature and the earlier peak for heat fluxes have also been observed in some other model studies with PLACE [*Mohr et al*., 2003; *Alonge et al*., 2007].

In addition, the simulated cloud optical depth (τ_c) is compared with the observed τ_c from MODIS satellite observations for deep convective clouds in the area. By averaging the τ_c values from 40 -100 (deep convective clouds), the model yields a value of about 69, close to the observed average value of 73 for the period of August 2002. The analysis of satellite observations indicates that the average τ_c for deep convective clouds from 2002 to 2006 does not change appreciably.

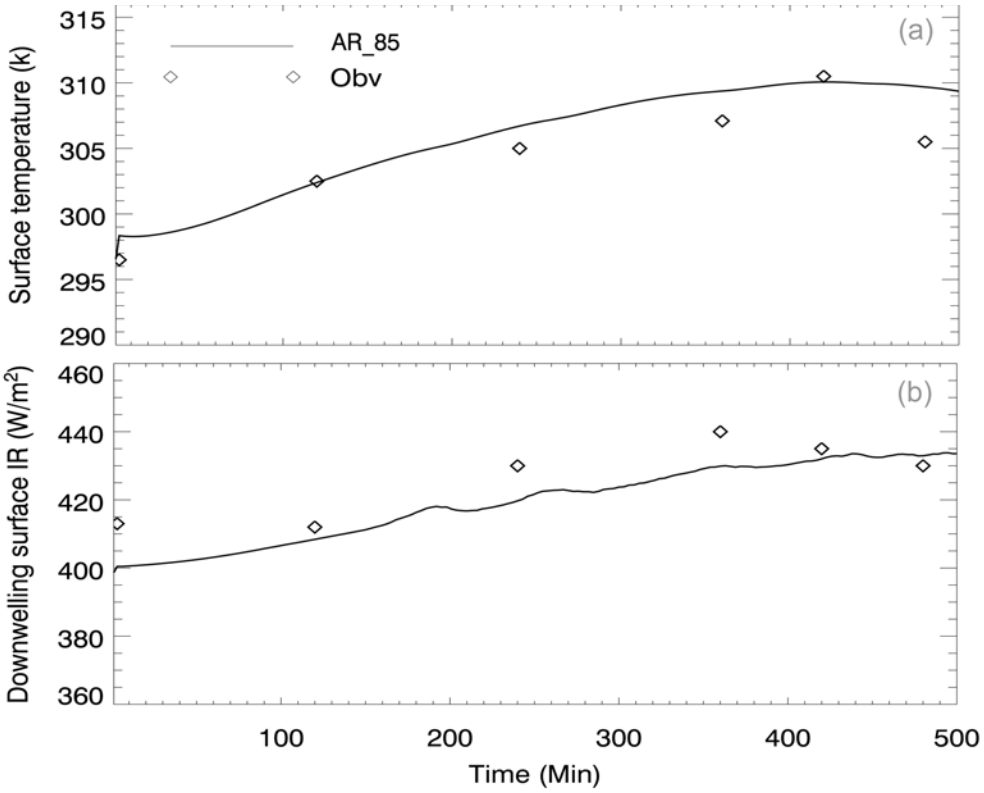

Figure 5.2 Time series of (a) the surface temperature and (b) the downwelling surface infrared fluxes from model simulation AR_85 and observations.

5.2 Results and Discussion

5.2.1 Aerosol radiative effects (ARE)

Comparisons are made between the simulations with (AR_85) and without the ARE (NAR_00). Figure 5.3 shows the time series of cloud microphysical fields averaged over all cloudy grids from 120-480 min. Note that the aerosol composition and initial size distribution are the same for these two simulations. The differences in droplet number concentration between NAR_00 and AR_85 are insignificant since the droplet number is mainly determined by aerosol composition and size distribution (Figure 5.3a). However, the simulation with the ARE (AR_85) has much lower ice particle concentrations than that without the ARE (NAR_00) (Figure 5.3b). The liquid water path (LWP) and ice water path (IWP) for the two cases are presented in Figures 5.3c and 5.3d, respectively. The LWP is defined as the sum of the mass-integrated mixing ratios of cloud water and rain water that determine water clouds, while IWP is defined as the sum of the mass-integrated mixing ratios of ice crystal, snow, graupel, and hail that determine the ice clouds. With the inclusion of the ARE, both LWP and IWP decrease significantly (Figures 5.3c and 5.3d). Also as shown in Figure 5.3, the peak values of cloud microphysical properties are delayed when the ARE is considered. The averaged cloud microphysical properties over the cloudy grids and during the simulation time from 120 to 480 min are shown in Table 5.3. The average ice particle number concentration (N_i) in AR_85 is about 35% lower than that in NAR_00. The average LWP and IWP decrease by about 15% when including the ARE. The ice microphysical properties respond more significantly to the ARE than the warm-cloud microphysical

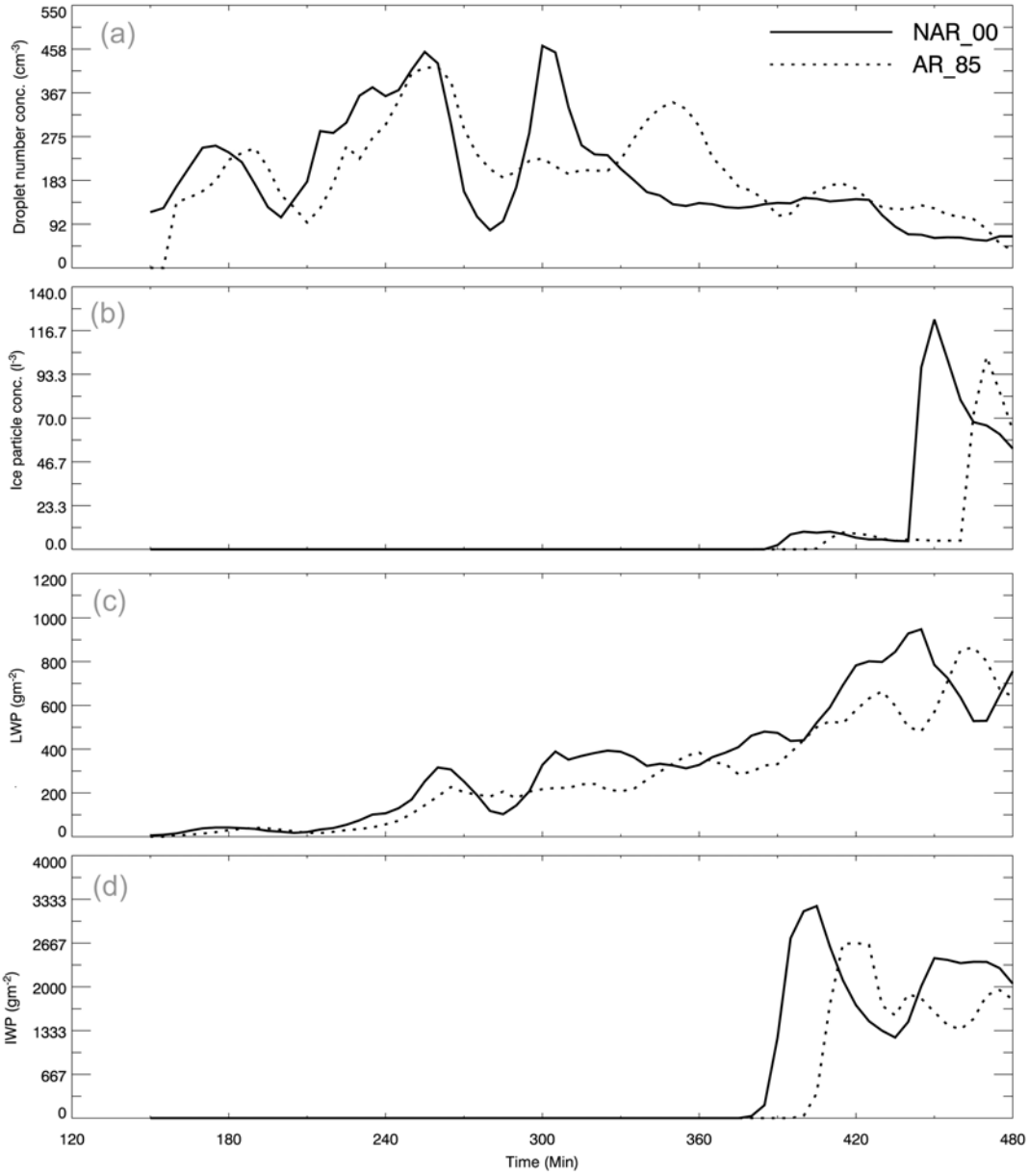

Figure 5.3 Time series of (a) cloud droplet number concentration, (b) ice particle number concentration, (c) LWP, and (d) IWP averaged over the cloud fields for NAR_00 and AR_85.

properties. With the ARE, the droplet effective radius (r_e) becomes significantly smaller, as shown in Figure 5.4. The average r_e decreases from 5.9 μm in NAR_00 to 5.6 μm in

AR_85 (Table 5.3). The vertical profile of r_e (Figure 5.4b) reveals that the differences in r_e are especially noticeable at heights above 6 km, probably because ice processes are more sensitive to aerosol radiative effects.

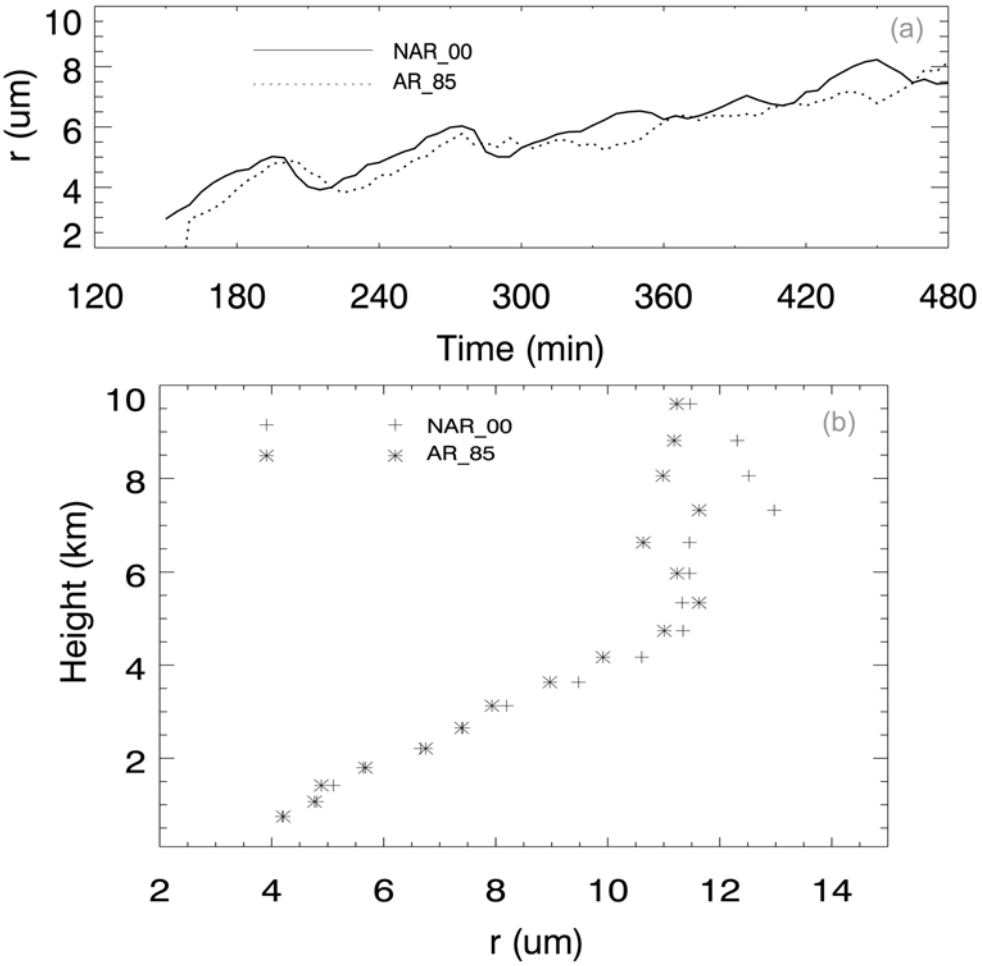

Figure 5.4 (a) Time series of average cloud droplet effective radius (r_e), and (b) the vertical profile of average r_e for NAR_00 and AR_85.

The reduction in the surface radiative fluxes caused by aerosols leads to a decrease in surface heat fluxes and consequently suppresses convection. Figure 5.5

presents the temporal variation of the updraft velocity averaged over the grids with a velocity greater than 1.0 m/s in the simulation domain. Generally, the convective strength is significantly weaker in AR_85 than that in NAR_00. The averaged domain-maximum updraft velocity (w_{max}) during 120-480 min is about 5.0 m/s in NAR_00 and 4.6 m/s in AR_85. The comparisons of surface temperature and heat fluxes between AR_85 and NAR_00 are shown in Figure 5.6. With the ARE, the average surface temperature decreases by about 0.35 K. The surface sensible heat fluxes decrease by up to 28 W m^{-2}, and the latent heat fluxes decrease as well. The decrease in surface heat fluxes suppresses convection and results in less cloudiness. Moreover, the semi-direct effect of BC heats air and leads to a more stable atmosphere, and consequently decreases cloud cover and LWP. The weaker convective strength leads to shallower clouds and then weaker ice processes, resulting in less ice particle concentrations and IWP. As show in Figure 5.7a, the cloud fractions (f_{cld}) averaged over the entire domain in AR_85 are significantly less than those in NAR_00. The f_{cld} decreases by about 18% on average (Table 5.3), with the maximum of over 60%, when the ARE is considered. The cloud optical depth (τ_c) also decreases significantly (Figure 5.7b), with an average value of over 20% (Table 5.3). Figure 5.8 illustrates the vertical profiles of the heating rates averaged over the simulation time of 120-480 min. The heating rates below 5 km in AR_85 are higher than those in NAR_00 due to aerosol absorption. The peak heating rate is at about 2 km with an average value of 2.7 K day^{-1} in AR_85, which is about 0.6 K day^{-1} higher than that in NAR_00. An extra 0.6 K day^{-1} of heating rate resulting from the ARE heats the atmosphere and burns the lower clouds, contributing to significant

decreases in cloud fraction and cloud optical depth as shown in Figure 5.7. The decreases in LWP, cloud fraction, and cloud optical depth by including the ARE have also been found in *Jiang and Feingold* [2006] for warm convective clouds.

Table 5.3 Cloud properties averaged over 120-480 min for the simulations NAR_00, AR_85, SA_100, and SAC_100

Cases	N_c (cm^{-3})	N_i (cm^{-3})	LWP ($g\ m^{-2}$)	IWP ($g\ m^{-2}$)	r_e (μm)	τ_c	f_{cld}	w_{max} (m/s)	r_{rain} (mm/hr)
NAR_00	191.15	34.38	335.69	1944.99	5.85	4.83	0.18	4.98	0.06
AR_85	203.19	22.85	286.91	1684.01	5.59	3.83	0.15	4.57	0.03
SA_100	253.27	31.07	337.88	1721.31	5.50	5.06	0.18	4.82	0.06
SAC_100	12.98	5.11	314.34	1447.58	12.20	1.34	0.21	4.95	0.11

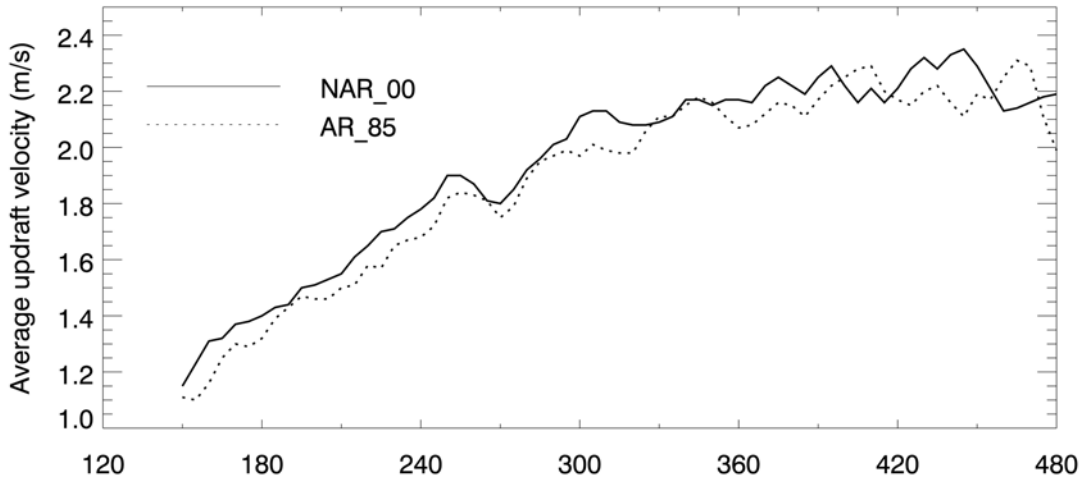

Figure 5.5 Time series of average updraft velocity for NAR_00 and AR_85.

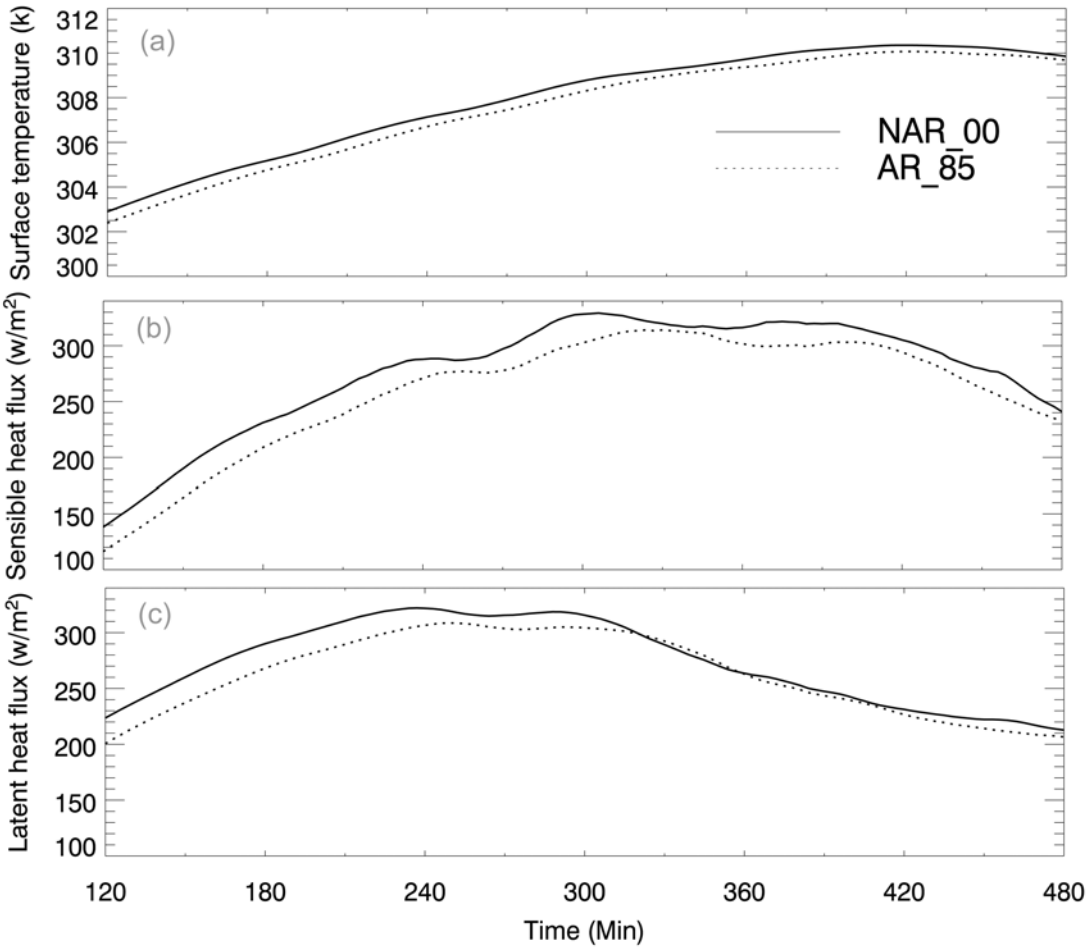

Figure 5.6 Time series of average (a) surface temperature, (b) sensible heat flux, and (c) latent heat flux for NAR_00 and AR_85.

The aerosol radiative effects impact precipitation dramatically. The domain-averaged rain rate (r_{rain}) during 120-480 min is reduced by about 50% (Table 5.3). With the ARE (AR_85), the accumulated rain per grid shown in Figure 5.9 decreases by a factor of 2. The decrease in precipitation primarily results from the shallower clouds due to weaker convection and the desiccation of the cloud layers caused by aerosol semi-direct effect.

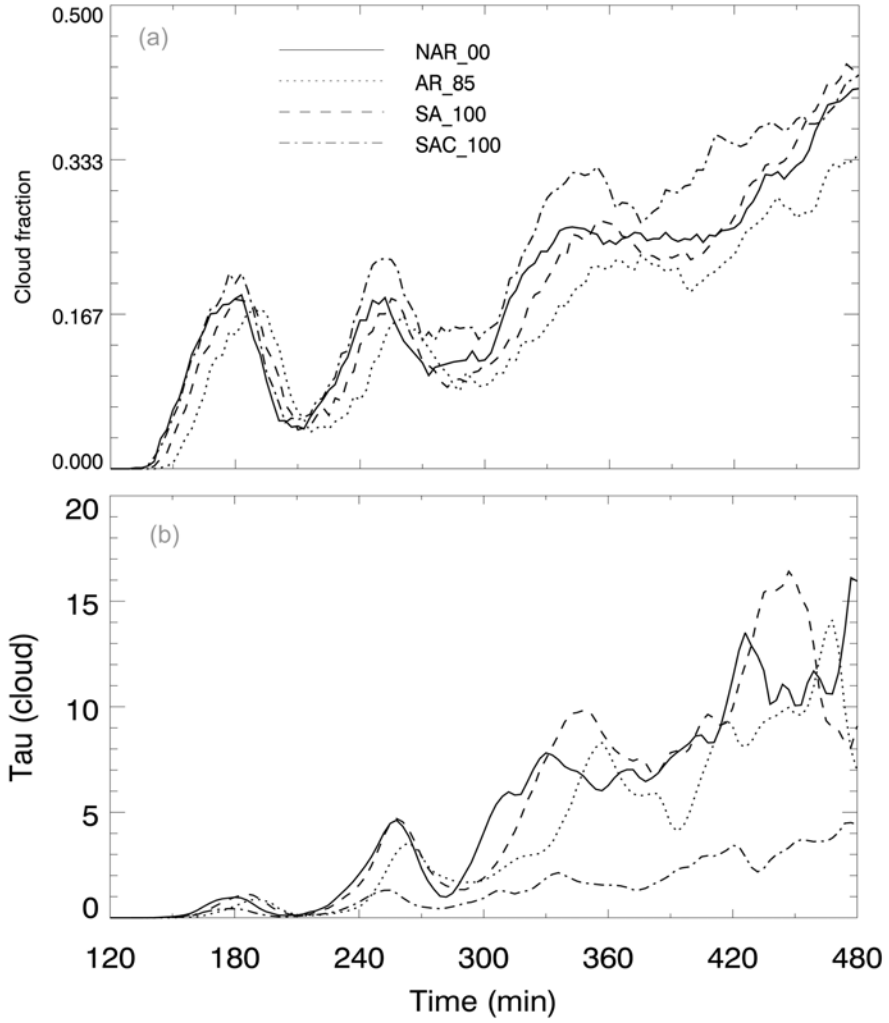

Figure 5.7 Time series of (a) cloud fraction, (b) averaged cloud optical depth over the domain for NAR_00 (solid), AR_85 (dotted), SA_100 (dashed), and SAC_100 (dash-dotted).

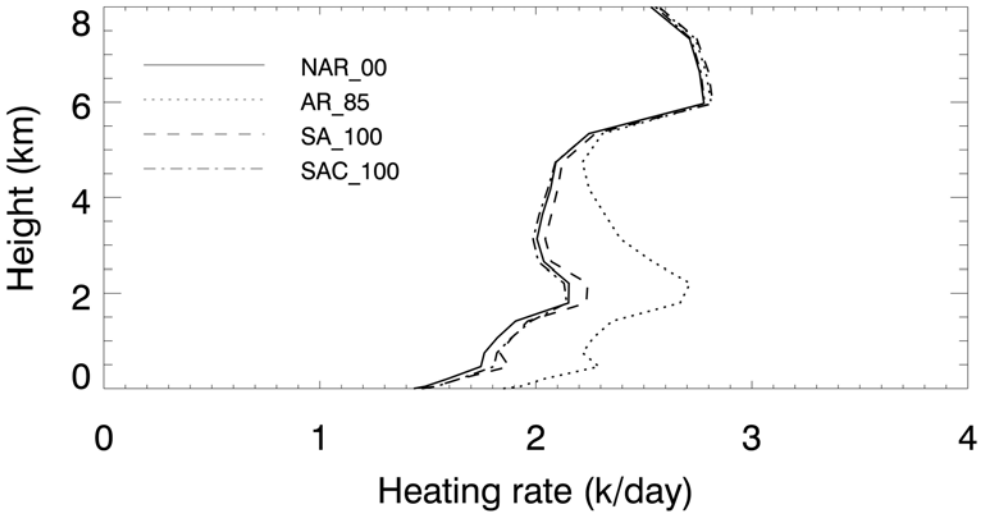

Figure 5.8 Vertical profiles of the heat rates averaged over the horizontal domain for NAR_00, AR_85, SA_100, and SAC_100.

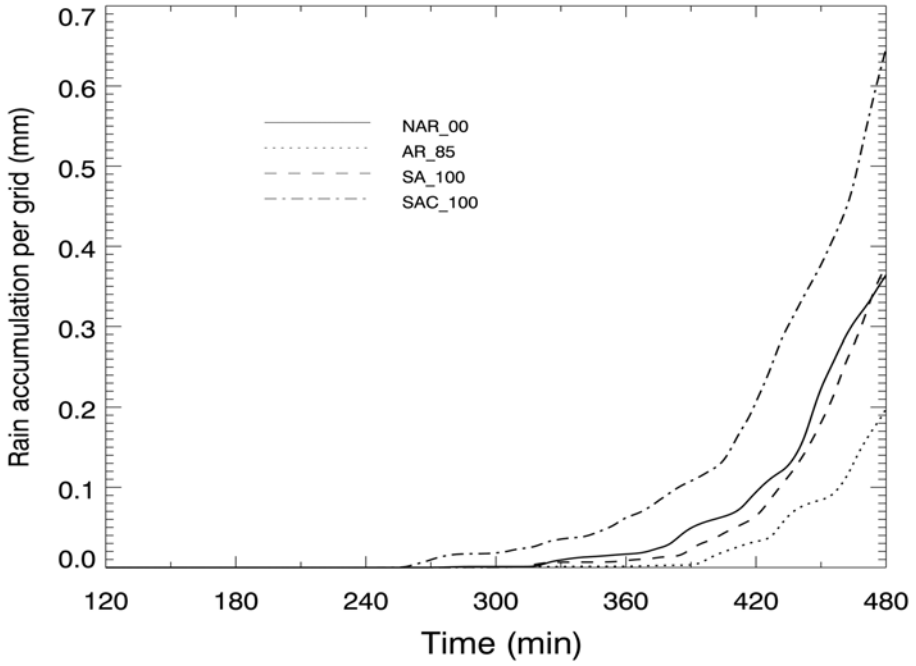

Figure 5.9 Time series of the accumulation rain per grid for NAR_00, AR_85, SA_100, and SAC_100.

In order to estimate the aerosol radiative forcing, the simulations SA_100 and SAC_100 with the background aerosols (ammonium sulfate only) are conducted for the polluted and clean conditions, respectively, with the inclusion of the ARE. Without the absorbing component of aerosols, the cloud fraction and cloud optical depth shown in Figure 5.7 for SA_100 are close to those for NAR_00, but significantly higher than those for AR_85. The clean case (SAC_100) has the largest cloud cover and lowest cloud optical depth, relating to much more convective cells and much larger droplet sizes (Figure 5.7 and Table 5.3). The simulations without the absorbing component of aerosols (i.e., SA_100 and SAC_100) have the similar vertical profiles of the heating rates with the simulation without the ARE (NAR_00), as shown in Figure 5.8. The difference in the average surface temperature between the SA_100 and NAR_00 is about 0.25 K, and the differences in the sensible and latent heat fluxes are only a few W m^{-2}. Therefore, the scattering effect of ammonium sulfate on surface heat fluxes is small. Also as shown in Table 5.3, SA_100 has a higher cloud droplet number concentration (253.3 cm^{-3}) than NAR_00 (191.2 cm^{-3}), resulting from the CCN activation processes. The higher droplet number concentrations are responsible for the smaller droplet size in SA_100. Although the clean case (SAC_100) has a lower cloud droplet and ice particle number concentration, LWP and IWP are higher because of the higher mass content of liquid water and ice water due to efficient growth (Table 5.3). However, compared with three polluted cases (NAR_00, AR_85, and SA_100), the ice particle number concentrations and IWP in SAC_100 are much lower, indicating a weaker ice process in the clean case due to much less droplet number concentrations and much stronger warm rain processes

(coalescence). Figure 5.9 shows much more precipitation for the clean case than for the polluted cases. In contrast to the increases in convection and precipitation with aerosols in our previous study of aerosol indirect effects on a warm-bubble initiated cumulus cloud [*Fan et al.*, 2007b], the convection and precipitation are suppressed by aerosols for the clouds induced by the surface heating through radiation, consistent with the study by *Jiang and Feingold* [2006] for warm convective clouds.

Separate estimates of the direct, semi-direct, and indirect forcing values at the TOA and surface (SFC) are made based on the definitions in *McFarquhar and Wang* [2006]. The total forcing (f_{total}) is the difference in the net radiative fluxes between the simulation for the polluted air with BC (AR_85) and the simulation with the clean background aerosols (SAC_100). The combination of the direct and semi-direct forcing, $f_{direct+semi}$, is defined as the difference in the net fluxes between the simulation for the polluted air with BC (AR_85) and the simulation with the polluted background aerosols (SA_100). The difference in the net fluxes between the simulation with the polluted background aerosols (SA_100) and the simulation with the clean background aerosols (SAC_100) corresponds to the non-absorbing aerosol indirect forcing ($f_{indirect}$). The direct forcing of BC, f_{direct}, is derived from the difference in the clear-sky net fluxes between the simulations of the polluted air with BC (AR_85) and the polluted background aerosols (SA). Table 5.4 summarizes the calculated forcing values for AR_85 averaged over the entire domain and during the daytime (from 7:00 to 17:00 local time). The total aerosol radiative forcing, f_{total}, at the TOA and surface are –11.6 and –31.9 W m^{-2}, respectively, in good agreement with the values of -9 W m^{-2} at the TOA and -30 W m^{-2}

at the surface reported over the Bay of Bengal where the aerosols consisted of soot, sulfate, and organics [*Ramachandran*, 2005]. The semi-direct forcing of BC, f_{semi}, is 10.0 W m^{-2} at the TOA and 11.2 W m^{-2} at the surface. The direct forcing induced by BC is positive (2.2 W m^{-2}) at the TOA, but is strongly negative at the surface (-17.4 W m^{-2}). The sum of direct and semi-direct forcing, $f_{direct+semi}$, warms the TOA by 12.2 W m^{-2} and cools the surface by a smaller magnitude (-6.2 W m^{-2}). Because the semi-direct forcing compensates the direct forcing at the surface, the reduction of the surface fluxes due to the ARE is not so significant, as shown in Figure 5.6. Compared with the semi-direct forcing estimates of 15 W m^{-2} for stratocumulus by *Johnson et al.* [2004] and of 7.5 W m^{-2} for the trade cumulus by *Ackerman et al.* [2000] at the surface, the estimates of 11.2 W m^{-2} reported in the present work is close to the median value between the previous studies. *Xu et al.* [2003] reported a daily-mean surface direct radiative forcing of -11.2 W m^{-2} over Yangtze delta region in China, slightly higher than our daily-mean value of -8.7 W m^{-2} estimated from the daytime-mean value of -17.4 W m^{-2} because of a larger AOD. The TOA indirect radiative forcing ($f_{indirect}$) is estimated to be -23.8 W m^{-2} and the surface $f_{indirect}$ is about -25.7 W m^{-2}, much higher than those reported over the tropical Indian Ocean (INDOEX) by *Ramanathan et al.* [2001b]. For much more polluted air in Houston, the aerosol indirect forcing should be higher than that for the INDOEX case.

Table 5.4 Estimates of radiative forcing for AR_85

W m^{-2}	TOA	SFC
f_{total}	-11.6	-31.9
$f_{direct+semi}$	12.2	-6.2
f_{direct}	2.2	-17.4
f_{semi}	10.0	11.2
$f_{indirect}$	-23.8	-25.7

The differences in the vertical profiles of temperature and relative humidity between the cases with ARE (AR_85) and without ARE (NAR_00) are shown in Figure 5.10. The data are averaged over the whole domain and the timesteps within one hour prior to the cloud formation. Considering the ARE, the temperature near the surface of about 1.5 km decreases but increase for the layers over 1.5 km (Figure 5.10a), indicating a cooling effect near the surface and a warming effect in the elevated atmosphere. The cooling then causes the increase of relative humidity at the bottom of atmosphere, but the warming decreases the relative humidity in the elevated atmosphere (Figure 5.10b). The warming effect decreases the temperature lapse rate in the middle troposphere, leading to a more stable atmosphere. Also, the decrease of relative humidity suppresses convection. In order to find out the contribution of the both effects to the convection, the CAPE changes due to the changes in temperature profile ($\Delta CAPE_T$) and relative humidity ($\Delta CAPE_W$) from the ARE are calculated, respectively. The results show the $\Delta CAPE_T$ are much more negative than $\Delta CAPE_W$, indicating that decreasing the

temperature lapse rate resulting from the ARE may contribute more significantly to the suppression of convection.

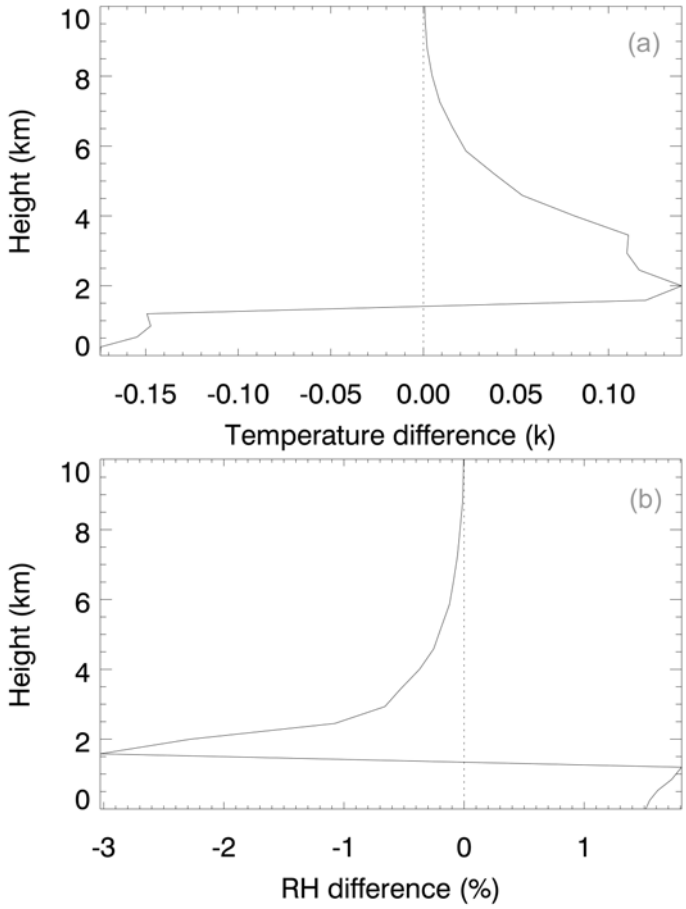

Figure 5.10 Differences in the vertical profiles of temperature and relative humidity between the cases with ARE (AR_85) and without ARE (NAR_00).

5.2.2 Sensitivity to single-scattering albedo (SSA)

Table 5.5 shows the TOA and surface solar radiative fluxes averaged over the entire domain and during the daytime for the simulations with different SSA and the relative net fluxes to the pure ammonium sulfate case (i.e., SSA = 1.0). At the TOA, the

upwelling fluxes ($F^{\uparrow}$(TOA)) are reduced with the decrease of SSA due to the increase of aerosol absorption, leading to an increase in the net solar radiative fluxes (F_{net}(TOA)). The net TOA solar radiative flux increases by 14.05 W m^{-2} when SSA decreases from 1.0 to 0.85, while the net surface solar radiative flux decreases by 5.81 W m^{-2} because of the decrease of the downwelling radiative flux ($F^{\downarrow}$(SFC)) due to the increase of absorption (Table 5.5). Increasing aerosol absorption leads to higher heating rates in the middle troposphere (Figure 5.11). The heating rate at 2 km for SSA = 0.85 is about 0.5 K day^{-1} higher than that for SSA = 1.0. At the surface, the heating rate for SSA = 0.85 is also about 0.3 K day^{-1} higher. This surface heating compensates the negative direct forcing, causing the surface temperature to be insensitive to SSA. As shown in Table 5.6, the average surface temperature (T_{sfc}) decreases slightly from 306.09 to 305.98 K as SSA decreases from 1.0 to 0.85. Consequently, the decreases in the surface sensible (F_{SH}) and latent heat fluxes (F_{LH}) with the decrease of SSA are insignificant (Table 5.6). *Huang et al.* [2007] also found that the surface temperature did not change much because of the canceling effect of semi-direct forcing, consistent with the results reported here.

Table 5.5 The solar radiative fluxes for different SSA and the relative forcing to pure ammonium sulfate (SSA=1.0)

SSA	$F^{\downarrow}$(TOA)	$F^{\uparrow}$(TOA)	$F^{\downarrow}$(SFC)	$F^{\uparrow}$(SFC)	F_{net}(TOA)	F_{net}(SFC)	Net fluxes relative to SSA=1.0	
							TOA	SFC
0.85	986.81	-106.62	657.15	-7.57	880.18	649.58	14.05	-5.81
0.90	986.81	-112.81	658.24	-7.40	874.00	650.85	7.86	-4.55
0.95	986.81	-119.15	659.02	-7.31	867.66	651.71	1.53	-3.68
1.00	986.81	-120.67	662.62	-7.23	866.13	655.39	0.00	0.00

Table 5.6 Cloud and surface fields for different SSA.

SSA	τ_c	f_{cld}	w_{max} (m/s)	Accum. rain per grid (mm)	T_{sfc} (K)	F_{SH} (W m^{-2})	F_{LH} (W m^{-2})
0.85	3.83	0.15	4.56	0.19	305.98	207.67	233.48
0.90	4.15	0.16	4.62	0.28	306.03	210.88	234.57
0.95	4.45	0.17	4.81	0.34	306.06	212.74	235.27
1.00	5.06	0.18	4.82	0.37	306.09	213.88	235.72

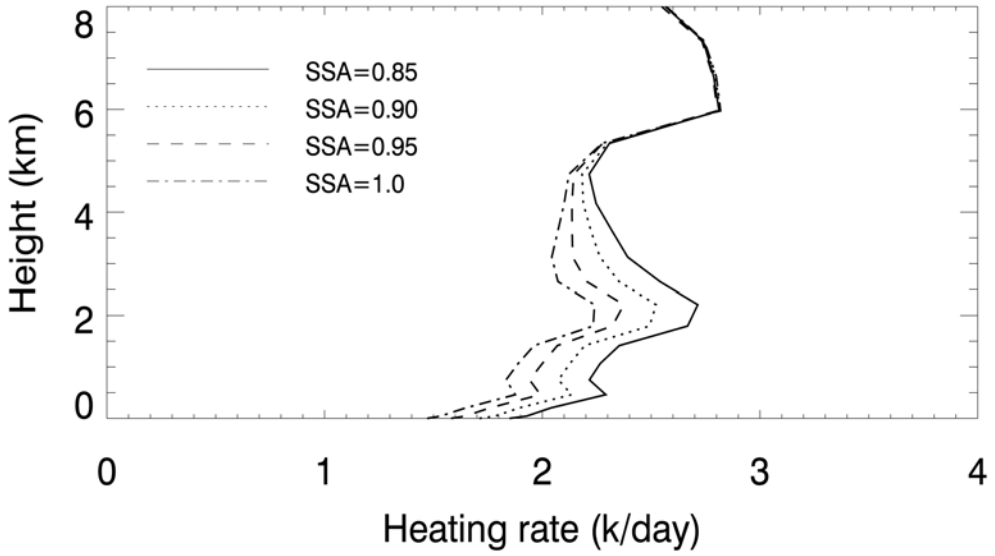

Figure 5.11 Vertical profile of the heat rates averaged over the horizontal domain for SSA of 0.85 (solid), 0.90 (dotted), 0.95 (dashed), and 1.00 (dash-dotted).

Figure 5.12 illustrates the aerosol radiative forcing versus SSA at the TOA (Figure 5.12a) and surface (Figure 5.12b). All the forcing values correspond to the daytime-means. Aerosol absorption generates significant positive direct and semi-direct radiative forcing at the TOA, and the semi-direct effect overwhelms the direct effect for

moderately or strongly absorbing aerosol mixtures (Figure 5.12a). The sum of the direct and semi-direct forcing yields only about 0.6 W m^{-2} positive TOA forcing at SSA = 0.95, but the value increases to 12.1 W m^{-2} at SSA = 0.85. The TOA total radiative forcing values are strongly negative for all SSA cases due to the aerosol indirect effect (Figure 5.12a). The indirect effect related increase in cloud albedo, and subsequently negative TOA forcing, dominates the positive TOA direct and semi-direct forcing above the clouds for this case. This is in agreement with the investigation by *Keil and Haywood* [2003] of the radiative forcing of biomass-burning aerosols in Southern African. Also seen from Figure 5.12a, there is significantly less negative TOA forcing with the decrease of SSA due to the absorption of aerosols induced by BC (semi-direct effect).

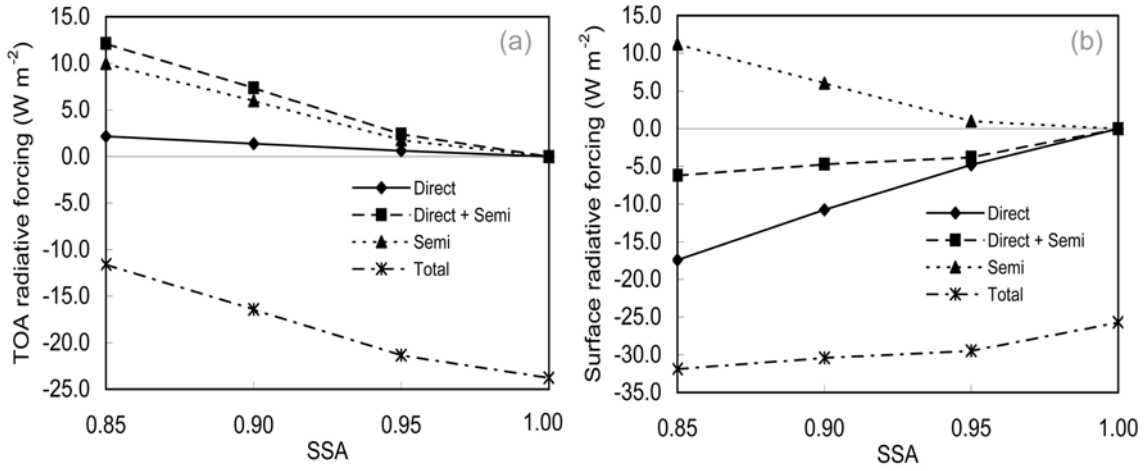

Figure 5.12 The aerosol raidative forcing vs. SSA at the (a) TOA and (b) surface.

At the surface, BC leads to strongly negative direct forcing and the value is up to 17.4 W m^{-2} at SSA = 0.85 (Figure 5.12b). However, the positive semi-direct forcing

partially compensates the negative direct forcing. Thus, the sum of direct and semi-direct forcing is much less negative, with a value of –6.2 W m^{-2} at SSA = 0.85. *Johnson et al.* [2004] indicated that for marine stratocumulus the semi-direct forcing may well exceed the direct forcing even for moderately absorbing aerosols. Both direct and semi-direct effects are very sensitive to SSA at the surface. Note that aerosol indirect forcing is dominant for the deep convective clouds. Therefore, the surface total radiative forcing is much more negative by including the indirect effects, but it is not as sensitive to SSA as the TOA total forcing, due to the compensation of positive semi-direct forcing. The more strongly negative surface radiative forcing for the lower SSA cools the surface and decreases the sensible and latent heat fluxes, leading to weaker convection, less cloudiness and hence lower cloud albedo. These effects are enhanced by the semi-direct effect of absorbing aerosols, which warms air and decreases the relative humidity, enhances the stability of the lower atmosphere. As shown in Table 5.6, the averaged domain-maximum updraft velocity during 120-480 min decreases from 4.82 m/s to 4.56 m/s, and the cloud fraction decreases from 0.18 to 0.15 with the decrease of SSA from 1.0 to 0.85. The domain-averaged cloud optical depth decreases from 5.06 at SSA = 1.0 to 3.83 at SSA = 0.85.

As illustrated in the section 5.2.1, the aerosol radiative effects reduce the precipitation. With the increase of absorption (i.e., decrease of SSA), the accumulated rain per grid averaged over 120 to 480 min decreases significantly (Table 5.6). The reduction in precipitation with the decrease of SSA is likely caused by the increase in thermal stability from the BC-induced surface cooling and atmospheric heating, which

inhibits cloud formation. The suppressed precipitation has also been found in a study over the east of Asia on the radiative effect of core-coated internally mixed aerosols containing BC [*Huang et al*., 2007].

5.3 Summary

Aerosol radiative effects on cloud properties are pronounced for mid-visible SSA of 0.85. Relative to the case excluding the ARE, cloud fraction and optical depth decrease by about 18% and 20%, respectively. Cloud droplet and ice particle number concentrations, LWP, IWP, and droplet size decrease significantly when the ARE is introduced. The results also reveal that the ice microphysical properties respond much more significantly to the ARE than the warm-rain microphysical properties. The ARE causes a surface cooling of about 0.35 K and significantly high heating rates in the lower troposphere (about 0.6 K day^{-1} higher at 2 km), both of which lead to a more stable atmosphere and hence weaker convection. The semi-direct effect of aerosols warms the atmosphere and decreases the relative humidity, and then suppresses convection. The weaker convection explains the less cloudiness, lower cloud optical depth, less LWP and IWP, smaller droplet size, and less precipitation resulting from the ARE. The daytime-mean direct forcing induced by black carbon is about 2.2 W m^{-2} at the TOA and -17.4 W m^{-2} at the surface for SSA = 0.85. The positive semi-direct forcing of 11.2 W m^{-2} compensates the negative direct forcing at the surface, causing a much less negative forcing. Both the TOA and surface total radiative forcing values are strongly negative for the deep convective clouds, about -11.6 and -31.9 W m^{-2}, respectively, attributed mostly to aerosol indirect forcing.

Aerosol direct and semi-direct effects are very sensitive to SSA. The TOA semi-direct forcing increases significantly with the decrease of SSA by decreasing the upwelling radiative fluxes due to the increase of aerosol absorption. At the surface, decreasing SSA (increasing absorption) leads to a significant reduction of direct forcing, and a significant increase of semi-direct forcing. Because the positive semi-direct forcing compensates the negative direct forcing at the surface, the surface temperature and heat fluxes decrease less significantly. The aerosol indirect forcing is dominant for deep convective clouds. The cloud fraction, optical depth, convective strength, and precipitation decrease with the increase of absorption, resulting from a more stable atmosphere due to enhanced surface cooling and atmospheric heating.

6. CONCLUSIONS

This work covers the investigation of aerosol characteristics, aerosol indirect effects under different aerosol and relative humidity conditions, and radiative effects of anthropogenic aerosols containing absorbing components on deep convective clouds in the Houston area by modeling simulations. The aerosol characteristics such as aerosol composition and number size distribution have been investigated by using the EPA's Models-3/CMAQ [*Fan et al.*, 2005; 2006]. The aerosol effects on cumulus clouds have been scrutinized by employing a cloud-resolving model, GCE, with a spectral-bin microphysics. Firstly, the aerosol indirect effects on the cumulus clouds have been separately investigated through cloud microphysical processes. Based on the simulation of a convective cloud event occurring in Houston on August 24, 2000, sensitivity studies have been conducted under different aerosol compositions, concentrations and size distributions to investigate aerosol indirect effects on cloud microphysical and dynamical properties [*Fan et al.*, 2007a; 2007b]. Then, the GCE model has been updated and modified by incorporating the aerosol and cloud radiation processes and the land-atmosphere interaction processes to comprehensively examine the aerosol effects on the deep convective clouds with the focus on radiative effects of anthropogenic aerosol containing black carbon [*Fan et al.*, 2007c].

The major components of the fine particles in the Houston area are sulfate, organic carbon, elemental carbon and ammonium with the predicted mass contents of about 30%, 27%, 5%, and 10% of total $PM_{2.5}$ mass, respectively. The black carbon mass

concentrations are high, up to 2.0 μg m^{-3}, and spatially inhomogeneous. The predicted daily $PM_{2.5}$ mass concentrations are about 8.5-13.0 μg/m^3, comparable to the measured values. A parameterized organic nucleation scheme accounting for the enhanced nucleation effects of secondary condensable organics predicts number concentrations of ultrafine particles in agreement with the measurements. The average total aerosol number concentrations during the daytime are over 10^4 cm^{-3}, with the high values of over 10^5 cm^{-3} frequently.

The cloud microphysical and macrophysical properties change considerably with the aerosol chemical properties. With varying the aerosol composition from only $(NH_4)_2SO_4$, $(NH_4)_2SO_4$ with soluble organics, to $(NH_4)_2SO_4$ with slightly soluble organics, the number of activated aerosols in cloud decreases gradually, leading to a decrease in the cloud droplet number concentration and an increase in the droplet size. Increasing activated aerosols results in the increase of ice crystal formation by homogeneous freezing, more extensive riming, lower supersatuation (S_w and S_{ice}), less efficient growth of graupel, and more melting precipitation. Ice microphysical processes are more sensitive to the changes of aerosol chemical properties than the warm rain processes. The changes in macrophysical properties are more evident: the increase of activated aerosols resulted in longer cell lifetime, larger cell size, stronger secondary convective cell and more accumulated precipitation.

The cloud properties are considerably influenced by the aerosol type and concentration. The maritime aerosol results in more intensive radar reflectivity in both developing and mature stages than the continental aerosol in polluted air. For the

continental case, the increase of initial aerosol concentration generally leads to a stronger convection. The most noticeable effect of increasing aerosol is the increases of the cloud droplet number concentration and cloud water content, but a decrease in the effective radius of cloud droplet. These changes lead to more extensive collection of small droplets by large drops and ice riming of supercooled droplets. The increase of the convection promotes the upward transport of the liquid drops, which leads to a faster formation of ice particles and retards ice particle sedimentation. We show that the total amount of precipitation and rain rate increase with aerosols, confirming measurements of precipitation enhancement reported previously [*Shepherd and Burian*, 2003]. More melting precipitation and stronger secondary clouds contribute to the enhanced precipitation with increasing aerosols.

The cloud development is dramatically affected by relative humidity. As RH increases from 40 to 70% at the surface, the cloud changes from shallow warm to deep convective types due to the significant increase of CAPE. The aerosol effects on the cloud microphysical properties and precipitation are found to be strongly dependent on RH: the effects are negligible in dry air (40% RH) but significant in humid air (60-70% RH). The aerosol effects on the convective strength and the rain rate are significant in the humid air. The rain delay is found to be sensitive to RH, but not very sensitive to aerosol under the same initial thermodynamic conditions.

Our results reveal that in continental aerosol environments, the aerosol indirect effect on deep convective clouds is consistent with the Twomey effect, but the effect is non-linear. The aerosol indirect effect on deep convection is more pronounced in

relatively clean air than in heavily polluted air, implying that aerosols may play a more important role in moist and clean marine environments [*Zhang et al*., 2007].

Aerosol radiative effects on cloud properties are pronounced for mid-visible SSA of 0.85. Relative to the case excluding the ARE, cloud fraction and optical depth decrease by about 18% and 20%, respectively. Cloud droplet and ice particle number concentrations, LWP, IWP, and droplet size decrease significantly when the ARE is introduced. The results also reveal that the ice microphysical properties respond much more significantly to the ARE than the warm-rain microphysical properties. The ARE causes a surface cooling of about 0.35 K and significantly high heating rates in the lower troposphere (about 0.6 K day^{-1} higher at 2 km), both of which lead to a more stable atmosphere and hence weaker convection. The semi-direct effect of aerosols warms the atmosphere and decreases the relative humidity, and then suppresses convection. The weaker convection explains the less cloudiness, lower cloud optical depth, less LWP and IWP, smaller droplet size, and less precipitation resulting from the ARE. The daytime-mean direct forcing induced by black carbon is about 2.2 W m^{-2} at the TOA and -17.4 W m^{-2} at the surface for SSA = 0.85. The positive semi-direct forcing of 11.2 W m^{-2} compensates the negative direct forcing at the surface, causing a much less negative forcing. Both the TOA and surface total radiative forcing values are strongly negative for the deep convective clouds, about -11.6 and -31.9 W m^{-2}, respectively, attributed mostly to aerosol indirect forcing.

Aerosol direct and semi-direct effects are very sensitive to SSA. The TOA semi-direct forcing increases significantly with the decrease of SSA by decreasing the

upwelling radiative fluxes due to the increase of aerosol absorption. At the surface, decreasing SSA (increasing absorption) leads to a significant reduction of direct forcing, and a significant increase of semi-direct forcing. Because the positive semi-direct forcing compensates the negative direct forcing at the surface, the surface temperature and heat fluxes decrease less significantly. The aerosol indirect forcing is dominant for deep convective clouds. The cloud fraction, optical depth, convective strength, and precipitation decrease with the increase of absorption, resulting from a more stable atmosphere due to enhanced surface cooling and atmospheric heating.

Our studies reveal that the aerosol effects on clouds and precipitation are strongly dependent on aerosol properties and cloud thermodynamic and dynamic conditions. In a single cumulus cloud initiated by a warm bubble, aerosol indirect effects are found to be dominant and lead to stronger convection, larger cloud coverage, and enhanced precipitation [*Fan et al.*, 2007a, b]. However, for absorbing aerosols and the clouds induced by surface heat fluxes through radiation, aerosol radiative effects are significant, which suppress convection and lead to less cloud fraction, lower cloud optical depth, and less precipitation.

REFERENCES

Ackerman, A. S., O. B. Toon, D. E. Stevens, A. J. Heymsfield, V. Ramanathan, and E. J. Welton (2000), Reduction of tropical cloudiness by soot, *Science*, *288*, 1042-1047.

Albrecht, B. A. (1989), Aerosols, cloud microphysics, and fractional cloudiness, *Science*, *245*, 1227–1230.

Allen, D. (2002), Fine particulate matter concentrations, compositions, and sources in southeast Texas: State of the science and critical research needs, version 1.0, report, University of Texas at Austin, Austin, Texas.

Alonge, C. J., K. I. Mohr, and W.-K. Tao (2007), Numerical case studies of wet vs. dry regimes in the West African Sahel. *J. Hydrometeor.*, *8*, 102–116.

Andreae, M. O., D. Rosenfeld, P. Artaxo, A. A. Costa, G. P. Frank, K. M Longo, and M. A. F. Silva-Dias (2004), Smoking rain clouds over the Amazon, *Science*, *303*, 1337–1341.

Arnold, J. R., R. L. Dennis, and G. S. Tonnesen (2003), Diagnostic evaluation of numerical air quality models with specialized ambient observations: testing the Community Multiscale Air Quality modeling system (CMAQ) at selected SOS 95 ground sites, *Atmos. Environ.*, *37*, 1185-1198.

Baker, R. D., B. H. Lynn, A. Boone, W.-K. Tao, J. Simpson (2001), The influence of soil moisture, coastline curvature, and the land-breeze circulation on sea-breeze initiated precipitation, *J. Hydrometeorol.*, *2*, 193–211.

Berkowitz, C.M., T. Jobson, G.F. Jiang, C.W. Spicer, and P.V. Doskey (2004), Chemical and meteorological characteristics associated with rapid increases of O_3 in Houston, Texas, *J. Geophys. Res*., *109*, doi:10.1029/2003JD004141.

Binkowski, F. S., and U. Shankar (1995), The regional particulate matter model, 1, Model description and preliminary results, *J. Geophys. Res., 100*, 26,191-26,209.

Binkowski, F. S., and S. J. Roselle (2003), Models-3 Community Multiscale Air Quality (CMAQ) model aerosol component, 1, Model description, *J. Geophys. Res.*, *108*(D6), 4183, doi:10.1029/2001JD001409.

Bohren, C. F., D. R. Huffman (1983), *Absorption and Scattering of Light by Small Particles*, John Wiley & Sons, New York.

Bréon, F.-M., D. Tanré, and S. Generoso **(**2002), Aerosol effect on cloud droplet size monitored from satellite, *Science*, *295*, 834–838.

Brock, C. A., M. Trainer, T. B. Ryerson, J. A. Neuman, D. D. Parrish, J. S. Holloway, D. K. Nicks Jr., G. J. Frost, G. Hubler, F. C. Fehsenfeld, J. C. Wilson, J. M. Reeves, B. G. Lafleur, H. Hilbert, E. L. Atlas, S. G. Donnelly, S. M. Schauffler, V. R. Stroud, and C. Wiedinmyer (2003), Particle growth in urban and industrial plumes in Texas, *J. Geophys. Res.*, *107*(D12), 4155, doi:10.1029/2001JD002746.

Businger, J .A., J. C. Wyngaard, Y. Izumi, and E. F. Bradley (1971), Flux-profile relationships in the atmospheric surface layer. *J. Atmos. Sci.*, 28, 181-189.

Chang, J. S., P. B. Middleton, W. R. Stockwell, C. J. Walcek, J. E. Pielm, H. H. Lansford, S. Madronich, F. S. Binkowski, N. L. Seaman, D. R. Stauffer, D. Byun, J. N. McHenry, H. Hass, and P. J. Samson (1991), The regional acid decomposition model and engineering model, in *Acidic Deposition: State of Science and Technology*, vol. 1, *NAPAP SOS/T Rep. 4*, Natl. Acid Precip. Assess. Program, Washington, DC.

Charlson, R. J., J. E. Lovelock, M. O. Andreae, and S. G. Warren (1987), Oceanic phytoplankton, atmospheric sulphur, cloud albedo and climate, *Nature*, *326*, 655-662.

Chazette, P., and C. Liousse (2001), A case study of optical and chemical ground apportionment for urban aerosols in Thessaloniki, *Atmos. Environ.*, *35*, 2497–2506.

Chou, M.-D., M. J. Suarez (1999), A shortwave radiation parameterization for atmospheric studies, *15*, *NASA/TM-104606*, pp 40, NASA/Goddard Space Flight Center, Greenbelt, MD.

Chou, M.-D., K.-T. Lee, S.-C. Tsay, Q. Fu (1999), Parameterization for cloud longwave scattering for use in atmospheric models, *J. Clim.*, *12*, 159–169.

Chuang, C. (2003), Find the missing piece in the climate change puzzle, http://www.llnl.gov/str/April03/Chuang.html, *UCRL-52000-03-4*, Lawrence Livermore National Laboratory, Livermore, CA.

Clark, T. L. (1973), Numerical modeling of the dynamics and microphysics of warm cumulus convection. *J. Atmos. Sci.*, *30*, 857–878.

Eder, B. K., M. R. Mebust, F. S. Binkowski, and S. J. Roselle (2000), A preliminary evaluation of Models-3/CMAQ using visibility parameters, paper presented at International Symposium on the Measurement of Toxic and Related Air Pollutants, Environ. Prot. Agency, Research Triangle Park, NC.

Ekman, A. M. L., C. Wang, J. Wilson, and J. Ström (2004), Explicit simulations of aerosol physics in a cloud-resolving model: a sensitivity study based on an observed convective cloud, *Atmos. Chem. Phys.*, *4*, 773-791.

Elleman, R. A., R. A. Kotchenruther, D. S. Covert, C. F. Mass, and C. J. (2004), CAMQ aerosol number and mass evaluation for Pacific Northwest, Models-3 User's workshop, Research Triangle Park, NC.

Elleman, R. A., R. A. Kotchenruther, D. S. Covert, C. F. Mass, and C. J. (2005), CAMQ aerosol number and mass evaluation for Pacific Northwest, 7th conference on atmospheric chemistry, the 85th AMS annual meeting, San Diego, CA.

Environmental Protection Agency (EPA) (1996), Air quality criteria for particulate matter, *Rep. EPA/600/p-95/001cF*, Research Triangle Park, NC.

Environmental Protection Agency (EPA) (1999), Science algorithms of the EPA Models-3 Community Multiscale Air Quality (CMAQ) modeling system, *Rep. EPA/600/R-99/030*, Research Triangle Park, NC.

Environmental Protection Agency (EPA) (2000), National air quality and emissions trend report, 1998, *Rep. EPA/454/R-00-003/00*, Off. of Air Qual. Plann. and Stand., Research Triangle Park, NC.

Environmental Protection Agency (EPA) (2003), Models-3 Community Multiscale Air Quality (CMAQ) model, version 4.3, report, Research Triangle Park, NC.

Fan, J., R. Zhang, G. Li, J. Nielsen-Gammon, and Z. Li (2005), Simulations of fine particulate matter ($PM_{2.5}$) in Houston, Texas, *J. Geophys. Res.*, *110*, D16203, doi:10.1029/2005JD005805.

Fan, J., R. Zhang, D. Collins, and G. Li (2006), Contribution of secondary condensable organics to new particle formation: a case study in Houston, Texas, *Geophys. Res. Lett.*, *33*, L15802, doi:10.1029/2006GL026295.

Fan, J., R. Zhang, G. Li, W.-K. Tao, and X. Li (2007a), Simulations of cumulus clouds using a spectral microphysics cloud-resoving model, *J. Geophys. Res.*, *112*, D04201, doi:10.1029/2006JD007688.

Fan, J., R. Zhang, G. Li, and W.-K. Tao (2007b), Effects of aerosols and relative humidity on cumulus clouds, *J. Geophys. Res.*, doi:10.1029/2006JD008136, in press.

Fan, J., R. Zhang, W.-K. Tao, and K. I. Mohr (2007c), Aerosol radiative effects on deep convective clouds and the related forcing, *J. Geophys. Res.*, submitted.

Fast, J. D., W. I. Gustafson Jr., R. C. Easter, R. A. Zaveri, J. C. Barnard, E. G. Chapman, G. A. Grell, and S. E. Peckham (2006), Evolution of ozone, particulates, and aerosol direct radiative forcing in the vicinity of Houston using a fully coupled meteorology-chemistry-aerosol model, *J. Geophys. Res.*, *111*, D21305, doi:10.1029/2005JD006721.

Feingold, G., L. A. Remer, J. Ramaprasad, and Y. J. Kaufman (2001), Analysis of smoke impact on clouds in Brazilian biomass burning regions: An extension of Twomey's approach, *J. Geophys. Res.*, *106*, 22,907–22,922.

Feingold, G., H. Jiang, and J. Y. Harrington (2005), On smoke suppression of clouds in Amazonia, *Geophys. Res. Lett.*, *32*, L02804, doi:10.1029/2004GL021369.

Ghan, S. J., R. C. Easter, E. G. Chapman, H. Abdul-Razzak, Y. Zhang, L. R. Leung, N. Laulainen, R. D. Saylor, and R. Zaveri (2001a), A physically-based estimate of radiative forcing by anthropogenic sulfate aerosol, *J. Geophys. Res.*, *106*, 5279–5293.

Ghan, S. J., N. S. Laulainen, R. C. Easter, R. Wagener, S. Nemesure, E. G. Chapman, Y. Zhang, and L. R. Leung (2001b), Evaluation of aerosol direct radiative forcing in MIRAGE, *J. Geophys. Res.*, *106*, 5295–5316.

Ghan, S. J., R. C. Easter, and F.-M. Bréon (2001c), Evaluation of aerosol indirect radiative forcing in MIRAGE, *J. Geophys. Res.*, *106*, 5317–5334.

Gasparini, R., R. J. Li, and D. R. Collins (2004), Integration of size distributions and size-resolved hygroscopicity measured during the Houston Supersite for compositional categorization of the aerosol, *Atmos. Environ.*, *38*, 3285–3303.

Hall, W. D. (1980), A detailed microphysical model within a 2-dimensional dynamic framework: Model description and preliminary results, *J. Atmos. Sci.*, *37*, 2486-2507.

Hänel, G**.** (1976), The properties of atmospheric particles as functions of the relative humidity at thermodynamic equilibrium with surrounding moist air, *Adv. Geophys.*, *19*, 73–188.

Hansen, J., M. Sato, and R. Ruedy (1997), Radiative forcing and climate response, *J. Geophys. Res.*, *102*, D6, 6832-6864.

Hegg, A. D., J. Livingston, P. V. Hobbs, T. Novakov, and P. Russell (1997), Chemical apportionment of aerosol column optical depth off the mid-Atlantic coast of the United States, *J. Geophys. Res.*, *102*, 25,293–25,303.

Heymsfield, A., and G. M. McFarquhar (2001), Microphysics of INDOEX clean and polluted trade cumulus clouds, *J. Geophys. Res.*, *106*, 28,653–28,673.

Hobbs, P. V. (Ed.) (1993), *Aerosol-Cloud Interaction*, *Int. Geophys. Ser.*, vol. 54, 237 pp., Elsevier, New York.

Houghton, J. T., Y. Ding, D. J. Griggs, M. Noguer, P. J. van der Linden, X. Dai, K. Maskell, and C. A. Johnson (2001), *Climate Change 2001: The Scientific Basis. Contribution of Working Group 1 to the Third Assessment Report of the Intergovernmental Panel on Climate Change*, Cambridge University Press, Cambridge.

Huang, Y., W. L. Chameides, and R. E. Dickinson (2007), Direct and indirect effects of anthropogenic aerosols on regional precipitation over east Asia, *J. Geophys. Res.*, *112*, D03212, doi:10.1029/2006JD007114.

Intergovernmental Panel on Climate Change (2001), *Climate Change 2001: The Scientific Basis. Contribution of Working Group 1 to the Third Assessment Report*, edited by J. T. Houghton et al., 881 pp., Cambridge Univ. Press, New York.

Jiang, H., and G. Feingold (2006), Effect of aerosol on warm convective clouds: Aerosol-cloud-surface flux feedbacks in a new coupled large eddy model, *J. Geophys. Res.*, *111*, D01202, doi:10.1029/2005JD006138.

Jiang, H., H. Xue, A. Teller, G. Feingold, and Z. Levin (2006), Aerosol effect on the lifetime of shallow cumulus, *Geophys. Res. Lett.*, *33*, doi:10.1029/2006GL026024.

Jiang, W., and H. Roth (2003), A detailed review and analysis of science, algorithms, and code in the aerosol components of Models-3/CMAQ, *Report No. Pet-1534-03s*, Technical Report Program of Energy Research and Development, Natural Resources Canada.

Jacobson, M. Z. (1997), Development and application of a new air pollution modeling system, II, Aerosol module structure and design, *Atmos. Environ.*, *31*, 131–144.

Johnson, B. T., K. P. Shine, and P. M. Forster (2004), The semi-direct aerosol effect: impact of absorbing aerosols on marine stratocumulus, *Q. J. R. Meteorol. Soc.*, *130*, 1407-1422.

Johnson, D., W.-K. Tao, J. Simpson, and C.-H. Sui, (2002), A study of the response of deep tropical clouds to large-scale processes, Part I: Model set-up strategy and comparison with observation, *J. Atmos. Sci.*, *59*, 3492-3518.

Jun, M., and M. L. Stein (2004), Statistical comparison of observed and CMAQ modeled daily sulfate levels, *Atmos. Environ.*, *38*, 4427-4436.

Kaufman, Y. J., and I, Koren (2006), Smoke and pollution aerosol effect on cloud cover, *Science*, *313*, 655-658.

Kessler, E. (1969), On the distribution and continuity of water substances in atmospheric circulations. *Meteor. Monogr.*, *32*, AMS, 84pp.

Keil, A., and J. M. Haywood (2003), Solar radiative forcing by biomass burning aerosol particles during SAFARI 2000: A case study based on measured aerosol and cloud properties, *J. Geophys. Res.*, *108*(D13), 8467, doi:10.1029/2002JD002315.

Khain, A. P., I. Sednev, and V. Khvorostyanov (1996), Simulation of coastal circulation in the Eastern Mediterranean using a spectral microphysics cloud ensemble model, *J. Climate.*, *9*, 3298–3316.

Khain, A. P., A. Pokrovsky, and I. Sednev (1999), Some effects of cloud–aerosol interaction on cloud microphysics structure and precipitation formation: Numerical experiments with a spectral microphysics cloud ensemble model, *Atmos. Res.*, *52*, 195–220.

Khain, A. P., M. Ovtchinnikov, M. Pinsky, A. Pokrovsky, and H. Krugliak (2000), Notes on the state-of-the-art numerical modeling of cloud microphysics, *Atmos. Res.*, *55*, 159–224.

Khain, A. P., A. Pokrovsky, M. Pinsky, A. Seifert, and V. Phillips (2004), Simulation of effects of atmospheric aerosols on deep turbulent convective clouds using a spectral microphysics mixed-phase cumulus cloud model. Part I: Model description and possible applications, *J. Atmos. Sci.*, *61*, 2963–2982.

Khain, A. P., and A. Pokrovsky (2004), Simulation of effects of atmospheric aerosols on deep turbulent convective clouds using a spectral microphysics mixed-phase cumulus cloud model. Part II: Sensitivity Study, *J. Atmos. Sci.*, *61*, 2983–3001.

Khain, A. P., D. Rosenfeld, and A. Pokrovsky (2005), Aerosol impact on the dynamics and microphysics of deep convective clouds, *Q. J. R. Meteorol. Soc.*, *131*, 1-25.

Khvorostyanov, V. I., A. P. Khain, and E. L. Kogteva (1989), A two-dimensional non-stationary microphysical model of a three-phase convective cloud and evaluation of the effects of seeding by crystallizing reagent, *Sov. Meteor. Hydrol.*, *5*, 33–45.

Klemp, J. B., and R. Wilhelmson, (1978), The simulation of three-dimensional convective storm dynamics, *J. Atmos. Sci*., *35*, 1070-1096.

Kogan, Y. (1991), The simulation of a convective cloud in a 3D model with explicit microphysics. Part I: Model description and sensitivity experiments, *J. Atmos. Sci.*, *48*, 1160–1189.

Koren, I., Y. J. Kaufman, D. Rosenfeld, L. A. Remer, Y. Rudich (2005), Aerosol invigoration and restructuring of Atlantic convective clouds, *Geophys. Res. Lett.*, *32*, L14828, doi:10.1029/2005GL023187.

Kratz, D. P., M.-D. Chou, M.-H., Yan, C.-H. Ho (1998), Minor trace gas radiative forcing calculations using the k-distribution method with one-parameter scaling, *J. Geophy. Res.*, *103*, 31647–31656.

Kulmala, M., A. Laaksonen, and L. Pirjola (1998), Parameterizations for sulfuric acid/water nucleation rates, *J. Geophys. Res*. *103*, 8301-8307.

Kulmala, M., H. Vehkamaki, T. Petaja, M. Dal Maso, A. Lauri, V.-M. Kerminen, W. Birmili, and P. H. McMurry (2004), Formation and growth rates of ultrafine atmospheric particles: a review of observations, *J. Aerosol Sci.*, *35*, 143-176.

Laaksonen, A., P. Korhonen, M. Kulmala, and R. J. Charlson (1998), Modification of the Köhler Equation to include soluble trace gases and slightly soluble substances, *J. Atmos. Sci.*, *55*, 853-862.

Laaksonen, A., A. Hamed, J. Joutsensaari, L. Hiltunen, F. Cavalli, W. Junkermann, A. Asmi, S. Fuzzi, and M. C. Facchini (2005), Cloud condensation nucleus production from nucleation events at a highly polluted region, *Geophys. Res. Lett.*, *32*, L06812, doi:10.1029/2004GL022092.

Lei, W., R. Zhang, X. Tie, and P. Hess (2004), Chemical characterization of ozone formation in the Houston-Galveston area, *J. Geophys. Res*., *109*, D12301, doi:10.1029/2003JD004219.

Li, G., R. Zhang, J. Fan, and X. Tie (2005), Impacts of black carbon aerosol on photolysis and ozone, *J. Geophys. Res*., *110*, D23206, doi:10.1029/2005JD005898.

Li, G., R. Zhang, J. Fan, X. Tie (2007), Impacts of biogenic emissions on photochemical ozone production in Houston, Texas, *J. Geophys. Res*., doi:10.1029/2006JD007924, in press.

Lin, Y.-L., R. D. Farley, and H. D. Orville (1983), Bulk parameterization of the snow field in a cloud model, *J. Climate Appl. Meteor.*, *22*, 1065-1092.

Liu, G., H. Shao, J. A. Coakley Jr., J. A. Curry, J. A. Haggerty, and M. A. Tschudi (2003), Retrieval of cloud droplet size from visible and microwave radiometric measurements during INDOEX, *J. Geophys. Res*., *108*(D1), 4006.

Liu, Q., and Y. Kogan (1998), Large eddy simulations of cloud processing of small size aerosols in marine stratocumulus. Preprints, *Conf. on Cloud Physics,* Everett, WA, Amer. Meteor. Soc., 329– 332.

Lurmann, F. W., A. S. Wexler, S. N. Pandis, S. Musarra, N. Kumar, and J. H. Seinfeld (1997), Modeling urban and regional aerosols, II, Application to California's South Coast Air Basin, *Atmos. Environ.*, *31*, 2695–2715.

Lynn, B. H., W.-K. Tao, and P.J. Wetzel (1998), A study of landscape generated deep moist convection. *Mon. Wea. Rev.*, *126*, 928-942.

Lynn, B. H., A. P. Khain, J. Dudhia, D. Rosenfeld, A. Pokrovsky, and A. Seifert (2005a), Spectral (Bin) microphysics coupled with a mesoscale model (MM5). Part I: model description and first results, *Monthly Weather Review*, *133*, 44–58.

Lynn, B. H., A. P. Khain, J. Dudhia, D. Rosenfeld, A. Pokrovsky, and A. Seifert (2005b), Spectral (Bin) microphysics coupled with a mesoscale model (MM5). Part II: simulation of a CaPE rain event with a squall line, *Monthly Weather Review*, *133*, 59–71.

Maritinsson, B. C., et al. (1999), Droplet nucleation and growth in orographic clouds in relation to the aerosol population. *Atmos. Res.*, *50*, 289–315.

McFarquhar, G. M., and H. Wang (2006), Effects of aerosols on trade wind cumuli over the Indian Ocean: Mosel simulations, *Q. J. R. Meteorol. Soc.*, *132*, 821-843.

Meyers, M. P., P. J. DeMott, and W. R. Cotton (1992), New primary ice-nucleation parameterizations in an explicit cloud model, *J. Appl. Meteor.*, *31*, 708-721.

Mallet, M., J. C. Roger, S. Despiau, J. P. Putaud, and O. Dubovik (2004), A study of the mixing state of black carbon in urban zone, *J. Geophys. Res.*, *109*, D04202, doi:10.1029/2003JD003940.

Mebust, M. R., B. K. Eder, F. S. Binkowski, and S. J. Roselle (2003), Models-3 Community Multiscale Air Quality (CMAQ) model aerosol component, 2, Model evaluation, *J. Geophys. Res.*, *108*(D6), 4184, doi:10.1029/2001JD001410.

Meng, Z., D. Dabdub, and J. H. Seinfeld **(**1998), Size-resolved and chemically resolved model of atmospheric aerosol dynamics, *J. Geophys. Res.*, *103*, 3419–3435.

Mircea, M., M. C. Facchini, S. Decesari, F. Cavalli, L. Emblico, S. Fuzzi, A. Vestin, J. Rissler, E. Swietlicki, G. Frank, M. O. Andreae, W. Maenhaut, Y. Rudich, and P. Artaxo (2005), Importance of the organic aerosol fraction for modeling aerosol hygroscopic growth and activation: a case study in the Amazon Basin, *Atmos. Chem. Phys.*, *5*, 3111-3126.

Mohr, K. I., R. D. Baker, W.-K. Tao, and J. S. Famiglietti, (2003), The sensitivity of West African convection line water budgets to land cover. *J. Hydrometeor.*, *4*, 62-76.

Nielsen-Gammon, J. W. (2002), Evaluation and comparison of preliminary meteorological modeling for the August 2000 Houston-Galveston ozone episode: A report to the Technical Analysis Division, Texas Nat. Resour. Conserv. Comm., Austin, report, pp. 19–22.

Nielsen-Gammon, J. W. (2003), Meteorological modeling files, available on http://www.tnrcc.state.tx.us/air/aqp/airquality_photomod.html#met, Texas Nat. Resour. Conserv. Comm., Austin, TX.

Ogura, Y., and Phillips, N. A. (1962), Scale analysis of deep and shallow convection in the atmosphere, *J. Atmos. Sci.*, *19*, 173-179.

Orville, R. E., G. Huffines, J. Nielsen-Gammon, R. Zhang, B. Ely, S. Steiger, S. Phillips, S. Allen, and W. Read (2001), Enhancement of cloud-to-ground lightning over Houston, Texas, *Geophys. Res. Lett.*, *28*, 2597-2600.

Ovtchinnikov, M., and Y. L. Kogan (2000), An investigation of ice production mechanisms using a 3D cloud model with detailed microphysics. Part I: Model description. *J. Atmos. Sci.*, *57*, 2989–3003.

Ovtchinnikov, M., Y. L. Kogan, and A. M. Blyth, (2000), An investigation of ice production. mechanisms using a 3D cloud model with detailed microphysics. Part II: Case study of New Mexico cumulus clouds. *J. Atmos. Sci.*, *57*, 3004–3021.

Park, S.-K., C. E. Cobb, K. Wade, J. Mulhollan, Y. Hu, and A. G. Russell (2006), Uncertainty in air quality model evaluation for particulate matter due to spatial variations in pollutant concentrations, *Atmos. Env.*, *40*, S563-S573.

Pinsky, M., and A. Khain (2002), Effects of in-cloud nucleation and turbulence on droplet spectrum formation in cumulus clouds. *Q. J. R. Meteor. Soc.*, *128*, 1–33.

Pruppacher, H. R., and J. D. Klett (1997), *Microphysics of Clouds and Precipitation*, 2nd ed., Springer, New York.

Ramachandran, S. (2005), Aerosol radiative forcing over Bay of Bengal and Chennai: Comparison with maritime, continental, and urban aerosol models, *J. Geophys. Res.*, *110*, D21206, doi:10.1029/2005JD005861.

Ramanathan, V., et al. (2001a), The Indian Experiment: An integrated assessment of the climate forcing and the effects of the great indo-asian haze, *J. Geophys. Res.*, *106*, 28,371–28,398.

Ramanathan, V., P. J. Crutzen, J. T. Kiehl, and D. Rosenfeld (2001b), Aerosol, climate and the hydrological cycle, *Science*, *294*, 2119–2124.

Rasmussen R. M., I. Geresdi, G. Thompson, K. Manning, and E. Karplus (2002), Freezing drizzle formation in stably stratified layer clouds: The role of radiative cooling of cloud droplets, cloud condensational nuclei, and ice initiation. *J. Atmos. Sci.*, *59*, 837–860.

Reisin, T., Z. Levin, and S. Tzvion (1996a), Rain production in convective clouds as simulated in an axisymmetric model with detailed microphysics. Part I: Description of the model. *J. Atmos. Sci.*, *53*, 497–519.

Reisin, T., Z. Levin, and S. Tzvion (1996b), Rain production in convective clouds as simulated in an axisymmetric model with detailed microphysics. Part II: Effects of varying drops and ice initiation. *J. Atmos. Sci.*, *53*, 1815–1837.

Reisin, T., S. Tzivion, and Z. Levin (1996c), Seeding convective clouds with ice nuclei or hygroscopic particles: A numerical study using a model with detailed microphysics. *J. Appl. Meteor.*, *35*, 1416–1434.

Roelofs, G.-J., and S. Jongen (2004), A model study of the influence of aerosol size and chemical properties on precipitation formation in warm clouds, *J. Geophys. Res.*, *109*, D22201, doi:10.1029/2004JD004779.

Rosenfeld, D. (1999), TRMM observed first direct evidence of smoke from forest fires inhibiting rainfall, *Geophys. Res. Lett.*, *26*, 3105–3108.

Rosenfeld, D. (2000), Suppression of rain and snow by urban and industrial air pollution, *Science*, *287*, 1793–1796.

Rosenfeld, D., and W. L. Woodley (1999), Satellite-inferred impact of aerosols on the microstructure of Thai convective clouds, *Proc. Seventh Scientific Conf. on Weather Modification*, Chiang Mai, Thailand, World Meteorological Organization, 17–20.

Rosenfeld, D., and W. L. Woodley (2000), Deep convective clouds with sustained supercooled liquid water down to −37.5°C. *Nature*, *405*, 440–442.

Russell, L. M., and J. H. Seinfeld (1998), Size- and composition-resolved externally mixed aerosol model, *Aerosol Sci. Technol.*, *28*, 403–416.

Russell, M., D. T. Allen, D. R. Collins, and M. P. Fraser (2004), Daily, seasonal and spatial trends in $PM_{2.5}$ mass and composition in southeast Texas, *Aerosol Sci. Technol.*, *38*, 14–26.

Seinfeld, J. H., S. N. Pandis (1998), *Atmospheric Chemistry and Physics: from Air Pollution to Climate Change*, John Wiley & Sons, Inc., NY.

Shepherd, J. M., and S. J. Burian (2003), Detection of urban-induced rainfall anomalies in a major coastal city, *Earth Interactions*, *7*, 1-17.

Smolarkiewicz, P. K., and W. W. Grabowski (1990), The multidimensional positive advection transport algorithm: Nonoscillatory option, *J. Comput. Phys*., *86*, 355-375.

Soong, S.-T., and Y. Ogura, (1980), Response of tradewind cumuli to large-scale processes, *J. Atmos. Sci.*, *37*, 2035-2050.

Stevens, B., G. Feingold, W. R. Cotton, and R. L. Walko (1996), Elements of the microphysical structure of the numerically simulated nonprecipitating stratocumulus. *J. Atmos. Sci.*, *53*, 980–1006.

Takahashi T. (1976), Hail in an axisymmetric cloud model. *J. Atmos. Sci*, *33*, 1579–1601.

Tao, W.-K., and J. Simpson (1993), The Goddard Cumulus Ensemble Model. Part I: Model description, *Terrestrial*, *Atmospheric and Oceanic Sciences*, *4*, 19-54.

Tao, W.-K., J. Simpson, D. Baker, S. Braun, M.-D. Chou, B. Ferrier, D. Johnson, A. Khain, S. Lang, B. Lynn, C.-L. Shie, D. Starr, C.-H. Sui, Y. Wang, and P. Wetzel (2003a), Microphysics, radiation and surface processes in the Goddard Cumulus Ensemble (GCE) model, *Meteorol. Atmos. Phys.*, *82*, 97-137.

Tao, W.-K., C.-L. Shie, J. Simpson, S. Braun, R. H. Johnson, and P. E. Ciesielski (2003b), Convective systems over the south China sea: cloud-resolving model simulations. *J. Atmos. Sci.*, *60*, 2929–2956.

Twomey, S. (1977), The influence of pollution on the shortwave albedo of clouds, *J. Atmos. Sci.*, *34*, 1149-1152.

Wang, C. (2004), A modeling study on the climate impacts of black carbon aerosols, *J. Geophys. Res.*, *109*, D03106, doi:10.1029/2003JD004084.

Wang, C. (2005), A modeling study of the response of tropical deep convection to the increase of cloud condensation nuclei concentration: 1. Dynamics and microphysics, *J. Geophys. Res.*, *110*, D21211, doi:10.1029/2004JD005720.

Wetzel, P. J., and A. Boone (1995), A parameterization for land–atmosphere–cloud exchange (PLACE): Documentation and testing of a detailed process model of the partly cloudy boundary layer over heterogeneous land, *J. Clim.*, *8*, 1810–1837.

Whitby, K. T. (1978), The physical characteristics of sulfur aerosols, *Atmos. Environ.*, *12*, 135-159.

Wolf, S. (2006), *Mie Scattering by Ensembles of Particles with Very Large Size Parameters*, Astrophysics Software Database, MPIA Heidelberg, Germany.

Xu, J., M. H. Bergin, R. Greenwald, and P. B. Russell (2003), Direct aerosol radiative forcing in the Yangtze delta region of China: Observation and model estimation, *J. Geophys. Res.*, *108*, 4060, doi:10.1029/2002JD002550.

Yin, Y., Z. Levin, T. Reisin, and S. Tzivion (2000a), The effects of giant cloud condensational nuclei on the development of precipitation in convective clouds: A numerical study, *Atmos. Res.*, *53*, 91–116.

Yin, Y., Z. Levin, T. Reisin, and S. Tzivion (2000b), Seeding convective clouds with hygroscopic flares: Numerical simulations using a cloud model with detailed microphysics, *J. Appl. Meteor.*, *39*, 1460–1472.

Zamora, R. J., Wilczak, J. M., Bao, J.-W., and Michelson, S. A. (2003), Heat flux and energy balance in Houston, A progress report to the Technical Analysis Division, Texas Commission on Environmental Quality (TCEQ), May 30, Austin, TX.

Zamora, R. J., Dutton, E. G., Trainer M., McKeen, S. A., Wilczak, J. M., and Hou, Y.-T. (2005), The accuracy of solar irradiance calculations used in mesoscale numerical weather prediction, *Mon. Wea. Rev.*, *133*, 783-792.

Zhang, R., X. Tie, and D. W. Bond (2003), Impacts of anthropogenic and natural NO_x sources over the U.S. on tropospheric chemistry, *Proc. Natl. Acad. Sci. USA*, *100*, 1505–1509.

Zhang, R., I. Suh, J. Zhao, D. Zhang, E.C. Fortner, X. Tie, L.T. Molina, and M.J. Molina (2004a), Atmospheric new particle formation enhanced by organic acids, *Science*, *304*, 1487-1490.

Zhang, R., W. Lei, X. Tie, P. Hess (2004b), Industrial emissions cause extreme diurnal urban ozone variability, *Proc. Natl. Acad. Sci. USA*, *101*, 6346-6350.

Zhang, R., G. Li, J. Fan, D. L. Wu, E. R. Williams, and M. J. Molina (2007), Intensification of Pacific storm track linked to Asian pollution, *Proc. Natl. Acad. Sci. USA*, *104*, 5295-5299.

Zhang, Y., R. C. Easter, S. Ghan, and H. Abdul-Razzak (2002), Impact of aerosol size representation on modeling aerosol-cloud interactions, *J. Geophys. Res.*, *107*, D21, 4558, doi:10.1029/2001JD001549.

Zilitinkevich, S. S. (1975), Comments on "A model for the dynamics of the inversion above a convective boundary layer." *J. Atmos. Sci.*, *32*, 991-992.

VITA

Name: Jiwen Fan

Address: Department of Atmospheric Sciences, Texas A&M University, 3150 TAMU, College Station, TX 77843-3150

Email Address: fannie@ariel.met.tamu.edu

Education: B.S., Chemistry, Xiangtan Normal University, China, 1996
M.S., Environmental Engineering, China University of Mining & Technology (Beijing Campus), 1999
M.S., Environmental Engineering, University of Central Florida, 2002
Ph.D., Atmospheric Sciences, Texas A&M University, 2007

Research Experience:

Research Assistant, Texas A&M University, Jun 2002 – Jun 2007
Aerosol effects in cumulus clouds and air quality modeling
NASA/GSFC Student Visitor, Sep – Nov 2005.
Research Assistant, University of Central Florida, Aug 2000 – May 2002
Highway vehicle emission dispersion modeling
Environmental Engineer, Tsinghua Unisplendor Group, Beijing, China, Jul 1999 – Jul 2000
Research Assistant, China University of Mining & Technology (Beijing Campus), Sep 1996 – Jun 1999
Sulfur-fixation in the process of coal combustion at high temperature